Study on the Epitaxial Strain Effects on Optoelectronic Properties of Functional Oxides with Rutile Structure

ルチル構造を有する機能性酸化物の光電子特性に及ぼすエピタキシャル歪の効果に関する研究

BINJIE CHEN

Graduate School of Information Science and Technology

Hokkaido University

March 2023

Table of Contents

List of Figures

List of Tables

List of Acronyms

IC	Integrated circuit
MO_2	Metal dioxide
CBM	Conduction band minimum
VBM	Valence band maximum
TCO	Transparent conducing oxide
R	Rutile
M	Monoclinic
RT	Room temperature
IR	Infrared
IMT	Insulator-to-metal transition
ITO	Indium tin oxide
IL	Ionic liquid
EDLTs	Electric double-layer transistors
C12A7	$12CaO \cdot 7Al_2O_3$
YSZ	Yttria-stabilized zirconia
LSGM	$La_{1-x}Sr_xGa_{1-y}Mg_yO_{3-\delta}$
TFTs	Thin film transistors
PLD	Pulsed laser deposition
XRD	X-ray diffraction
XRR	X-ray reflectivity
AFM	Atomic force microscopy
SCL	Strain compensation layer
ML	Multilayer
XAS	X-ray absorption spectroscopy

DFT	Density functional theory
VASP	Vienna ab initio simulation package
GGA	Generalized gradient approximation
HSE06	Heyed, Scuseria and Ernzerhof
STEM	Scanning transmission electron microscopy
HAADF	High-angle annular dark field
IFFT	Inverse fast Fourier transformation
DOS	Density of state
QSE	Quantum size effect
FWHM	Full width at half maximum

List of Symbols

E_g	Bandgap
m^*	Effective mass
m_0	Electron mass
n_s	Carrier concentration
T_c	Critical temperature
λ	Wavelength
T	Temperature
ΔV	Thermo-electromotive force
ΔT	Temperature difference
S	Thermopower
q	Scattering vector
ρ	Resistivity
ΔT_c	Thermal hysteresis
P_{O2}	Oxygen pressure
T_{sub}	Substrate temperature
t_c	Critical thickness
μ_{Hall}	Hall mobility
R_{rms}	Root mean square roughness
U	Hubbard term
σ	Conductivity
k_B	Boltzmann constant
F_r	Fermi integral
r	Scattering parameter of the relaxation time
ξ	Chemical potential

h	Plank's constant
α	Absorption coefficient
v	Speed of light
m_e^*	Electron effective mass
m_h^*	Hole effective mass
T	Transmission
R	Reflection
D	Thickness
r	Power factor

Chapter 1. General Introduction

1.1. Background of this thesis

Since the first development of the transistor in the middle of the 20th century [1], human society has rapidly moved towards the age of electronics. Subsequently, the exploration and development of electronic materials have also been springing up and the profits are now being used in the daily lives of billions of people around the world. Among them, silicon and its derivatives are the well-deserved cornerstones of the electronics industry; Almost all the integrated circuits (IC) are built from them so far. Although status of the silicon-based devices is still dominating, with the emergence of some special demands as well as expectations for device with higher performance, the development of function specialized materials (known as functional material) has become an urgent priority.

Metal oxides are a big family of materials with a variety of different properties. They exhibit an ever-growing use in some specific areas such as display [2], sensor [3, 4], memory [5], etc., owning to their abundant and tunable properties, high chemical stability, low-cost of synthesis, etc. **Figure 1-1** shows a series of typical functional applications of metal oxides. As the typical case of metal oxides, amorphous indium gallium zinc oxide (a-IGZO) has been commercially used in display industry. The

applications of metal oxides on sensor and memory are also promising and under development. In addition to the electronic applications, metal oxides also show potentiality in the fields of energy and catalysis [6, 7]. It is worth noting that the specific application of such materials often highly depends on their physical and chemical properties. The property regulation and even design of the material are expected to improve the performance of devices based on them and even open up new applications. According to this point, it is necessary to investigate the method suitable for material property regulation and study on the corresponding effects of such method. In this thesis, I was committed on the epitaxial strain effects on optoelectronic properties of the rutile-structured metal oxides.

1.2. Introduction to rutile-structured functional oxides

Rutile structure, which gets its name from a natural mineral of titanium dioxide (TiO_2), is one of the simplest and widely distributed crystal structure for metal oxides. It is usually represented by the chemical formula of MO_2 (*M*: metal cations), in which the *M* cations and oxygen anions form a MO_6 octahedra as the base unit. Such octahedra shares vertices in the tetragonal *ab* plane and the edges along the *c*-axis, eventually forming the rutile structure as shown in **Figure 1-2**. There are many different rutile-structured oxides with various *M* cations referring to transition metals (Ti, V, Nb, Ru, Ir, etc), post-transition metal (Sn and Pb), metalloid (Ge), and even nonmetals (Si) [8]. Due

to the difference in electron configuration of *M* cations as well as the orbital overlapping with oxygen anions, this series of materials exhibits a variety of physical properties and used as the functional materials in various fields, such as photocatalysis, sensor, conductivity, etc. Next, I would like to introduce three types of typical rutile-structured oxides involved in this thesis.

1.1.1. Titanium dioxide (TiO_2)

TiO_2 is a well-known oxide material with a wide range of industrial applications, such as pigment, sunscreen coating, colorant, etc. In the 1960s, A. Fujishima and K. Honda discovered the photocatalytic effect of TiO_2 [7], making it an ideal active material for photocatalytic water splitting and receiving continuous research in the following decades. There are several different TiO_2 polymorphs, which can be represented by rutile (Space group: $P4_2/mnm$, a = 0.4594 nm, c = 0.2958 nm) and anatase (space group: $I4_1/amd$, a = 0.3785 nm, c = 0.9505 nm). Rutile is the stable phase and the most common natural mineral. Anatase is metastable phase which can be stabled at low temperatures, owning to its relatively low surface energy. However, anatase phase changes into the rutile phase when heated up above 600 °C [9, 10].

Both rutile and anatase phase exhibit photocatalytic activity. Their conduction band minimum (CBM) and valence band maximum (VBM) are both composed by Ti 3d and

O 2p orbitals. Rutile TiO_2 was determined to show a direct bandgap (E_g) of ~3.06 eV, while anatase TiO_2 is an indirect semiconductor with E_g of ~3.2 eV. Both these two E_g are around the maximum photon energy of visible light (~3.1 eV) [11]. When TiO_2 absorbs light (photon energy >E_g), the valence electron is excited to the conduction band, generating a positive hole in the valence band. The conduction electron reduces water while the hole oxidizes it, subsequently generating hydrogen and oxygen [7, 12-14]. Such photocatalytic activity is strongly related to the crystal structure of TiO_2 because the electronic structure as well as the physical properties are determined by the crystal structure [15-19]. Generally, anatase is more active than rutile [18], although the smaller E_g of rutile is favor to the visible light absorption. Previous studies stated that nature of bandgap, carrier mobility, lifetime of exciton, etc. may also play some roles. The combined effect of multiple factors eventually determines the photocatalytic activity of TiO_2. To further explore the potential of TiO_2 in photocatalysis as well as other application, modification of its basic physical properties is essential.

1.1.2. Tin dioxide (SnO_2)

Tin dioxide (SnO_2), also known as stannic oxide and cassiterite, is another traditional rutile-structured oxide which has won extensive fundamental and application studies for over a century. Different from the polymorphic characteristics of TiO_2, SnO_2 only stabilized as the rutile phase (space group: $P4_2/mnm$, a = 0.4737 nm, c = 0.3186 nm)

under thermal equilibrium state. The band structure of SnO_2 is dominated by the Sn 5s-based CBM and the O 2p-based VBM and the optical bandgap is varied from ~3.5 eV to 4.0 eV, which depends on the crystalline state (single crystal/polycrystal/amorphous etc.) and the growth conditions [20, 21].

The large optical bandgap brings an excellent transparency in both visible and infrared regions, while Sn 5s orbitals overlaps with each other, allowing the free movement of electrons, consequently leading to the small electron effective mass (m^*) [22]. Besides, the enhancement of carrier concentration (n_s) of SnO_2 has been experimentally achieved by chemical doping of cations with valance higher than Sn^{4+} (e.g. Ta, Nb, Sb, etc.). Thus, electron-doped SnO_2 is considered as a great candidate of transparent conducing oxide (TCO) [23, 24]. In addition to the application of TCO, SnO_2 has also been evaluated as gas sensor, catalyst, transistor as well as a series of other optoelectronic applications [25-27]. Anyway, similar to that of TiO_2, the potential applications of SnO_2 are determined by its inner physical properties. Understanding the effects of some regulation methods such as doping, gating and strain on the physical properties of SnO_2 is expected to provide a guidance for optimizing the SnO_2-based devices and even discovering more functional properties.

1.1.3. Vanadium dioxide (VO_2)

Different from the TiO_2 and SnO_2, stable in rutile phase at room temperature (RT), the RT phase of bulk vanadium dioxide (VO_2) is monoclinic (M1, space group: $P2_1/c$, a = 0.5759 nm, b = 0.5363 nm, c = 0.4518 nm, β = 122.3°), whereas it transfers to rutile phase (R, space group: $P4_2/mnm$, a = 0.4528 nm, c = 0.2860 nm) when temperature is higher than ~68 °C (~341 K) [28]. The most striking structure difference between these two polymorphic forms of VO_2 is the arrangement of V^{4+} ions along c-axis, where they form zigzag chains (so-called V−V dimers) in monoclinic phase, resulting in the alternate V−V spacing of 0.265 nm and 0.312 nm, respectively. On the contrary, rutile VO_2 has an evenly divided V^{4+} ion chain with the distance of 0.296 nm (**Figure 1-3**). Besides the M1 and R phase, VO_2 also has various polymorphs such as A, B, and M2 phase [29]. Among them, the lattice of M2 phase consists of half zigzag chains and half equidistant chains. Thus, M2 is regarded as an intermediate phase during the phase transition between M1 phase and R phase [30, 31].

The transition of crystal structure is usually accompanied by dissimilation of electronic structure, eventually leading to the difference in physical properties. In case of VO_2, M1 phase is an infrared (IR) transparent insulator while R phase is a metallic-like semiconductor with low transmittance in IR region (**Figure 1-3(c)**). Thus, VO_2 has been considered as a candidate for thermochromic materials [32, 33]. It has also been

reported that the phase transition behavior of VO_2 can be manipulated by applying electric or optical field, promising the application in information computing and memory [34, 35]. However, the phase transition temperature (T_c) of intrinsic bulk VO_2 is still a little bit high. Reducing the T_c to around RT is critical for practical applications. Chemical doping, field effect and strain effect have been demonstrated to be effective in regulating T_c. I would like to discuss them in detail in chapter 1.2.

In addition to the potential for applications, the phase transition mechanism of VO_2 also attracts extensive investigations in few past decades, however there is still no generally accepted explanation. The bone of contention rages on whether insulator-to-metal transition (IMT) are strictly bound to the lattice distortion. From different viewpoint, two alternate scenarios were proposed: lattice distortion driven IMT (Peierls transition) [36] and electron correlation driven IMT (Mott transition) [37]. In recent years, an intermediate mechanism integrating the two have also been emerged, so-called cooperative Mott-Peierls transition [38, 39]. The difficulty in deconstructing its mechanism lies on the observation of intermediate processes of IMT and anomalous phases of VO_2 (e.g. metallic M phases [40, 41]). Inducing the emergence of such phases through property regulation method is expected to provide guidance.

1.2. General methods to regulate the physical property of rutile phase

The property regulation and design are important prerequisites for the application of functional materials. There are various methods have been developed to achieve effective regulations, such as chemical doping, growth condition controlling, field gating, etc., while for materials in film form, epitaxial strain is also a common way, because of the intimate relations between lattice, electron charge, orbital energy and overlapping. In this chapter, I would like to introduce the effects of these regulation methods on properties of TiO_2, SnO_2 and VO_2.

1.2.1. Chemical doping

Chemical doping is the most typical method to regulate the properties of materials. Especially for the control of carrier, carrier concentration (n_s) and even the type of carrier (electron/hole) can be effectively adjusted by doping electron or hole dopants. On the other hand, some specific properties (e.g. electrical conductivity, magnetism, etc.) are possible to be introduced when doping the atoms with such properties. Moreover, for crystalline materials, doping the material with different ionic radii will change the lattice parameter or even induce structural transitions.

The chemical doping of rutile-structured oxides has been extensively investigated. Studies revealed that the substitution of Ti in TiO_2 by a series of transition metals (e.g. V,

Cr, Co, Ni, etc.) can narrow the bandgap and improve the absorption of visible light, which points to improving its photocatalytic efficiency [42, 43]. For SnO_2, doping of V cations (Sb, Ta, etc.) on Sn^{4+} site or VII anion (F^-) on O^{2-} site can greatly optimize its conductivity by increasing n_s [23, 24, 44, 45]. Thus, electron-doped SnO_2 is expected to replace the ITO as the indium-free transparent conducting oxides. Lastly, doping in VO_2 aims to lower its T_c. An empirical conclusion has been drawn—dopants with higher valance than V^{4+} (e.g. Nb^{5+}, W^{6+}, etc.) tend to reduce the T_c, whereas dopants with lower valance than V^{4+} (Ga^{3+}, Cr^{3+}, Mg^{2+}, etc) increase the T_c (**Figure 1-4**) [46, 47]. Among them, W doping exhibits the best efficiency [48, 49]. Chemical doping shows high universality in material modulation, however, the parasitic effect (defect, inhomogeneity, etc.) and fraction limitation of doping bring difficulties on practical use.

1.2.2. Field effect

Field effect modulation of property is a broad concept, in which the 'field' represents not only electric field, but also magnetic field, light field and other physical field. However, due to the controllability and compatibility with integrated circuits, electric field has been considered as the most suitable 'trigger' for property modulation of functional materials. The following will mainly deal with electric filed effects.

In a narrow sense, field effect refers to the regulation of n_s of a material by

electrostatic effect, where traditional field effect transistor structures based on solid-state dielectrics (SiO_2, Al_2O_3, Y_2O_3, HfO_2, etc.) are widely used. However, such oxides exhibit limited ability on regulation of n_s ($<10^{13}$ cm^{-2}). In recent years, ionic liquid (IL)-based electric double-layer transistors (EDLTs), which exhibit stronger regulation ability ($\sim10^{14}$ cm^{-2}), have been proposed and achieved impressive results in property regulation [50-52]. At present, the field effect is no longer limited to the regulation of carriers. A series of electrochemical methods are also included in this category, such as electric filed induced ion implantation (H^+ by IL, proton conductors such as $12CaO{\cdot}7Al_2O_3$ (C12A7), pectin, nanogranular SiO_2, etc.) and redox (O^{2-} by IL, oxide ion conductors such as YSZ, LSGM, $NaTaO_3$, etc.) [53-57].

Specific to regulated materials, rutile TiO_2 was reported to give rise to metallization through ionic liquid-induced oxygen vacancies [58]. SnO_2 is a candidate for the channel material of thin film transistors (TFTs). To achieve this application, D. Liang and her co-authors modulated the thermopower of SnO_2 film by electric field effect, further optimizing the performance of SnO_2 TFT [59, 60]. VO_2, as a strongly correlated electronic oxide with phase transition, has always been an ideal target for field effect gating. Its switching between metallic and insulating states has been achieved by ferroelectric field effect, protonation and redox of ionic liquids, respectively [61-63]. Moreover, recent studies also revealed that light filed excitation can also control the phase transition behavior of VO_2 [34, 64].

1.2.3. Epitaxial strain engineering

Crystals are formed by the periodic accumulation of a large number of atoms. The overlapping and hybridization of the electron orbitals of these atoms constitutes the energy band and finally determines the electronic structure of a crystal. Since the physical, chemical and optical properties of a crystal are usually determined by electronic structure, transition of crystal structure and change of lattice parameters may affect the properties of material through perturbations to the electronic structure [15, 65-67]. The subsequent issue is how to regulate the lattice. For epitaxial films, the difference in lattice parameters between substrate and film, so-called lattice mismatch, provides an excellent facility for introducing strain (**Figure 1-5(a)** and **4(b)**). Furthermore, by adjusting the thickness of the film, the degree of strain can also be designed within a certain range [68, 69]. It is necessary to note that that whether an epitaxial film can be grown on a particular substrate, and the crystallographic orientation of the film also depend on the compatibility of the two. Previous studies have revealed that the substrates suitable for epitaxial growth of rutile structured oxide films mainly includes single-crystalline silicon (Si), sapphire (Al_2O_3), magnesium fluoride (MgF_2) and rutile TiO_2 itself [70, 71].

Rutile TiO_2 is used more as an optimal substrate for growing rutile phase, while the reports on its own strain regulation are rare. In the chapter 4 of this thesis, a systematical

study of optoelectronic properties of TiO_2 as a function of strain conditions will be presented [68]. Epitaxial strain effect on SnO_2 film focus on its optical bandgap. Both theoretical and experimental results suggested that the optical bandgap of epitaxial SnO_2 film decreases with increasing strain [20].

Lastly, I would like to highlight the epitaxial strain effect on the VO_2. As I have mentioned in chapter 1.1.3, the key to VO_2 phase transition is the kink of V−V chain along *c*-axis. Therefore, it is widely accepted the phase transition behavior of VO_2 is dominated by lattice parameter *c* of R-VO_2 (c_R, corresponding to *a* of M-VO_2 (a_M)) [67, 72, 73]. According to this, a series of studies aiming to reduce the T_c were proposed. Y. Muraoka and Z. Hiroi firstly fabricated epitaxial VO_2 films on (001) TiO_2 substrates and an abrupt phase transition with highly reduced T_c around room temperature (~300 °C) was demonstrated, owing to the isomorphism of TiO_2 substrate with R-VO_2 and the reduced c_R of VO_2 due to tensile strain from substrate (~0.86%) [73]. Thereafter, the growth of VO_2 film on other substrates (A-, C-, R- and M-sapphire, (001), (101) and (110) MgF_2, etc.) and the corresponding strain effects on T_c of VO_2 were also continuously investigated [74, 75]. In general, they all show a certain effect but still not as good as TiO_2. The strain effect from (001) TiO_2 substrates was considered the most effective way to reduce T_c of VO_2 so far.

However, there are also some restrictions on strain engineering by using substrates.

On the one hand, the realization of film epitaxy depends on the suitable lattice mismatch, leading to the limited choice of substrates. On the other hand, strain effects fail due to the strain relaxation when film is thicker than a critical thickness (**Figure 1-5(c)**). In case of VO_2 film, the use of TiO_2 substrate, which shows best effect on reducing T_c, is not realistic in large-scale applications like the smart window because of the size limitation of Verneuil-grown TiO_2 crystal [76]. Also, the VO_2 film thickness is limited due to strain relaxation through crack formation (**Figure 1-5(d)**) [77-85].

1.3. Objective of this thesis

The objective of this thesis is to investigate the epitaxial strain effects on physical properties of rutile-structured functional oxides. Three typical oxides with rutile structure, TiO_2, SnO_2 and VO_2, were selected due to their rich physical properties and potential applications in optoelectronics. To achieve the research goal, a series of these three films were epitaxially fabricated on M-plane sapphire (α-Al_2O_3) substrates through pulsed laser deposition technique. Because of the anisotropic in-plane lattice parameters of M-sapphire, the epitaxial films grown on it receive asymmetric lattice strain (**Figure 1-6**). Consequently, such strain induced orthorhombic distortion was observed in TiO_2 and VO_2 films grown on it. Moreover, by adjusting the film thickness, the degree of such distortion was modulated, further resulting in the regulation of effective mass (TiO_2), optical bandgap (TiO_2) and the insulator-to-metal transition (IMT)

behavior (VO_2). On the contrary, strain induced distortion did not appear in SnO_2 film. The mechanism of this anomalous phenomenon was revealed through a comparison study between TiO_2 and SnO_2.

This thesis is organized by following chapters. In chapter 1, the related background and purposes of this study were introduced. In chapter 2, the near room temperature IMT behavior of VO_2/TiO_2 bilayer film on M-sapphire was demonstrated. Furthermore, the effects of strain induced orthorhombic distortion on the IMT behaviors of VO_2/TiO_2 bilayer films grown on M-sapphire substrate were discussed [69]. In chapter 3, a method to suppress the strain relaxation and crack formation of VO_2 film grown on TiO_2 substrate was proposed. Chapter 4 demonstrated the effects of orthorhombic distortion on the optoelectronic properties of rutile TiO_2 films, where the effective mass and optical bandgap clearly regulated [68]. Then in chapter 5, the absence of orthorhombic distortion was observed in SnO_2 film and subsequently explained by the specific lattice mismatch between SnO_2 and M-sapphire. Finally, the overall results of this thesis are summarized in chapter 6. To my knowledge, this thesis is the first to propose a method for introducing orthorhombic distortion in films with rutile structure through epitaxial strain and systematically study the effects of such distortion on optoelectronic properties of these films. The contribution reported in this thesis would provide a beneficial guidance for design of rutile-type oxide based functional devices.

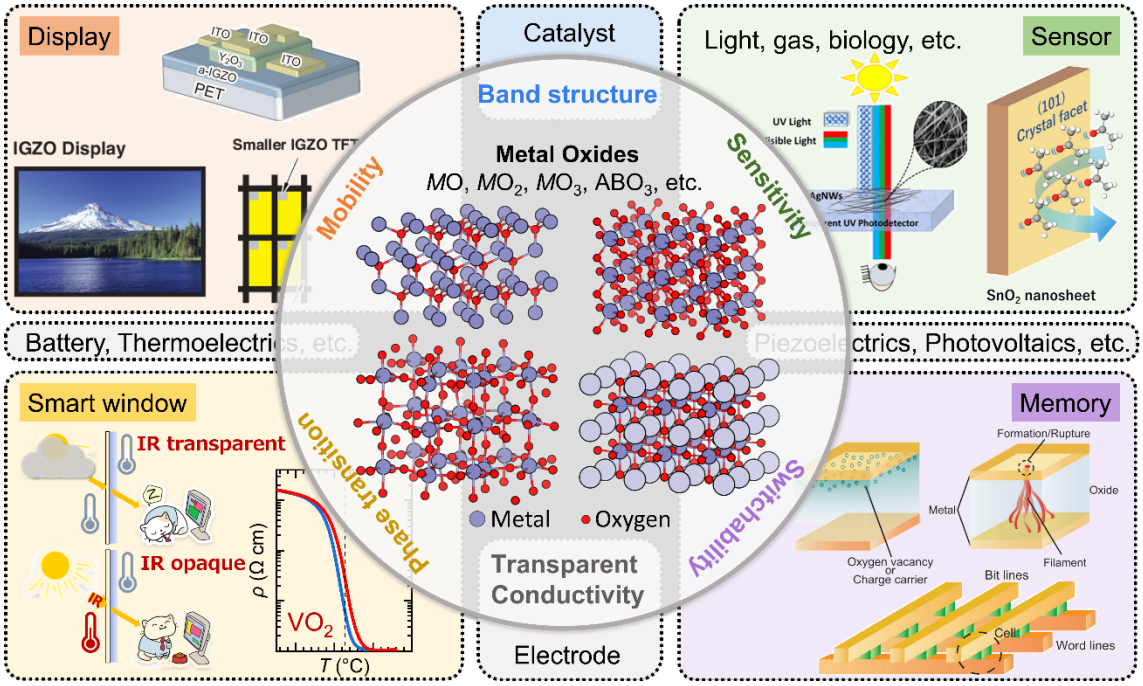

Figure 1-1. Schematic illustration of the various applications of metal oxides. The showing examples are a-IGZO (display) [2], TiO_2/SnO_2 (sensor) [3, 4], VO_2 (smart window), and NiO/La_2CuO_4 (memory) [5], respectively.

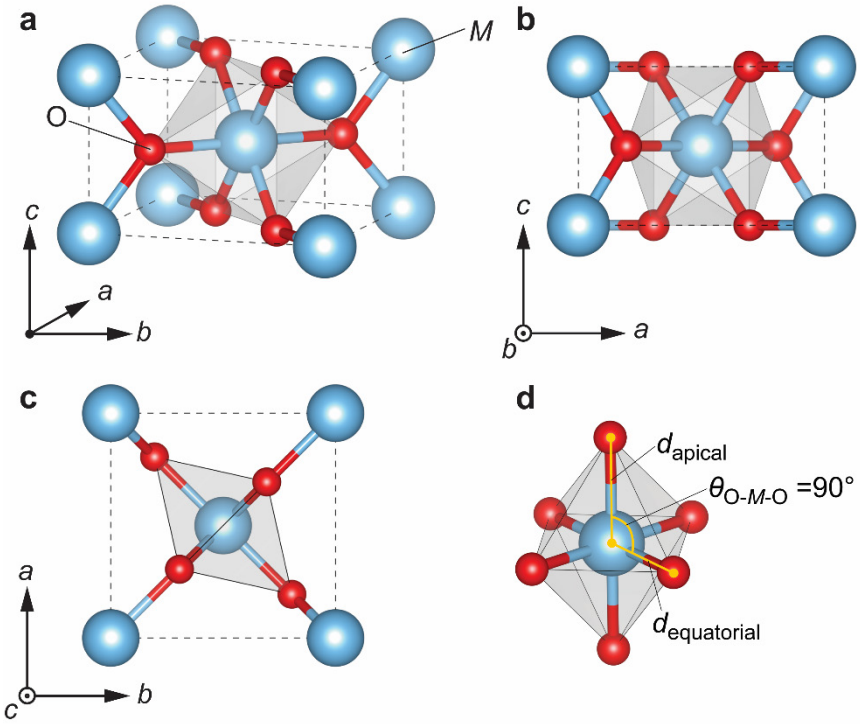

Figure 1-2. Crystallographic structure of rutile structured oxide. View (a) with standard orientation, (b) along [010] and (c) [001] MO_2 zone axis. (d) MO_6 octahedra.

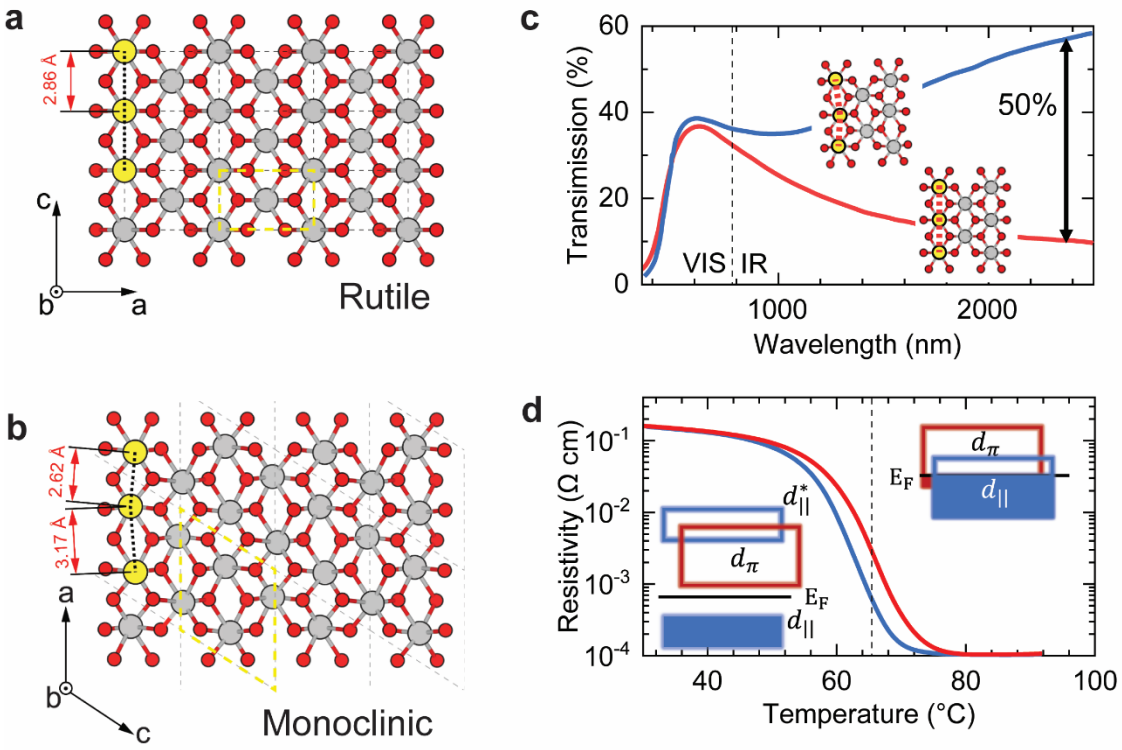

Figure 1-3. Phase transition and accompanied physical property changes of VO_2. Atomic arrangement of (a) rutile VO_2 and (b) monoclinic VO_2. The dashed lines are the eye guide of the change of V−V dimers during phase transition. The difference in (c) optical transmission and (d) resistivity between rutile and monoclinic VO_2.

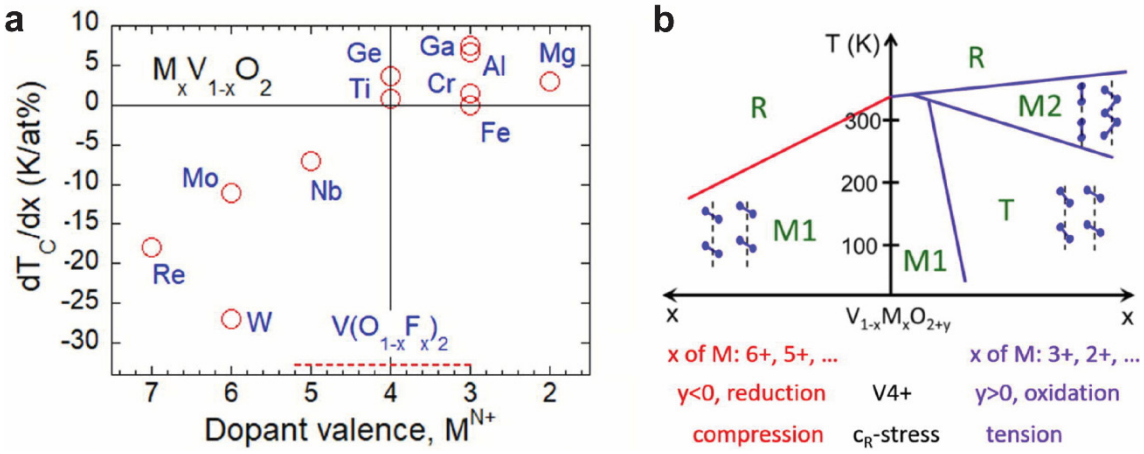

Figure 1-4. Doping effect on phase transition behavior of VO_2[46]. (a) Changing rate of critical temperature of VO_2 phase transition with different dopants. (b) A schematic phase diagram of VO_2 for doping, non-stoichiometry, and uniaxial stress.

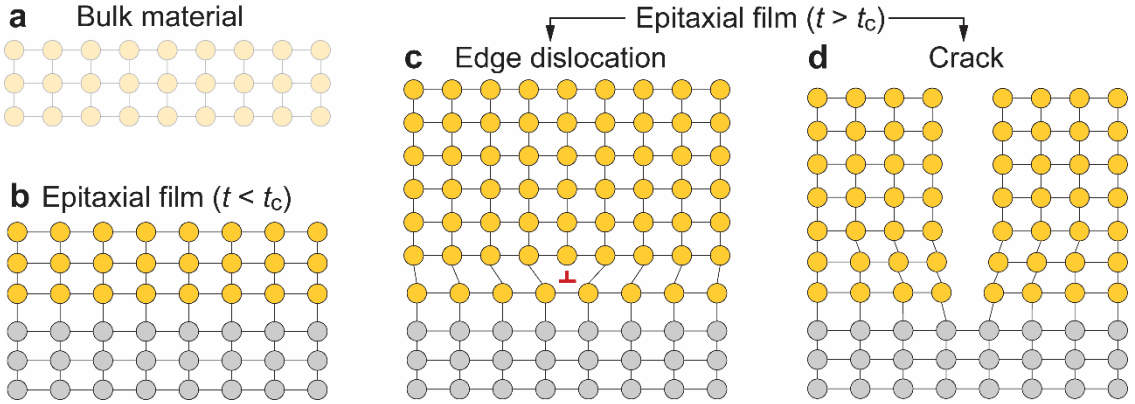

Figure 1-5. Schematic diagram of epitaxial growth induced strain condition and strain relaxation. Atomic arrangement of (a) a bulk material without strain. (b) highly strained epitaxial film. Strain relaxation through (c) dislocation and (d) crack formation when film thickness exceeds the critical thickness (t_c).

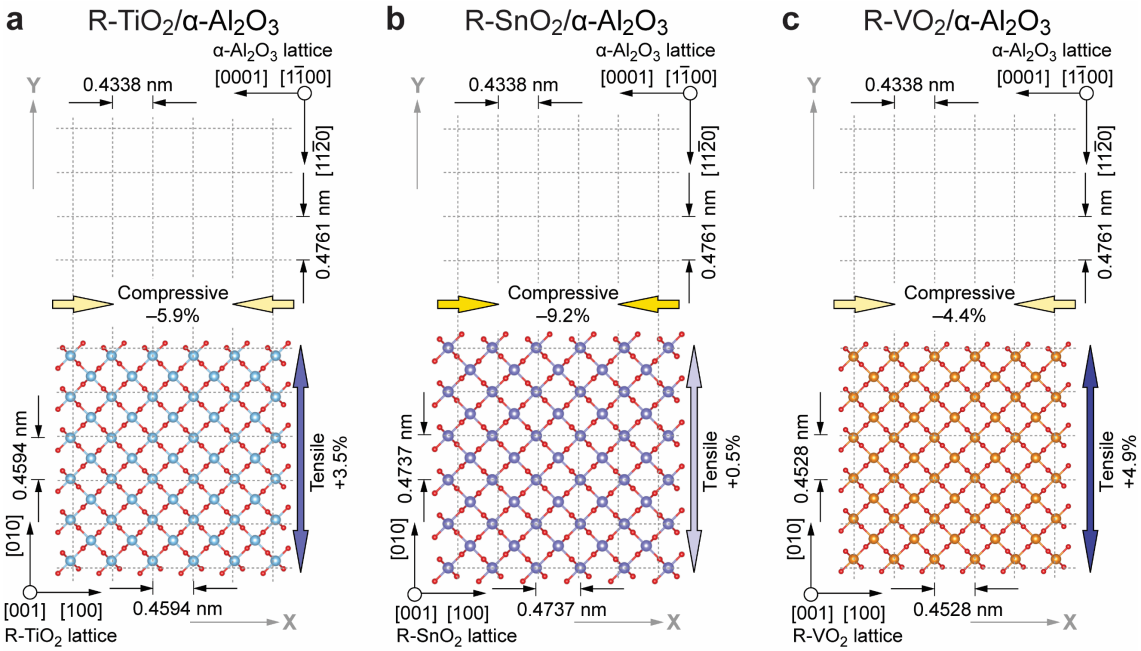

Figure 1-6. The atomic arrangements of rutile structured oxide films on M-plane sapphire substrate. (a) Schematic crystal lattice of rutile R-TiO_2 on (1$\bar{1}$00) α-Al_2O_3 (sublattice of oxide ions, dotted lines). The lattice parameter of TiO_2 along [100] direction is larger than that of α-Al_2O_3 along [0001] (lattice mismatch: −5.9%), suggesting a compressive strain along X direction, whereas tensile strain is assumed along the Y direction ([11$\bar{2}$0] α-Al_2O_3) due to the relatively small lattice parameter of TiO_2 along this direction compared to that of α-Al_2O_3 (lattice mismatch: +3.5%). (b) Schematic crystal lattice of rutile R-SnO_2 on (1$\bar{1}$00) α-Al_2O_3. The lattice parameter of SnO_2 along [100] direction is extremely larger than that of α-Al_2O_3 along [0001] (lattice mismatch: −9.2%) suggesting a compressive strain along X direction, whereas the lattice mismatch along Y direction is almost absent (+0.5%), resulting in the negligible tensile strain. (c) Schematic crystal lattice of rutile R-VO_2 on (1$\bar{1}$00) α-Al_2O_3. The strain conditions of VO_2 are similar to these of R-TiO_2. Compressive and tensile strains are assumed along X and Y directions, respectively.

References

[1] Bardeen, J. and W.H. Brattain, The Transistor, a Semi-Conductor Triode. *Phys. Rev.* **74**, 230-231 (1948).

[2] Nomura, K.*, et al.*, Room-Temperature Fabrication of Transparent Flexible Thin-Film Transistors using Amorphous Oxide Semiconductors. *Nature* **432**, 488-492 (2004).

[3] Abbas, S.*, et al.*, Silver-Nanowire-Embedded Transparent Metal-Oxide Heterojunction Schottky Photodetector. *ACS Appl. Mater. Interfaces* **10**, 14292-14298 (2018).

[4] Kim, K.*, et al.*, Catalyst-Free Highly Sensitive SnO_2 Nanosheet Gas Sensors for Parts per Billion-Level Detection of Acetone. *ACS Appl. Mater. Interfaces* **12**, 51637-51644 (2020).

[5] Sawa, A., Resistive Switching in Transition Metal Oxides. *Mater. Today* **11**, 28-36 (2008).

[6] Yuan, C.Z.*, et al.*, Mixed Transition-Metal Oxides: Design, Synthesis, and Energy-Related Applications. *Angew. Chem. Int. Edit.* **53**, 1488-1504 (2014).

[7] Fujishima, A. and K. Honda, Electrochemical Photolysis of Water at a Semiconductor Electrode. *Nature* **238**, 37-38 (1972).

[8] Bolzan, A.A.*, et al.*, Structural Studies of Rutile-Type Metal Dioxides. *Acta Crystallogr. B* **53**, 373-380 (1997).

[9] Hanaor, D.A.H. and C.C. Sorrell, Review of The Anatase to Rutile Phase Transformation. *J. Mater. Sci.* **46**, 855-874 (2011).

[10] Cui, Z.H., F. Wu, and H. Jiang, First-principles Study of Relative Stability of Rutile and Anatase TiO_2 Using the Random Phase Approximation. *Phys. Chem. Chem. Phys.* **18**, 29914-29922 (2016).

[11] Dette, C.*, et al.*, TiO_2 Anatase with a Bandgap in the Visible Region. *Nano Lett.* **14**, 6533-6538 (2014).

[12] Daghrir, R., P. Drogui, and D. Robert, Modified TiO_2 For Environmental Photocatalytic Applications: A Review. *Ind. Eng. Chem. Res.* **52**, 3581-3599 (2013).

[13] Schneider, J.*, et al.*, Understanding TiO_2 Photocatalysis: Mechanisms and Materials. *Chem. Rev.* **114**, 9919-9986 (2014).

[14] Lan, Y.C., Y.L. Lu, and Z.F. Ren, Mini Review on Photocatalysis of Titanium Dioxide Nanoparticles and Their Solar Applications. *Nano Energy* **2**, 1031-1045 (2013).

[15] Arroyo-de Dompablo, M.E., A. Morales-Garcia, and M. Taravillo, DFT+*U* Calculations of Crystal Lattice, Electronic Structure, and Phase Stability under Pressure of TiO_2 Polymorphs. *J. Chem. Phys.* **135**, 054503 (2011).

[16] Hu, Y.X.*, et al.*, Lattice Distortion Induced Internal Electric Field in TiO_2 Photoelectrode for Efficient Charge Separation and Transfer. *Nat. Commun.* **11**, 2129 (2020).

[17] Rahimi, N., R.A. Pax, and E.M. Gray, Review of Functional Titanium Oxides. I: TiO_2 and Its Modifications. *Prog Solid State Ch* **44**, 86-105 (2016).

[18] Luttrell, T.*, et al.*, Why Is Anatase a Better Photocatalyst Than Rutile? - Model Studies on Epitaxial TiO_2 Films. *Sci. Rep.* **4**, 4043 (2014).

[19] Nishikawa, M.*, et al.*, Effect of Lattice Distortion on Photocatalytic Performance of TiO_2. *Catal. Lett.* **147**, 292-300 (2017).

[20] Zhou, W.*, et al.*, Band Gap Engineering of SnO_2 by Epitaxial Strain: Experimental and Theoretical Investigations. *J. Phys. Chem. C.* **118**, 6448-6453 (2014).

[21] Kamarulzaman, N.*, et al.*, Anomalies in Wide Band Gap SnO_2 Nanostructures. *J. Solid State Chem.* **277**, 271-280 (2019).

[22] Mishra, K.C., K.H. Johnson, and P.C. Schmidt, Electronic Structure of Antimony-doped Tin Oxide. *Phys. Rev. B* **51**, 13972-13976 (1995).

[23] Williamson, B.A.*, et al.*, Resonant Ta Doping for Enhanced Mobility in

Transparent Conducting SnO_2. *Chem. Mater.* **32**, 1964-1973 (2020).

[24] Dixon, S.C.*, et al.*, n-Type Doped Transparent Conducting Binary Oxides: an Overview. *J. Mater. Chem. C* **4**, 6946-6961 (2016).

[25] Das, S. and V. Jayaraman, SnO_2: A Comprehensive Review on Structures and Gas Sensors. *Prog. Mater. Sci* **66**, 112-255 (2014).

[26] Xiong, L.*, et al.*, Review on the Application of SnO_2 in Perovskite Solar Cells. *Adv. Funct. Mater.* **28**, 1802757 (2018).

[27] Sun, C.*, et al.*, Recent Intensification Strategies of SnO_2-based Photocatalysts: A Review. *Chem. Eng. J.* **427**, 131564 (2022).

[28] Morin, F.J., Oxides Which Show a Metal-to-Insulator Transition at the Neel Temperature. *Phys. Rev. Lett.* **3**, 34-36 (1959).

[29] Srivastava, A.*, et al.*, Selective Growth of Single Phase VO_2 (A, B, and M) Polymorph Thin Films. *APL Mater.* **3**, 026101 (2015).

[30] Cao, J.*, et al.*, Extended Mapping and Exploration of the Vanadium Dioxide Stress-Temperature Phase Diagram. *Nano Lett.* **10**, 2667-2673 (2010).

[31] Zylbersztejn, A. and N.F. Mott, Metal-Insulator Transition in Vanadium Dioxide. *Phys. Rev. B* **11**, 4383 (1975).

[32] Cui, Y.*, et al.*, Thermochromic VO_2 for Energy-Efficient Smart Windows. *Joule* **2**, 1707-1746 (2018).

[33] Gao, Y.*, et al.*, Nanoceramic VO_2 Thermochromic Smart Glass: A Review on Progress in Solution Processing. *Nano Energy* **1**, 221-246 (2012).

[34] Li, G.*, et al.*, Photo-Induced Non-Volatile VO_2 Phase Transition for Neuromorphic Ultraviolet Sensors. *Nat. Commun.* **13**, 1729 (2022).

[35] Jung, Y.*, et al.*, Observation of Optically Addressable Nonvolatile Memory in VO_2 at Room Temperature. *Adv. Electron. Mater.* **7**, 2001142 (2021).

[36] Goodenough, J.B., The Two Components of the Crystallographic Transition in VO_2. *J. Solid State Chem.* **3**, 490-500 (1971).

[37] Nájera, O.*, et al.*, Resolving the VO_2 Controversy: Mott Mechanism Dominates

the Insulator-to-Metal Transition. *Phys. Rev. B* **95**, 035113 (2017).

[38] Cocker, T.*, et al.*, Phase Diagram of the Ultrafast Photoinduced Insulator-Metal Transition in Vanadium Dioxide. *Phys. Rev. B* **85**, 155120 (2012).

[39] Lee, D.*, et al.*, Deposition-Temperature-Mediated Selective Phase Transition Mechanism of VO_2 Films. *J. Phys. Chem. C.* **124**, 17282-17289 (2020).

[40] Hsieh, W.-P.*, et al.*, Evidence for Photo-Induced Monoclinic Metallic VO_2 under High Pressure. *Appl. Phys. Lett.* **104**, 021917 (2014).

[41] Li, Z.*, et al.*, Imaging Metal-like Monoclinic Phase Stabilized by Surface Coordination Effect in Vanadium Dioxide Nanobeam. *Nat. Commun.* **8**, 1-7 (2017).

[42] Inturi, S.N.R.*, et al.*, Visible-Light-Induced Photodegradation of Gas Phase Acetonitrile using Aerosol-Made Transition Metal (V, Cr, Fe, Co, Mn, Mo, Ni, Cu, Y, Ce, and Zr) doped TiO_2. *Appl. Catal. B: Environ.* **144**, 333-342 (2014).

[43] Nair, R.V.*, et al.*, A Review on Optical Bandgap Engineering in TiO_2 Nanostructures via Doping and Intrinsic Vacancy Modulation Towards Visible Light Applications. *J. Phys. D: Appl. Phys.* **55**, 313003 (2022).

[44] Sato, K.*, et al.*, Highly Textured SnO_2: F TCO Films for a-Si Solar Cells. *Asahi Garasu Kenkyu Hokoku* **42**, 129-137 (1993).

[45] Montero, J., J. Herrero, and C. Guillén, Preparation of Reactively Sputtered Sb-doped SnO_2 Thin Films: Structural, Electrical and Optical Properties. *Sol. Energy Mater. Sol. Cells* **94**, 612-616 (2010).

[46] Liu, K.*, et al.*, Recent Progresses on Physics and Applications of Vanadium Dioxide. *Mater. Today* **21**, 875-896 (2018).

[47] Pouget, J. and H. Launois, Metal-insulator phase transition in VO_2. *Le Journal de Physique Colloques* **37**, C4-49-C4-57 (1976).

[48] Rakotoniaina, J.*, et al.*, The Thermochromic Vanadium Dioxide: I. Role of Stresses and Substitution on Switching Properties. *J. Solid State Chem.* **103**, 81-94 (1993).

[49] Gu, Q.*, et al.*, Current-Driven Phase Oscillation and Domain-Wall Propagation in $W_xV_{1-x}O_2$ Nanobeams. *Nano Lett.* **7**, 363-366 (2007).

[50] Fujimoto, T. and K. Awaga, Electric-Double-Layer Field-Effect Transistors with Ionic Liquids. *Phys. Chem. Chem. Phys.* **15**, 8983-9006 (2013).

[51] Yuan, H.*, et al.*, High‐Density Carrier Accumulation in ZnO Field‐Effect Transistors Gated by Electric Double Layers of Ionic Liquids. *Adv. Funct. Mater.* **19**, 1046-1053 (2009).

[52] Du, H.*, et al.*, Electric Double-Layer Transistors: a Review of Recent Progress. *J. Mater. Sci.* **50**, 5641-5673 (2015).

[53] Katase, T.*, et al.*, A Transparent Electrochromic Metal-Insulator Switching Device with Three-Terminal Transistor Geometry. *Sci. Rep.* **6**, 25819 (2016).

[54] Leighton, C., Electrolyte-Based Ionic Control of Functional Oxides. *Nat. Mater.* **18**, 13-18 (2019).

[55] Zhang, X.*, et al.*, Solid-State Electrochemical Switch of Superconductor–Metal–Insulators. *ACS Appl. Mater. Interfaces* **13**, 54204-54209 (2021).

[56] Yang, Q.*, et al.*, Solid-State Electrochemical Protonation of $SrCoO_{2.5}$ into $H_xSrCoO_{2.5}$ (x= 1, 1.5, and 2). *ACS Appl. Electron. Mater.* **3**, 3296-3300 (2021).

[57] Kim, G., H.J. Cho, and H. Ohta, Reversible Redox Control of Optoelectronic Properties of Hexagonal Tungsten Oxide Epitaxial Films Grown on YSZ Solid Electrolyte. *ACS Appl. Electron. Mater.* **3**, 3619-3624 (2021).

[58] Schladt, T.D.*, et al.*, Crystal-Facet-Dependent Metallization in Electrolyte-Gated Rutile TiO_2 Single Crystals. *ACS Nano* **7**, 8074-8081 (2013).

[59] Liang, D.*, et al.*, Optimization of Two-Dimensional Channel Thickness in Nanometer-Thick SnO_2-Based Top-Gated Thin-Film Transistors using Electric Field Thermopower Modulation: Implications for Flat-Panel Displays. *ACS Appl. Nano Mater.* **3**, 12427-12432 (2020).

[60] Liang, D.D.*, et al.*, Thickness Optimization toward High-Performance Bottom-

Gated Transparent Tin Dioxide Thin-Film Transistors. *ACS Appl. Electron. Mater.* **2**, 3454-3458 (2020).

[61] Lee, Y.J.*, et al.*, Nonvolatile Control of Metal–Insulator Transition in VO_2 by Ferroelectric Gating. *Adv. Mater.* **34**, 2203097 (2022).

[62] Jeong, J.*, et al.*, Suppression of Metal-Insulator Transition in VO_2 by Electric Field-Induced Oxygen Vacancy Formation. *Science* **339**, 1402-1405 (2013).

[63] Shibuya, K. and A. Sawa, Modulation of Metal-Insulator Transition in VO_2 by Electrolyte Gating-Induced Protonation. *Adv. Electron. Mater.* **2**, 1500131 (2016).

[64] Li, G.*, et al.*, Flexible VO_2 Films for In‐Sensor Computing with Ultraviolet Light. *Adv. Funct. Mater.* 2203074 (2022).

[65] Thomas, N., Crystal Structure-Physical Property Relationships in Perovskites. *Acta Crystallogr. B* **45**, 337-344 (1989).

[66] Zhu, C.*, et al.*, Strain Engineering in Perovskite Solar Cells and its Impacts on Carrier Dynamics. *Nat. Commun.* **10**, 815 (2019).

[67] Aetukuri, N.B.*, et al.*, Control of the Metal–Insulator Transition in Vanadium Dioxide by Modifying Orbital Occupancy. *Nat. Phys.* **9**, 661-666 (2013).

[68] Chen, B.*, et al.*, Orthorhombic Distortion-Induced Anatase-like Optoelectronic Properties of Rutile TiO_2. *J. Appl. Phys.* **132**, 185301 (2022).

[69] Chen, B.*, et al.*, Room Temperature Insulator-to-Metal Transition of VO_2/TiO_2 Epitaxial Bilayer Films Grown on M-plane Sapphire Substrates. *Adv. Electron. Mater.* **8**, 2100687 (2022).

[70] Chae, S.*, et al.*, Germanium Dioxide: A New Rutile Substrate for Epitaxial Film Growth. *J. Vac. Sci. Technol. A* **40**, 050401 (2022).

[71] Silva, V.F.*, et al.*, Substrate-Controlled Allotropic Phases and Growth Orientation of TiO_2 Epitaxial Thin Films. *J. Appl. Crystallogr.* **43**, 1502-1512 (2010).

[72] Strelcov, E.*, et al.*, Doping-Based Stabilization of the M2 Phase in Free-Standing VO_2 Nanostructures at Room Temperature. *Nano Lett.* **12**, 6198-6205 (2012).

[73] Muraoka, Y. and Z. Hiroi, Metal–Insulator Transition of VO_2 Thin Films Grown on TiO_2 (001) and (110) Substrates. *Appl. Phys. Lett.* **80**, 583-585 (2002).

[74] Shibuya, K.*, et al.*, Fabrication and Raman Scattering Study of epitaxial VO_2 films on MgF_2 (001) Substrates. *Appl. Phys. Lett.* **103**, 021604 (2013).

[75] Li, J. and J. Dho, Controlling Metal–Insulator Transition in the Hetero-Epitaxial VO_2/TiO_2 Bilayer Grown on Al_2O_3. *J. Cryst. Growth* **312**, 3287-3291 (2010).

[76] Moore, C.H., Formation and properties of single crystals of synthetic rutile. *Trans. Am. Institute of Mining, Metallurgical and Petroleum Engineers* **184**, 194 (1949).

[77] Nagashima, K.*, et al.*, Stress Relaxation Effect on Transport Properties of Strained Vanadium Dioxide Epitaxial Thin Films. *Phys. Rev. B* **74**, 172106 (2006).

[78] Rodriguez, L.*, et al.*, Self-Pixelation Through Fracture in VO_2 Thin Films. *ACS Appl. Electron. Mater.* **2**, 1433-1439 (2020).

[79] Sohn, A.*, et al.*, Visualization of Local Phase Transition Behaviors near Dislocations in Epitaxial VO_2/TiO_2 thin films. *Appl. Phys. Lett.* **107**, 171603 (2015).

[80] Yajima, T.*, et al.*, Drastic Change in Electronic Domain Structures via Strong Elastic Coupling in VO_2 Films. *Phys. Rev. B* **91**, 205102 (2015).

[81] Sandiumenge, F.*, et al.*, Metallic Diluted Dimerization in VO_2 Tweeds. *Adv. Mater.* **33**, 2004374 (2021).

[82] Kawatani, K., T. Kanki, and H. Tanaka, Formation Mechanism of a Microscale Domain and Effect on Transport Properties in Strained VO_2 Thin Films on TiO_2(001). *Phys. Rev. B* **90**, 054203 (2014).

[83] Paik, H.*, et al.*, Transport Properties of Ultra-Thin VO_2 Films on (001) TiO_2 Grown by Reactive Molecular-Beam Epitaxy. *Appl. Phys. Lett.* **107**, 163101

(2015).

[84] Lee, D.*, et al.*, Sharpened VO_2 Phase Transition via Controlled Release of Epitaxial Strain. *Nano Lett.* **17**, 5614-5619 (2017).

[85] Chen, X.*, et al.*, A Near-Field Study of VO_2/(100)TiO_2 Film and its Crack-Induced Strain Relief. *Appl. Phys. Lett.* **121**, 021902 (2022).

Chapter 2. Room Temperature Insulator-to-Metal Transition of VO_2/TiO_2 Epitaxial Bilayer Films Grown on M-plane Sapphire Substrates

2.1. Objective of this chapter

Vanadium dioxide (VO_2) shows first-order phase transition from monoclinic phase to tetragonal rutile phase. Due to the different optoelectronic properties of these two phases, VO_2 is a promising candidate as the active materials of thermochromic smart windows, bolometer, etc [1, 2]. However, the T_c of bulk VO_2 is rather high 341 K (68 °C) and therefore, needs to be decreased down to near temperature for practical applications. Although T_c can be reduced to room temperature (RT) if rutile TiO_2 crystal is used as the substrate [3], it is not technologically viable for large scale applications because of the size limitation of available TiO_2 crystal [4].

To overcome this issue, materials applicable in optical applications, which can also be synthesized in large-scale, is required as the substrate to support the growth of VO_2. In this regard, α-Al_2O_3 shows excellent transmittance in both visible and infrared light. The large-scale synthesis of α-Al_2O_3 is also allowed by various growth techniques [5, 6]. Moreover, $(1\bar{1}00)$-oriented α-Al_2O_3 is verified to support the epitaxial growth of rutile TiO_2 films [7, 8]. Therefore, the T_c of VO_2 films on TiO_2 buffered α-Al_2O_3 would be of

interest to the optoelectronics community since it can potentially provide an important step towards realizing practical VO_2-based devices.

In this chapter, the effectiveness of TiO_2-buffered α-Al_2O_3 substrates on the reduction of T_c of VO_2 were verified by fabricating VO_2 films with different thickness on 200-nm-thick TiO_2-buffered $(1\bar{1}00)$ α-Al_2O_3 substrates (**Figure 2-1(a)**). The 5.5-nm-thick VO_2 film on 200-nm-thick TiO_2-buffered sapphire substrate showed clear insulator-to-metal transition at a near room temperature of ~305 K (32 °C). Additionally, a strain induced orthorhombic distortion were observed. To further investigate such distortion on insulator-to-metal transition (IMT) behavior of VO_2, VO_2/TiO_2 bilayer films with varied TiO_2 thicknesses were fabricated as shown in **Figure 2-1(b)**. experimental results demonstrate that the IMT behavior is sensitive to the orthorhombic distortion. Extremely large distortion will suppress the IMT of VO_2, due to the carrier generation. This systematic study on the effect of in-plane lattice distortion on the insulator-to-metal transition of VO_2 would be useful for the practical application of VO_2 as an active material of smart window.

2.2. Experimental

***Sample preparation*:** The bilayer films of VO_2/TiO_2 were grown on $(1\bar{1}00)$ α-Al_2O_3 substrate by pulsed laser deposition (PLD) method. Firstly, rutile TiO_2 layer was

deposited on $(1\bar{1}00)$ α-Al_2O_3 (10 × 10 × 0.5 mm) substrates at 500 °C in an oxygen atmosphere of 1.5 Pa by irradiating a KrF excimer laser (λ = 248 nm, fluence ~ 0.8 J cm^{-2} $pulse^{-1}$, repetition rate = 10 Hz) on a ceramic TiO_2 target. To minimize the interdiffusion between VO_2 and TiO_2 layer and keep the magnitude and sharpness of the metal-to-insulator transition, the deposition temperature of VO_2 layer was set at 450 °C, slightly lower than that of TiO_2 deposition while other conditions remained unchanged.

***Crystallographic analyses*:** The film thickness, crystallographic orientation, and lattice parameters were analyzed by using the high-resolution X-ray diffraction (XRD, ATX-G, Rigaku Co.) with Cu $K\alpha_1$ (λ = 0.154059 nm) radiation. All measurements were performed at room temperature.

Electrical property measurements: Electrical resistivity, carrier concentration, and Hall mobility were measured by dc four-probe methods with van der Pauw electrode configuration in air. Thermopower was measured by the steady-state method. A temperature difference of 3 − 4 K was generated by a pair of Peltier devices under the specimen. The resulting thermoelectromotive force (ΔV) and temperature difference (ΔT) were measured by a digital multimeter (R6552, Advantest Co.) and two thermocouples, respectively. Thermopower (S) was calculated from the slope of $\Delta V - \Delta T$ plots.

2.3. Result and discussion

Figure 2-2(a) shows the out-of-plane XRD patterns of the resultant VO_2 films (thickness: 5.5 − 40 nm) grown on ~200-nm-thick TiO_2 buffered $(1\bar{1}00)$ α-Al_2O_3 single crystal substrates. Intense diffraction peaks of 002 TiO_2, 002 VO_2, and $3\bar{3}00$ α-Al_2O_3 are seen at q_z = 6.76 nm^{-1}, 6.98 nm^{-1}, and 7.28 nm^{-1}, respectively, indicating strong 00*l* orientation of the VO_2/TiO_2 bilayer. No other peak is detected in the wide range XRD pattern (**Figure 2-3**), indicating no other preferential orientation in all samples. The out-of-plane diffraction peak position of VO_2 is insensitive to the thickness, which is due to the asymmetric biaxial strain in the in-plane direction we will discuss later. Noting that the slight random shift of peaks may be due to the interference of the VO_2 and TiO_2 peaks [9].

To clarify the lattice strain in VO_2 films, the in-plane XRD measurements were performed for the resultant films. **Figure 2-2(b)** shows the in-plane XRD patterns of (upper) 28-nm-thick and (lower) 5.5-nm-thick VO_2 on 200-nm-thick TiO_2 buffered $(1\bar{1}00)$ α-Al_2O_3 substrates. Only intense diffraction peaks of 040 and 400 VO_2/TiO_2 are seen together with $22\bar{4}0$ and $000\underline{12}$ α-Al_2O_3, respectively, indicating that heteroepitaxial growth of VO_2/TiO_2 bilayer occurred with an epitaxial relationship of (001)[010] VO_2||(001) TiO_2||$(1\bar{1}00)$[0001] α-Al_2O_3. It should be noted that the diffraction peak position of 400 and 040 is different when VO_2 is 5.5 nm (**Figure 2-2(b) lower**),

indicating orthorhombic distortion due to the asymmetric in-plane lattice parameters of $(1\bar{1}00)$ α-Al_2O_3 (**Figure 2-2(c)**). The peak positions of 400 and 040 gradually approach the same position ($q/2\pi$ ~8.8 nm^{-1}) with increasing thickness, suggesting lattice relaxation occurs when VO_2 is 28 nm (**Figure 2-2(b) upper**).

Figure 2-4 summarizes the changes in the lattice parameters and distortion of VO_2 films. The out-of-plane lattice parameter *c* is almost constant at ~0.286 nm, whereas the in-plane lattice parameters *a* and *b* show decreasing tendencies with increasing VO_2 thickness until the VO_2 thickness reaches 20 nm. When the VO_2 thickness is thicker than 20 nm, *a* and *b* lattice parameters become constant (~0.455 nm). Here the ratio of in-plane lattice parameters, *b*/*a* was defined as a metric to quantify the distortion (**Figure 2-4(c)**) to visualize the in-plane lattice distortion. The *b*/*a* decreases with increasing thickness when the VO_2 thickness is thinner than 20 nm, indicating that the lattice of thinner VO_2 film is largely distorted in this regime.

In order to further increase the lattice distortion, 10-nm-thick VO_2 films were grown on the 10 − 200-nm-thick TiO_2 buffers on $(1\bar{1}00)$ α-Al_2O_3 substrates. The lattice parameters and distortion *b*/*a* are shown in **Figure 2-4(b)** and **4(d)**, respectively. As TiO_2 thickness decreases, the difference between lattice parameters *a* and *b* further increases, ranging from ~1.005 to 1.027.

Figure 2-5 summarizes the temperature dependences of the electrical resistivity (ρ) of the resultant VO_2 films grown on TiO_2-buffered $(1\bar{1}00)$ α-Al_2O_3 substrates. Insulator-to-metal transition behavior is clearly observed in most cases (**Figure 2-5(a)** and **5(c)**) with clockwise hysteresis. It should be noted that the T_c systematically changed with the thickness of VO_2 (**Figure 2-5(a)**, on 200-nm-thick TiO_2) and TiO_2 (**Figure 2-5(b)**, VO_2 thickness is fixed at 10 nm). **Figure 2-5(b)** and **2-5(d)** visualize the T_c and hysteresis width (ΔT_c) as a function of the VO_2 thickness and the TiO_2 thickness, respectively. The T_c gradually decreases from ~320 (~47 °C) to ~305 K (~32 °C) with decreasing the VO_2 thickness from 40 to 5.5 nm (**Figure 2-5(b) upper**). The lowest T_c of 32 °C is similar to that of VO_2 films grown on TiO_2 substrate [10, 11]. Thus, the T_c was successfully reduced to near RT using 200-nm-thick TiO_2-buffered $(1\bar{1}00)$ α-Al_2O_3 as the substrates. Since T_c gradually increases with decreasing TiO_2 thickness (**Figure 2-5(d) upper**), thicker TiO_2 buffer layer needs to be used to reduce T_c.

On the other hand, when VO_2 thickness is thicker than 10 nm, ΔT_c is almost constant (~4 K) whereas it increases when thickness is thinner than 10 nm (**Figure 2-5(b) lower**). Further, ΔT_c slightly decreases with decreasing TiO_2 thickness (**Figure 2-5(d) lower**), and the resistivity ratio of insulating phase/metallic phase of 10-nm-thick VO_2 film on thinner (10 nm) TiO_2-buffered $(1\bar{1}00)$ α-Al_2O_3 substrate is small (~10^1) as compared to the others ($10^3 - 10^4$). To clarify the origin of the small resistivity ratio, the temperature dependence of thermopower (S) of the VO_2 films was measured (**Figure 2-6(a)** and

6(b)) since *S* is a great measure of the carrier concentration; All samples show negative *S* indicating that the majority carrier is electrons; |*S*| decreases with increasing carrier concentration [12, 13]. Similar to the resistivity, clockwise change of |*S*| is observed in all cases except the 10-nm-thick VO_2 film on 10-nm-thick TiO_2-buffered $(1\bar{1}00)$ α-Al_2O_3 substrate. |*S*| of the 10-nm-thick VO_2 film on 10-nm-thick TiO_2-buffered $(1\bar{1}00)$ α-Al_2O_3 substrate is always small (~30 μV K^{-1}) as compared to the other samples, which show drastic change in |*S*| from ~500 (insulating phase) to ~30 μV K^{-1} (metallic phase). These results suggest that carrier concentration of the 10-nm-thick sample is much higher than the other samples.

Here, a discussion of the origin of the carrier generation in the 10-nm-thick sample was proposed. As shown in **Figure 2-4(c)** and **4(d)**, there is an in-plane lattice distortion in the VO_2 films. The 10-nm-thick sample showed largest distortion (b/a = 1.027). A hypothesis that in-plane lattice distortion induced oxygen vacancy generation occurred was raised [14]; introduction of oxygen vacancy in VO_2 would originate carrier generation. In order to clarify the hypothesis, the Hall effect measurements of the VO_2 samples were performed at room temperature. Notably, the results show that distorted VO_2 is still n-type semiconductor with electrons as the majority carrier, which is consistent with the result of thermopower measurement. **Figure 7** plots the observed carrier (electron) concentration and Hall mobility as a function of the lattice distortion. With increasing the lattice distortion, the carrier concentration drastically increases and

the Hall mobility slightly decreases. Based on these results, it was concluded that the carrier concentration of VO_2 film increases when the TiO_2 buffer layer is thin due to large lattice distortion.

2.4. Conclusion

In this study, it was found that the T_c of VO_2 films can be reduced to near room temperature by using M-plane sapphire as the substrate. VO_2/TiO_2 bilayer films with varied thicknesses were fabricated on $(1\bar{1}00)$ α-Al_2O_3 substrates. The 5.5-nm-thick VO_2 film on 200-nm-thick TiO_2 buffered sapphire substrate showed clear insulator-to-metal transition at ~305 K (32 °C). It was also found that the insulator-to-metal transition is sensitive to the in-plane lattice distortion, which induces carrier generation. The systematic study of this chapter on the effect of in-plane lattice distortion on the insulator-to-metal transition of VO_2 would be useful for the practical application of VO_2 as an active material of smart window.

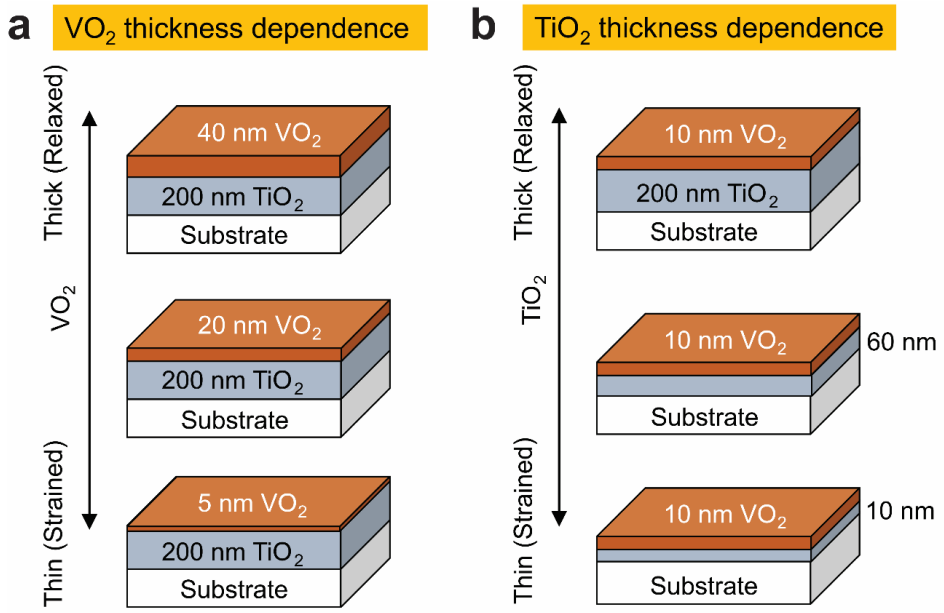

Figure 2-1. Hypothesis of the lattice mismatch induced strain of VO_2 epitaxial films. (a) VO_2 films on 200-nm-thick TiO_2 epitaxial films. (b) 10-nm-thick VO_2 films on TiO_2 epitaxial films with various thicknesses. It was expected that the VO_2/TiO_2 bilayer films are highly strained when both layers are extremely thin, and the strain would significantly affect the insulator-to-metal transition of VO_2 epitaxial films.

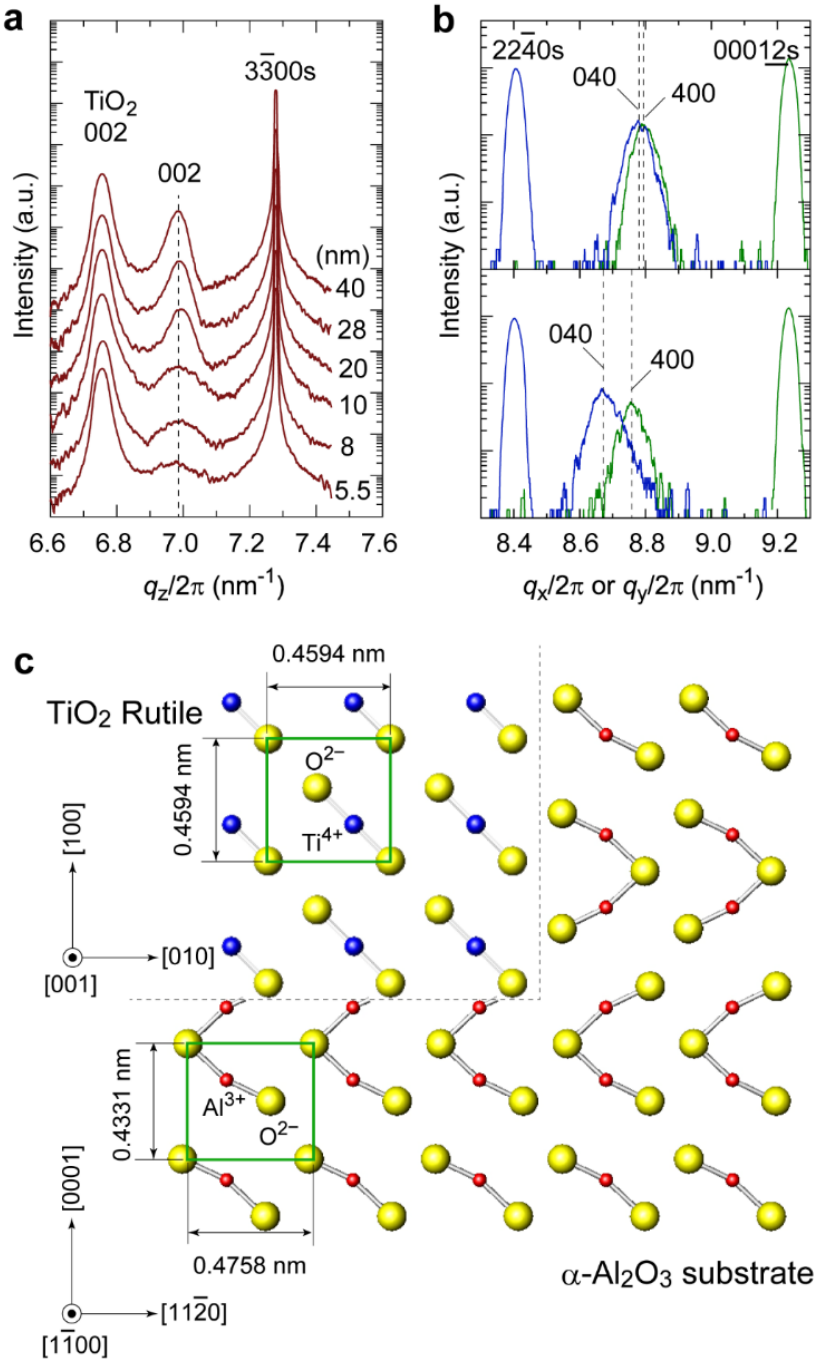

Figure 2-2. Crystallographic orientation and lattice mismatch. (a) Out-of-plane XRD patterns of the VO_2 (5.5 − 40 nm)/TiO_2 (200 nm) epitaxial bilayer on $(1\bar{1}00)$ α-Al_2O_3 substrate. The diffraction peak position of 002 VO_2 is independent of the thickness. (b) In-plane XRD patterns of (upper) 28-nm-thick VO_2/TiO_2 (200 nm) bilayer and (lower) 5.5-nm-thick VO_2/TiO_2 (200 nm) bilayer films on $(1\bar{1}00)$ α-Al_2O_3 substrate. The dashed lines indicate the diffraction peak positions of VO_2 layer. (c) The epitaxial relationship between (001) rutile TiO_2 and $(1\bar{1}00)$ α-Al_2O_3.

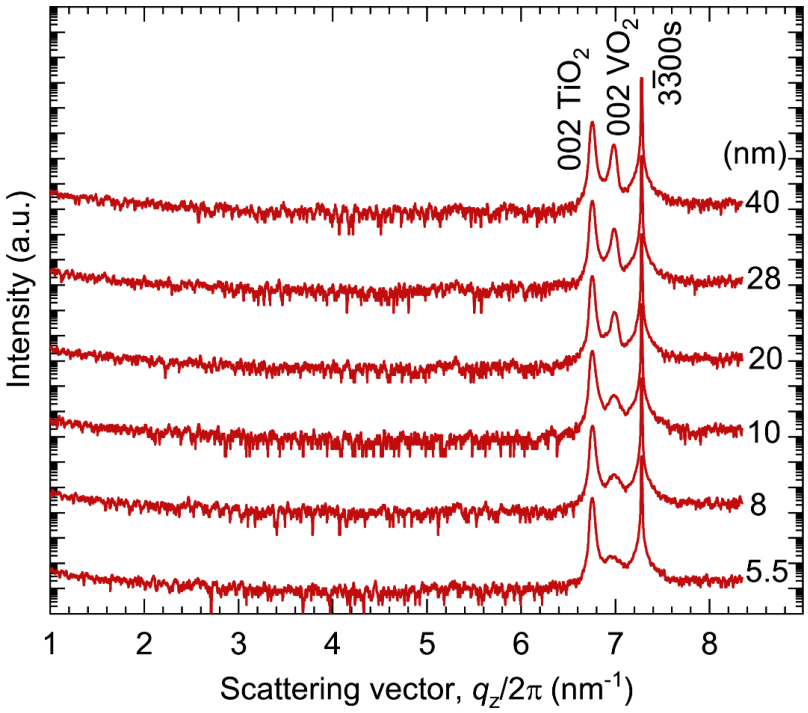

Figure 2-3. Out-of-plane XRD patterns of the 5.5 − 40-nm-thick VO_2 films on 200-nm-thick TiO_2-buffered $(1\bar{1}00)$ α-Al_2O_3 substrates. Only three diffraction peaks are detected.

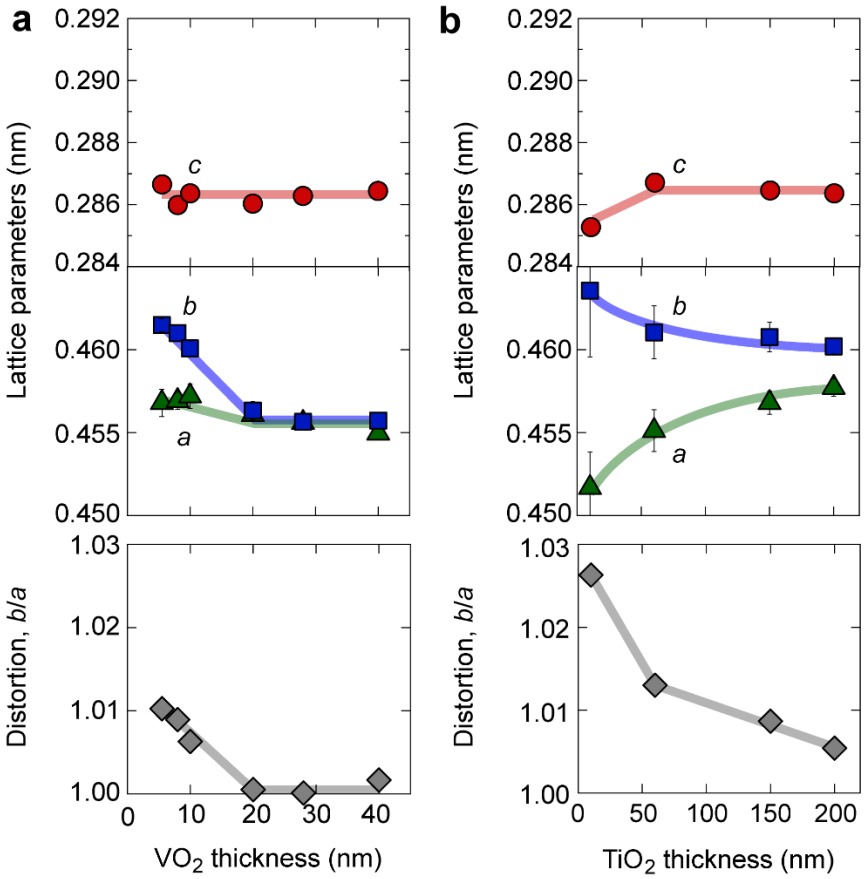

Figure 2-4. Lattice parameters and distortions. VO_2-thickness dependence of (a) the lattice parameters and (c) distortion of VO_2 epitaxial films grown on 200-nm-thick TiO_2 films. TiO_2-thickness dependence of (a) the lattice parameters and (c) distortion of 10-nm-thick VO_2 epitaxial films grown on TiO_2 films with various thicknesses. The lattice parameters are extracted from XRD patterns of Figure 2-2 and 2-3. The distortion is defined as the ratio of in-plane lattice parameters, *b*/*a*.

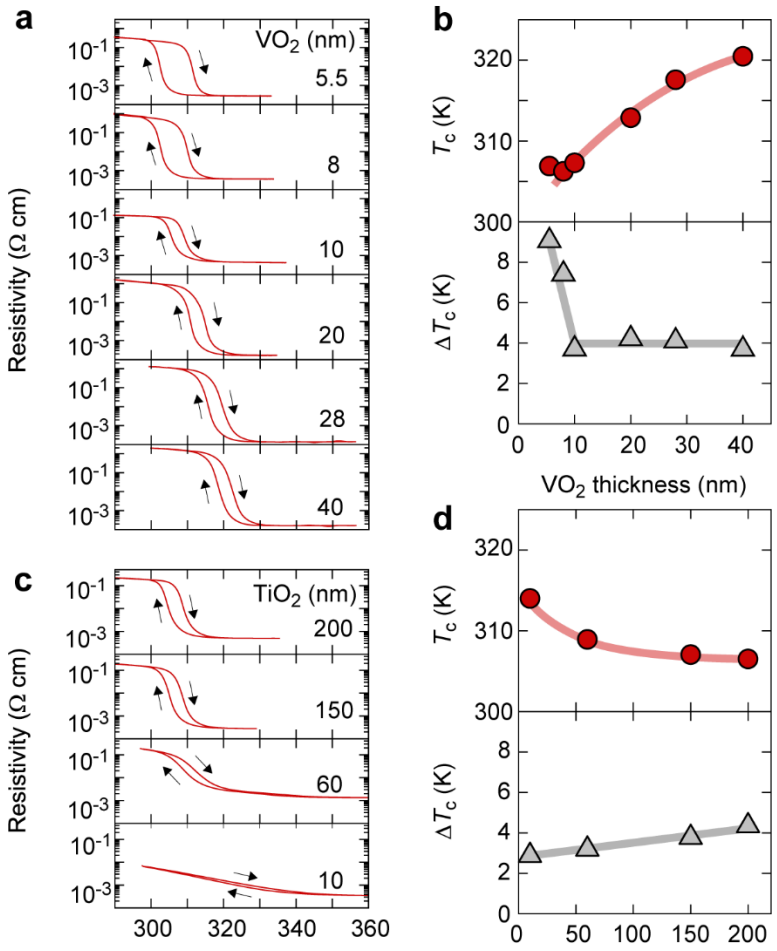

Figure 2-5. Electrical resistivity. (a) Temperature dependences of electrical resistivity (ρ), (b, upper) metal-to-insulator transition temperature (T_c), and (b, lower) thermal hysteresis width (ΔT_c) of VO_2 films (5.5 − 40 nm) on 200-nm-thick TiO_2 films. The arrows indicate the direction of the hysteresis is clockwise. T_c and ΔT_c are defined as average and difference of $T_{c,\,cooling}$ and $T_{c,\,heating}$, respectively. $T_{c,\,cooling}$ and $T_{c,\,heating}$ are extracted from $\rho-T$ curve. The T_c gradually increases with VO_2 thickness, whereas ΔT_c drops from ~9 K to ~4 K when thickness increases from 5.5 nm to 10 nm. (c) Temperature dependences of ρ, (d, upper) T_c, and (d, lower) ΔT_c of 10-nm-thick VO_2 films on TiO_2 films with various thicknesses. The T_c gradually decreases with TiO_2 thickness, whereas ΔT_c slightly increases from ~3 K to ~4.5 K.

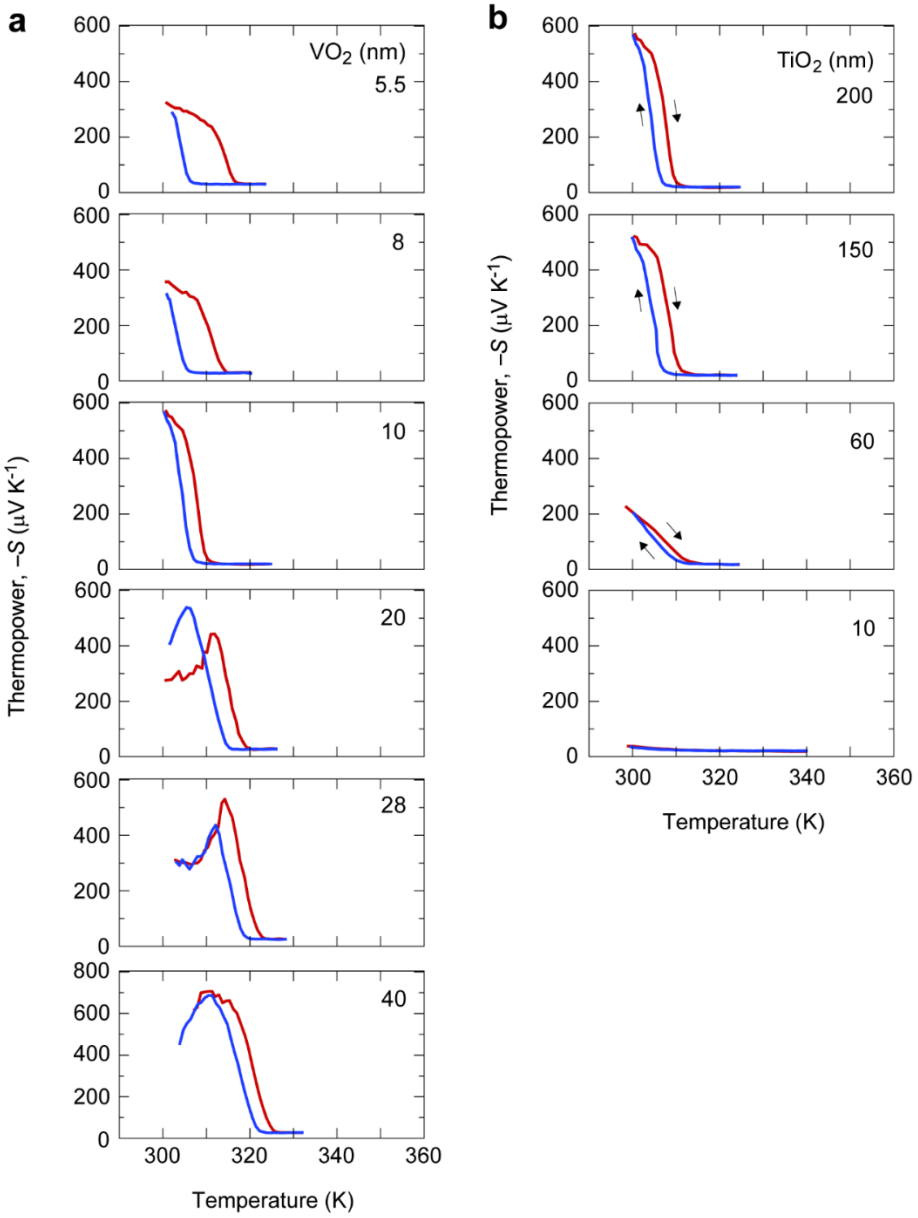

Figure 2-6. Thermopower. (a) Temperature dependence of thermopower (S) of VO_2 films (5.5 − 40 nm) on 200-nm-thick TiO_2 films. The absolute value of thermopower is small when VO_2 thickness is thinner than 10 nm. (b) Temperature dependence of thermopower (S) of 10-nm-thick VO_2 films on TiO_2 films with various thicknesses. The absolute value of thermopower decreases with decreasing TiO_2 thickness. The red and blue lines correspond to the heating and cooling process, respectively.

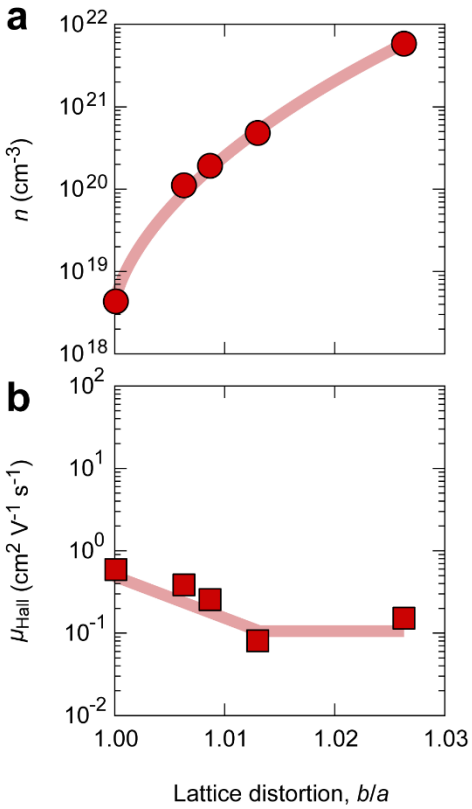

Figure 2-7. Lattice distortion induced carrier generation. (a) Carrier concentration (n) and (b) Hall mobility (μ_{Hall}) of the 10 nm VO_2 films grown on 10-, 60-, 150-, and 200-nm-thick TiO_2-buffered $(1\bar{1}00)$ α-Al_2O_3 substrates as the function of lattice distortion b/a. The point of the slightly distorted VO_2 (b/a = ~1) is 28-nm-thick VO_2/200-nm-thick TiO_2 sample, which is used for reference.

References

[1] Gao, Y.*, et al.*, Nanoceramic VO_2 Thermochromic Smart Glass: A Review on Progress in Solution Processing. *Nano Energy* **1**, 221-246 (2012).

[2] Liu, K.*, et al.*, Recent Progresses on Physics and Applications of Vanadium Dioxide. *Mater. Today* **21**, 875-896 (2018).

[3] Muraoka, Y. and Z. Hiroi, Metal–Insulator Transition of VO_2 Thin Films Grown on TiO_2 (001) and (110) Substrates. *Appl. Phys. Lett.* **80**, 583-585 (2002).

[4] Moore, C.H., Formation and properties of single crystals of synthetic rutile. *Trans. Am. Institute of Mining, Metallurgical and Petroleum Engineers* **184**, 194 (1949).

[5] Carter, C.B. and M.G. Norton, *Growing Single Crystals*, in *Ceramic Materials: Science and Engineering*. 2007, Springer New York: New York, NY. p. 507-526.

[6] Kurlov, V., *Sapphire: Properties, Growth, and Applications*, in *Encyclopedia of Materials: Science and Technology*. 2001, Elsevier. p. 8259-8264.

[7] Breckenfeld, E.*, et al.*, Strain Effects in Epitaxial VO_2 Thin Films on Columnar Buffer-Layer TiO_2/Al_2O_3 Virtual Substrates. *ACS Appl. Mater. Interfaces* **9**, 1577-1584 (2017).

[8] Silva, V.F.*, et al.*, Substrate-Controlled Allotropic Phases and Growth Orientation of TiO_2 Epitaxial Thin Films. *J. Appl. Crystallogr.* **43**, 1502-1512 (2010).

[9] Pesquera, D.*, et al.*, X-Ray Interference Effects on the Determination of Structural Data in Ultrathin $La_{2/3}Sr_{1/3}MnO_3$ Epitaxial Thin Films. *Appl. Phys. Lett.* **99**, 221901 (2011).

[10] Ren, H.*, et al.*, Wet-Etching Induced Abnormal Phase Transition in Highly Strained VO_2/TiO_2 (001) Epitaxial Film. *Phys. Status Solidi - Rapid Res. Lett.* **12**, 1700320 (2018).

[11] Yang, Y.*, et al.*, Thickness Effects on the Epitaxial Strain States and Phase

Transformations in (001)-VO_2/TiO_2 Thin Films. *J. Appl. Phys.* **125**, 082508 (2019).

[12] Katase, T., K. Endo, and H. Ohta, Thermopower Analysis of Metal-Insulator Transition Temperature Modulations in Vanadium Dioxide Thin Films with Lattice Distortion. *Phys. Rev. B* **92**, 035302 (2015).

[13] Katase, T., K. Endo, and H. Ohta, Thermopower Analysis of the Electronic Structure around the Metal-Insulator Transition in $V_{1-x}W_xO_2$. *Phys. Rev. B* **90**, 161105(R) (2014).

[14] Tyunina, M., *et al.*, Epitaxial Growth of Perovskite Oxide Films Facilitated by Oxygen Vacancies. *J. Mater. Chem. C* **9**, 1693-1700 (2021).

Chapter 3. Suppression of Strain Relaxation in VO_2/TiO_2 Multilayered Films

3.1. Objective of this chapter

As noted in the previous chapters, the phase transition of VO_2 occurs between insulating monoclinic phase (M-VO_2, space group: $P2_1/c$) and metallic rutile phase (R-VO_2, space group: $P4_2/mnm$) reversibly. The latter is isostructural with the rutile TiO_2. A very small lattice mismatch (~0.9%) between (001) R-VO_2 and (001) R-TiO_2 stabilizes R-VO_2 lattice at room temperature. Thus, the T_c of epitaxial VO_2 film is significantly reduced by using (001) TiO_2 substrate [1]. In addition to the use of TiO_2 substrate, the use of TiO_2 buffer layer that grown on other substrate has been experimentally proved to show the similar effect [2-4], which has been verified in previous chapter .

However, for VO_2 film grown on TiO_2 substrate, there is still an issue to be addressed; high strain condition is needed for stabilization of R-VO_2, nevertheless strain relaxation occurs when thickness exceeds a critical thickness (t_c ~15 nm). Even worse, for VO_2 grown on TiO_2, the strain is relaxed through crack formation instead of generating dislocation (**Figure 3-1(a)**). Such cracks destroy the uniformity of film and show higher resistance in local and disturbs the homogeneity of current flow, eventually resulting in the uncontrollability of IMT behavior that limits the practical optoelectronic application

of VO_2 [5-13]. To overcome this problem, deceleration of the strain relaxation should be a feasible way. To be specific, a method so-called strain compensation layer (SCL), which resists strain changes through insertion of a middle layer, has been widely studied in the InGaAs/GaAs and other zinc blende heteroepitaxial structures and demonstrated high effectiveness [14-16].

In this chapter, the SCL of TiO_2 was applied in order to maintain the strain condition of VO_2 even if the overall thickness of VO_2 films exceeds the t_c. Here, the result demonstrated that insertion of a TiO_2 overlayer between VO_2 layers (**Figure 3-1(b)**) is an excellent way to maintain the t_c around room temperature while overall VO_2 thickness exceeds ~50 nm. The present results provide a feasible method to control the crack formation and IMT behaviors of VO_2 films, which would be beneficial to the development of thermochromic device of strained VO_2.

3.2. Experimental

***VO_2/TiO_2 multilayered film growth*:** The single-layer VO_2 and multi-layer VO_2/TiO_2 were grown on (001) rutile TiO_2 single crystal substrates (10 × 10 × 0.5 mm) by pulsed laser deposition (PLD). A KrF excimer laser (λ = 248 nm, fluence ~ 1.0 J cm^{-2} $pulse^{-1}$, repetition rate = 10 Hz) was used to ablate on V_2O_5 and TiO_2 ceramic targets for the deposition of VO_2 and TiO_2 film. To facilitate the cyclic growth of multi-layer film, the

growth conditions (P_{O2} and T_{sub}) of both VO_2 and TiO_2 were fixed to 1.5 Pa and 370 °C. The thickness of each film was controlled by the deposition time and verified by X-ray reflectivity measurements. After the film growth, the film was naturally cooled to room temperature at the same pressure.

***Crystallographic analyses*:** The film thickness was measured by X-ray reflectivity (XRR). The crystallographic orientation and strain condition were analyzed by high-resolution X-ray diffraction (ATX-G, Rigaku Co.) with monochromatic Cu $K\alpha_1$ (λ = 0.154059 nm) radiation at room temperature.

***Morphology observations*:** Topographic morphologies of the resultant films were observed by atomic force microscopy (AFM, Nanocute, Hitachi Co.) at room temperature.

***Electrical resistivity measurements*:** The temperature dependence of electrical resistivity ($\rho-T$ curve) was measured by dc four-probe methods with van der Pauw electrode configuration. The temperature was controlled by using the Peltier device and measured by the K-type thermocouple mechanically attached to the sample surface.

3.3. Result and discussion

Since the growth condition may also affect the IMT behaviors of VO_2 film, for consistency, the reproduction of crack formation of VO_2 film grown on TiO_2 substrate and its effect on the IMT behavior of VO_2 were first investigated. **Figure 3-2(a)** shows the temperature dependence of resistivity ($\rho-T$) of single layer VO_2 films (upper: 8 nm, lower: 15 nm) grown on (001) TiO_2 substrate. The $\rho-T$ curves show that the clockwise IMT occurs in both films. Although the IMT behavior of 8-nm-thick VO_2 is sharp and the T_c is ~292 K, 15-nm-thick VO_2 shows a gradual and multistep IMT with T_c of ~313 K. Such multistep behavior with higher T_c is attributed to the microcrack on the VO_2 surface [5, 8, 10, 13, 17]. In order to visualize the microcrack, topographic AFM observations were performed (**Figure 3-2(b)** and **2(c)**). Rather smooth surface was observed in the case of 8-nm-thick VO_2 film with the root mean square roughness (R_{rms}) of 0.25 nm (**Figure 3-2(b)**). On the other hand, several gridded cracks were observed in the case of 15-nm-thick VO_2 film (**Figure 3-2(c)**), well consistent with its gradual and multistep IMT. Thus, the harmful effects of cracks on IMT behavior of VO_2 films has been confirmed.

Here the effectiveness of TiO_2 SCL on crack suppression and further discuss its thickness dependence on IMT behavior of VO_2 films were examined. First, a series of VO_2 (8 nm)/TiO_2 (x nm)/VO_2 (8 nm) trilayer films (x = 2, 4, 9, and 65) were

heteroepitaxially grown on (001) TiO_2 substrates under the same conditions of VO_2 single layer films. **Figure 3-3(a)** summarizes the $\rho-T$ curves of the resultant trilayer films. Although the x = 2 trilayer showed gradual and multistep IMT, the other trilayer films (x = 4, 9, and 65) showed clear clockwise IMT behavior. Correspondingly, several cracks were observed in the topographic AFM image of the x = 2 trilayer (**Figure 3-3(b)**). On the contrary, no crack was observed in the topographic AFM images of the x = 4, 9, and 65 trilayer films (**Figure 3-3(c)**, **(d)** and **(e)**). Thus, TiO_2 SCL suppresses the crack formation when it becomes thick and therefore, the $VO_2/TiO_2/VO_2$ trilayer shows clear clockwise IMT behavior. Since the x = 4 trilayer film showed slightly broader clockwise IMT behavior, it was concluded that use of ~9-nm-tihck TiO_2 SCL is useful for the strain compensation and crack suppression for VO_2 films.

Second, the effectiveness of TiO_2 SCL on maintaining clear clockwise IMT behavior was verified, even when the overall VO_2 thickness is ~50 nm, far thicker than the t_c. The VO_2 (~8 nm)/TiO_2 (~9 nm) multilayered (ML) films were fabricated on (001) TiO_2 substrates with varying the lamination number. **Figure 3-4** summarizes the $\rho-T$ curves of the ML films. Overall, the T_c gradually increased with the number of lamination increases. As already mentioned above, the 8-nm-thick VO_2 single layer (**Figure 3-4(a)**) and the trilayer (**Figure 3-4(b)**) showed clear clockwise IMT behavior. When the lamination number increased, two-step IMT behavior was observed in the heating direction; For three times laminated ML (**Figure 3-4(c)**), the first IMT (low temperature

side, IMT_L) occurred at 285 K and the second IMT (high temperature side, IMT_H) occurred at 307 K. When the lamination number increased, the IMT_L gradually increased with the lamination number increased, whereas the IMT_H did not change. On the other hand, the increase behavior of ρ became broader in the cooling direction with the lamination number increases. These phenomena are different from the crack-induced multistep IMT revealed in the previous section (**Figure 3-2(a)** and **3-3(a)**).

Indeed, in addition to the crack-induced multistep IMT, there are several reports of multiphase related such behavior [1, 18, 19]. For multilayer films in this study, the top VO_2 layer and middle VO_2 layer may exhibit different Tc owning to the delay of heat transfer or even the difference state themselves. The former was excluded by the consistency of the IMT curves under different cooling/heating rate (**Figure 3-5**). For the latter, a TiO_2 (9 nm)/VO_2 (8 nm) bilayer film was fabricated on (001) TiO_2 substrate and measured the $\rho-T$ curve (**Figure 3-6(a)**). It is obvious that the IMT behavior of bilayer film is different from single layer VO_2 (8 nm) and the x = 65 trilayer film (**Figure 3-6(b)**), indicating the possibility of multiphase-induced multistep IMT. Furthermore, considering that the top VO_2 layer and middle VO_2 layer can be simplified as a parallel circuit, the $\rho-T$ curve of the five times laminated ML can be simulated (**Figure 3-6(c)**), based on the $\rho-T$ curve of TiO_2/VO_2 bilayer film and the x = 65 trilayer film, due to the clear multistep IMT and similar overall thickness (Thickness of the five times laminated ML is ~76 nm while that of the x = 65 trilayer film is ~81 nm). The simulated multistep

IMT is similar to the observed $\rho-T$ curve (**Figure 3-6(d)**), emphasizing that the multistep IMT in these ML films originates from the different state between top VO_2 layer and middle VO_2 layer.

The T_c of the resultant ML films as a function of the overall VO_2 thickness was summarized as shown in **Figure 3-7(a)**. Since the heating process shows two-step IMT, they were plotted separately. The T_c gradually increased with increasing thickness in both heating and cooling process. It should be noted that the three times laminated ML showed relatively low IMT_L in heating that is close to the T_c in cooling. Subsequently, IMT_L gradually increased and approached to IML_H as the thickness increases. Considering the ML films with increasing the number of laminations has more middle VO_2 layers, such shift is most likely due to a rise in the contribution of the middle VO_2 layer. Lastly, if comparing the T_c of the ML films and the single layer VO_2 films grown on (001) TiO_2 substrates (**Figure 3-7(b)**) [11, 17, 18], it is obvious that the ML films exhibit a more regular change trend as well as overall low T_c, compared to the single layer VO_2 films.

3.4. Conclusion

In this chapter, the effectiveness of TiO_2 SCL on suppression of crack formation and stabilization of IMT behavior of VO_2 films grown on TiO_2 substrate was investigated. The results clarified that the thickness induced crack formation in single layer VO_2 film

can be suppressed through middle insertion of TiO_2 SCL with thickness exceeding 9 nm. Consequently, sharp IMT behaviors with T_c around room temperature were still observed in such multilayer film although the overall VO_2 thickness exceed critical thickness. Additionally, the relation between IMT behavior and lamination number was also explored. Multistep IMT behaviors in heating process were observed for ML films with middle lamination number (3/2, 4/3, and 5/4), possibly attributed to the difference between top and middle VO_2 layer. Lastly, with increasing lamination number, the T_c can be regulated smoothly around room temperature, ranging from 292 to 302 K. This study provides an idea to solve the crack problem of VO_2 films grown on TiO_2 substrates and may facilitate the research on VO_2-based thermochromic application.

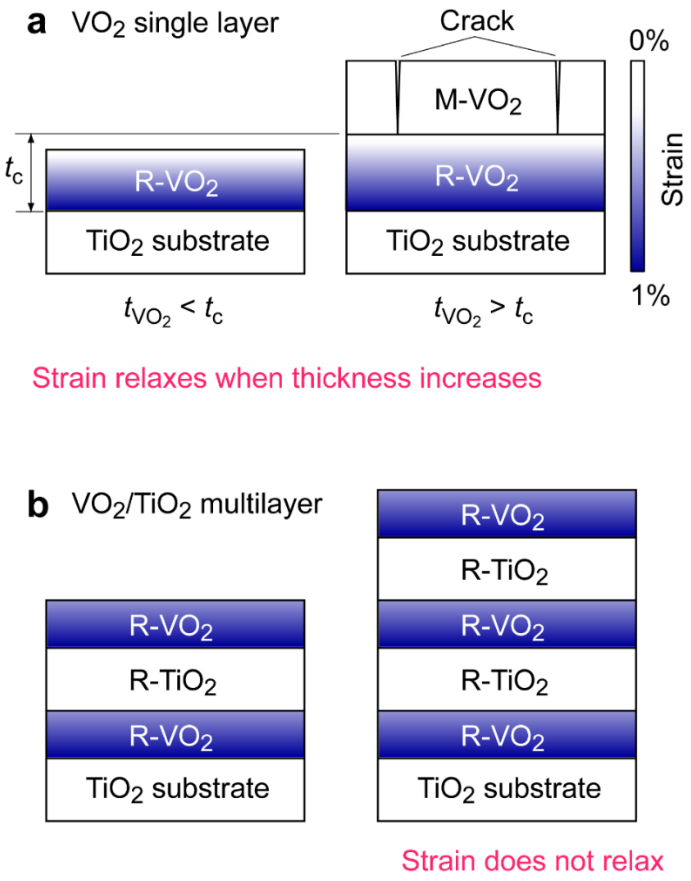

Figure 3-1. Hypothesis. (a) VO_2 single layer growth. When the VO_2 layer thickness exceeds the critical thickness ($t_c \approx 15$ nm), the VO_2 lattice is relaxed and the rutile (R) lattice becomes monoclinic (M) lattice. The lattice strain is released through crack formation. (b) The hypothesis of crack formation suppression of VO_2 film by fabricating epitaxial VO_2/TiO_2 multilayer. We expected that the TiO_2 strain compensation layer (SCL) maintains the strain condition of VO_2.

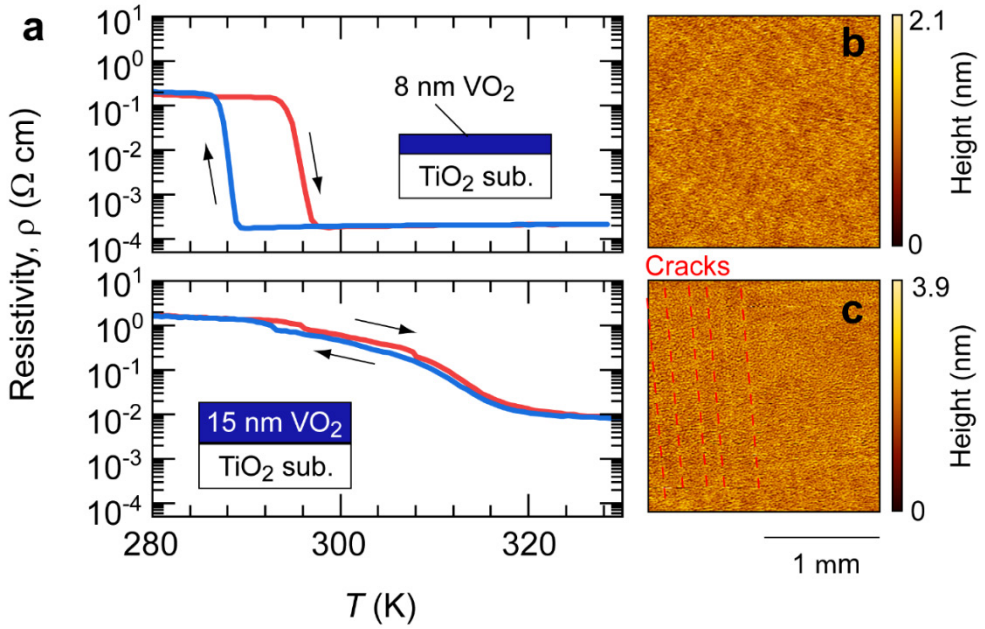

Figure 3-2. Insulator-to-metal transition behavior of VO_2 epitaxial films on (001) TiO_2 substrates. (a) Temperature dependence of the electrical resistivity for (upper) 8-nm-thick VO_2 epitaxial film and (lower) 15-nm-thick VO_2 epitaxial film. Although clear IMT with clockwise hysteresis is clearly seen in 8-nm-thick VO_2, 15-nm-thick VO_2 does not show clear hysteresis. (b, c) Topographic AFM images of (b) the 8-nm-thick VO_2 and (c) the 15-nm-thick VO_2 epitaxial films. Many cracks are seen in (c) and marked as the dashed line.

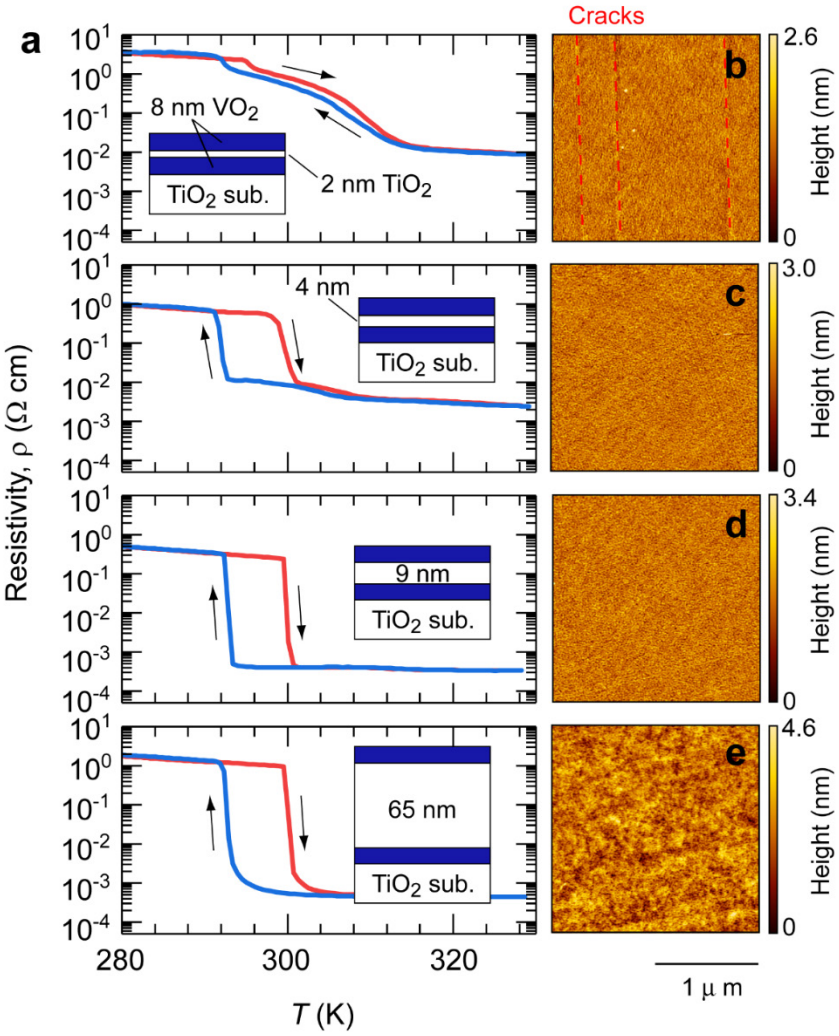

Figure 3-3. Change in the IMT behavior of 16-nm-thick VO_2 films with insertion of TiO_2 overlayer. (a) $\rho-T$ curves. Although 2-nm-thick TiO_2 overlayer insertion does not affect the IMT behavior, clear recovery of the IMT behavior is seen when the TiO_2 SCL thickness exceeds 4 nm. (b–e) Topographic AFM images of the TiO_2 SCL inserted $VO_2/TiO_2/VO_2$ films with varied TiO_2 SCL thickness. (b) 2 nm, (c) 4 nm, (d) 9 nm, and (e) 65 nm. Cracks are seen in (b) and marked as the dashed line.

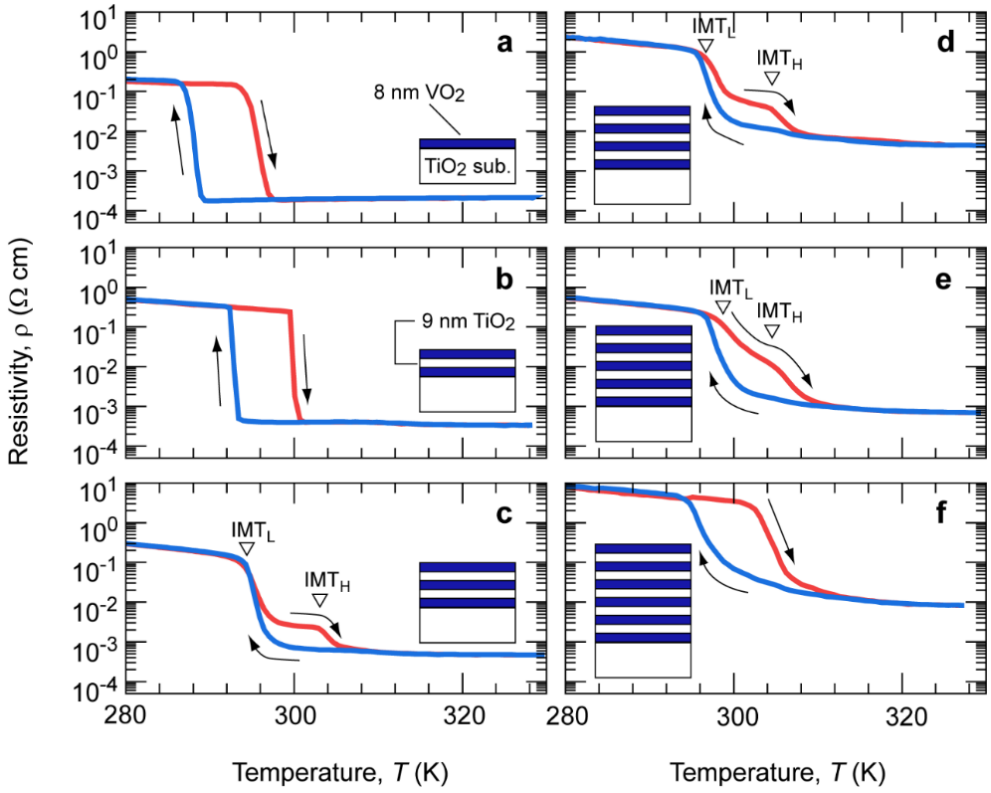

Figure 3-4. Change in the IMT behavior of the 8-nm-thick VO_2/9-nm-thick TiO_2 multilayered (ML) films. (a) VO_2 single layer, (b) trilayer film, (c) three times laminated film, (d) four times laminated film, (e) five times laminated film, (f) six times laminated film.

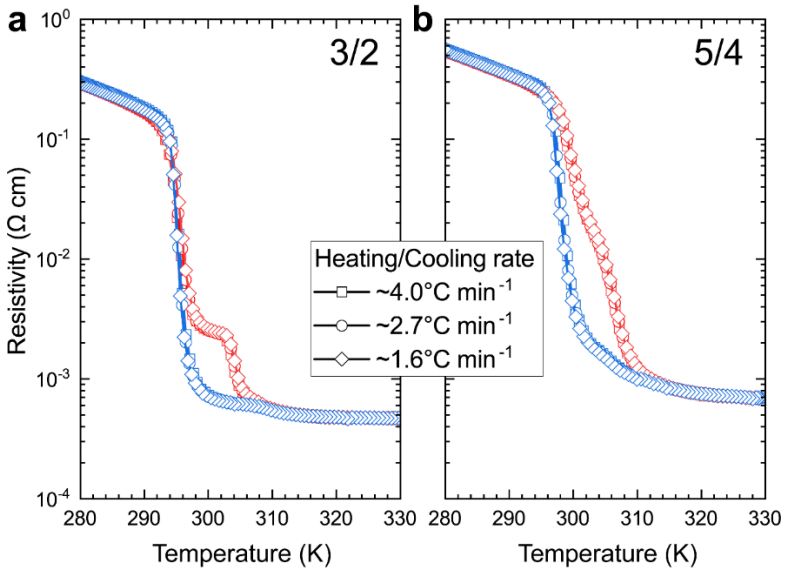

Figure 3-5. $\rho-T$ curves measured with different heating/cooling rate. (a) three times laminated film. (b) five times laminated film.

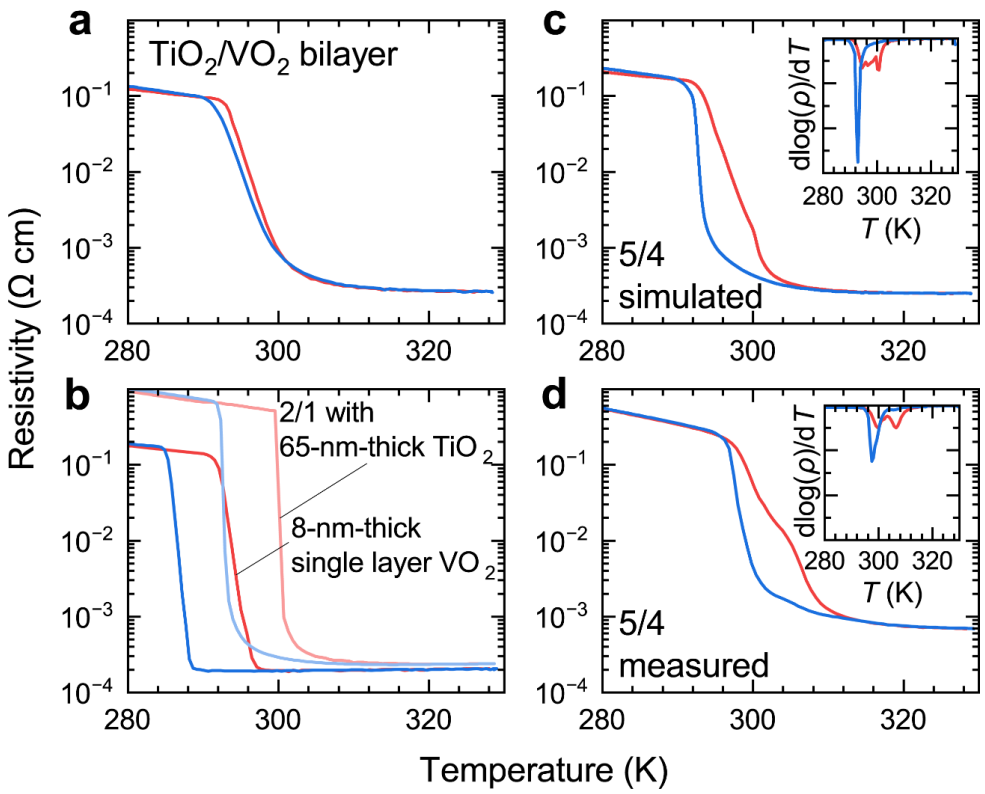

Figure 3-6. Clarification of multistep IMT behavior. $\rho-T$ curves of (a) TiO_2/VO_2 bilayer film, (b) 8-nm-thick single layer VO_2 film, and trilayer film with 65-nm-thick TiO_2 layer. (c) The simulated $\rho-T$ curve of five times laminated film based on the parallel circuit model by combining the $\rho-T$ curve of TiO_2/VO_2 bilayer and trilayer film with 65-nm-thick TiO_2 layer. (d) The measured $\rho-T$ curve of five times laminated film for comparison. The insets are the corresponding differential curves ($d\log(\rho)/dT$).

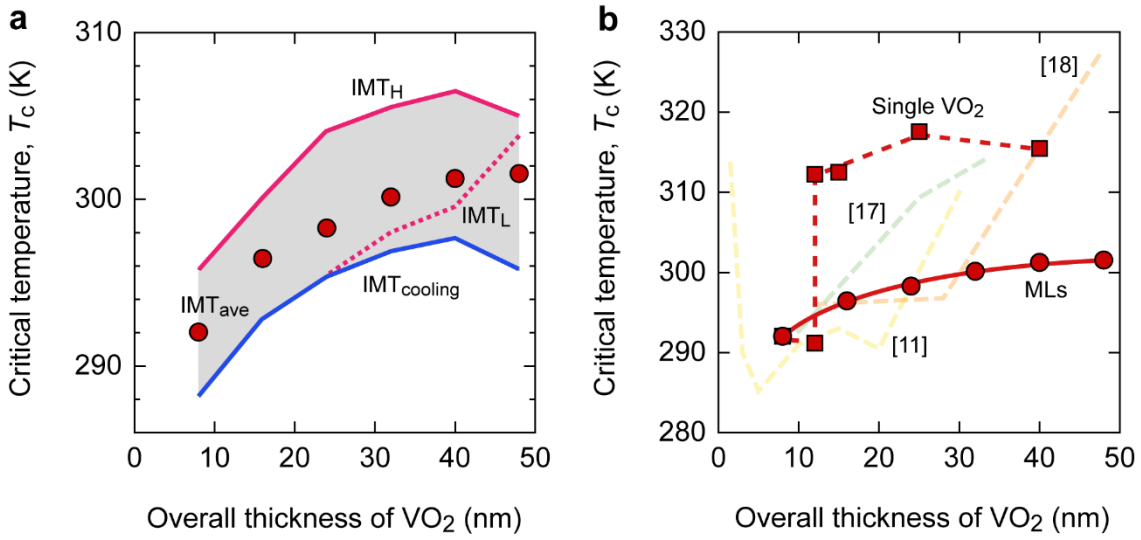

Figure 3-7. The critical temperature (T_c) of ML films. (a) The T_c of ML films as the function of the overall thickness of VO_2 layer. IMT_H denotes T_c of higher temperature in heating process. IMT_L denotes T_c of lower temperature in heating process. $IMT_{cooling}$ denotes T_c in cooling process. IMT_{ave} denotes average T_c. (b) Comparison of the avenge T_c.

References

[1] Muraoka, Y. and Z. Hiroi, Metal–Insulator Transition of VO_2 Thin Films Grown on TiO_2 (001) and (110) Substrates. *Appl. Phys. Lett.* **80**, 583-585 (2002).

[2] Breckenfeld, E.*, et al.*, Strain Effects in Epitaxial VO_2 Thin Films on Columnar Buffer-Layer TiO_2/Al_2O_3 Virtual Substrates. *ACS Appl. Mater. Inter.* **9**, 1577-1584 (2017).

[3] Bayati, M.R.*, et al.*, Correlation between Structure and Semiconductor-to-Metal Transition Characteristics of VO_2/TiO_2/Sapphire Thin Film Heterostructures. *Acta. Mater.* **61**, 7805-7815 (2013).

[4] Chen, B.*, et al.*, Room Temperature Insulator-to-Metal Transition of VO_2/TiO_2 Epitaxial Bilayer Films Grown on M-plane Sapphire Substrates. *Adv. Electron. Mater.* **8**, 2100687 (2022).

[5] Nagashima, K.*, et al.*, Stress Relaxation Effect on Transport Properties of Strained Vanadium Dioxide Epitaxial Thin Films. *Phys. Rev. B* **74**, 172106 (2006).

[6] Rodriguez, L.*, et al.*, Self-Pixelation Through Fracture in VO_2 Thin Films. *ACS Appl. Electron. Mater.* **2**, 1433-1439 (2020).

[7] Sohn, A.*, et al.*, Visualization of Local Phase Transition Behaviors near Dislocations in Epitaxial VO_2/TiO_2 thin films. *Appl. Phys. Lett.* **107**, 171603 (2015).

[8] Yajima, T.*, et al.*, Drastic Change in Electronic Domain Structures via Strong Elastic Coupling in VO_2 Films. *Phys. Rev. B* **91**, 205102 (2015).

[9] Sandiumenge, F.*, et al.*, Metallic Diluted Dimerization in VO_2 Tweeds. *Adv. Mater.* **33**, 2004374 (2021).

[10] Kawatani, K., T. Kanki, and H. Tanaka, Formation Mechanism of a Microscale Domain and Effect on Transport Properties in Strained VO_2 Thin Films on TiO_2(001). *Phys. Rev. B* **90**, 054203 (2014).

[11] Paik, H.*, et al.*, Transport Properties of Ultra-Thin VO_2 Films on (001) TiO_2 Grown by Reactive Molecular-Beam Epitaxy. *Appl. Phys. Lett.* **107**, 163101 (2015).

[12] Lee, D.*, et al.*, Sharpened VO_2 Phase Transition via Controlled Release of Epitaxial Strain. *Nano Lett.* **17**, 5614-5619 (2017).

[13] Chen, X.*, et al.*, A Near-Field Study of VO_2/(100)TiO_2 Film and its Crack-Induced Strain Relief. *Appl. Phys. Lett.* **121**, 021902 (2022).

[14] Tatebayashi, J.*, et al.*, Strain Compensation Technique in Self-Assembled InAs/GaAs Quantum Dots for Applications to Photonic Devices. *Journal of Physics D-Applied Physics* **42**, 073002 (2009).

[15] Kageyama, T.*, et al.*, InAs/GaAs Quantum Dot Lasers with GaP Strain-Compensation Layers Grown by Molecular Beam Epitaxy. *Phys. Status Solidi A* **213**, 958-964 (2016).

[16] Kim, Y.*, et al.*, Efficiency Enhancement in InAs/GaAsSb Quantum Dot Solar Cells with GaP Strain Compensation Layer. *Appl. Phys. Lett.* **108**, 103104 (2016).

[17] Yang, Y.*, et al.*, Thickness Effects on the Epitaxial Strain States and Phase Transformations in (001)-VO_2/TiO_2 Thin Films. *J. Appl. Phys.* **125**, 082508 (2019).

[18] Sharma, Y.*, et al.*, Competing Phases in Epitaxial Vanadium Dioxide at Nanoscale. *APL Mater.* **7**, 081127 (2019).

[19] Eres, G.*, et al.*, Versatile Tunability of the Metal Insulator Transition in $(TiO_2)_m/(VO_2)_m$ Superlattices. *Adv. Funct. Mater.* **30**, 2004914 (2020).

Chapter 4. Orthorhombic Distortion-induced Anatase-like Optoelectronic Properties of Rutile TiO_2

4.1. Objective of this chapter

In chapter 2, a strain induced orthorhombic distortion was observed in VO_2/TiO_2 films grown on $(1\bar{1}00)$ α-Al_2O_3 substrates and the effects of such distortion on IMT behavior of VO_2 was investigated. In fact, TiO_2 itself is a traditional rutile structured material, which is expected to introduce such distortions to modulate its physical properties. In this chapter, a systematic study was conducted on it.

Titanium dioxide (TiO_2) is an active material for photocatalytic water splitting. The optical bandgap (E_g) of TiO_2 is 3.1 − 3.3 eV, which is close to the maximum energy of visible light (~3.1 eV) [1-3]. Fundamentally, E_g of TiO_2 is composed of the Ti 3d-based conduction band minimum (CBM) and the O 2p-based valence band maximum (VBM). When TiO_2 absorbs light (photon energy $>E_g$), the valence electron is excited to the conduction band, generating a positive hole in the valence band. The conduction electron reduces water while the hole oxidizes it [4-7]. In addition, the photocatalytic activity strongly depends on the crystal structure of TiO_2 because the electronic structure is affected by the crystal structure [8-12]. Thus, understanding the correlation between the electronic and crystal structures is essential to extract the functional

properties of TiO_2.

In this chapter, a series of 0.5%Nb:TiO_2 films with various thickness were fabricated on $(1\bar{1}00)$ α-Al_2O_3 substrates. Subsequently, their crystallographic information and optoelectronic properties were investigated. The results suggest that the orthorhombic lattice distortion was successfully introduced into TiO_2 films and degree of such distortion was controlled by the film thickness. Correspondingly, with increasing orthorhombic lattice distortion, rutile 0.5%Nb:TiO_2 epitaxial films exhibit anatase-like optoelectronic properties. The present observations provide insight into regulating the physical properties of TiO_2 and should be beneficial for designing TiO_2-based photocatalysts and transparent conducting electrodes.

4.2. Experimental

***Sample preparation*:** The target was a 0.5%-Nb-doped TiO_2 ceramic disk. Pulsed laser deposition (PLD) with a KrF excimer laser (λ = 248 nm, laser fluence ~1.0 J cm^{-2} $pulse^{-1}$, repetition rate = 10 Hz) was used to fabricate 0.5%-Nb-doped TiO_2 films on $(1\bar{1}00)$ α-Al_2O_3 single crystal substrates, where the slight doping is to provide the donor dopant to facilitate further electronic measurements. Such low-level doping does not affect the lattice structure significantly [13, 14]. During film growth, the substrate temperature and oxygen pressure were kept constant at 500 °C and 5 × 10^{-3} Pa,

respectively. Adjusting the deposition time controlled the film thickness.

***Crystallographic analyses*:** The film thickness, crystallographic orientations, and lattice parameters were determined using high-resolution X-ray diffraction (XRD, ATX-G, Rigaku) with Cu $K\alpha_1$ (λ = 0.154059 nm) radiation. Both out-of-plane and in-plane measurements were performed to extract the lattice parameters. The atomic arrangement of the resultant films was visualized using STEM (ARM200CF, JEOL Co. Ltd) operated at 200 keV. HAADF-STEM images were taken with the detection angle of 68 − 280 mrad. All measurements were conducted at room temperature.

***Electrical and optical properties measurements*:** The electrical resistivity (ρ), carrier concentration (n), and Hall mobility (μ_{Hall}) at room temperature were measured by the dc four-probe method with the van der Pauw electrode configuration in air. The temperature-dependent electrical resistivity ($\rho-T$), carrier concentration ($n-T$), and Hall mobility ($\mu_{Hall}-T$) were performed using the same configuration in a vacuum and a variable temperature of 10−300 K. The thermopower (S) of the films in the in-plane direction was measured by the conventional steady-state method. The transmission and reflection spectra in the 200 − 1600 nm wavelength range were measured by a spectrophotometer (SolidSpec-3700, Shimadzu).

***X-ray Absorption Spectroscopy (XAS) measurements*:** XAS measurements were

performed at the 2A beamline of the Pohang Accelerator Laboratory (PAL) with the grazing incidence (22.5°) configuration in the total-electron-yield (TEY) mode. The Ti L-edge spectra were measured at room temperature.

***Density Functional Theory (DFT) calculations*:** DFT calculations were performed with the projector augmented wave method implemented in the Vienna Ab initio Simulation Package (VASP) program [15, 16]. For the exchange-correlation term of the electrons, the generalized gradient approximation (GGA) parameterized by Perdew, Burke, and Ernzerhof was used [17]. The electrons were $3p^6$, $3d^2$, and $4s^2$ for Ti and $2s^2$ and $2p^4$ for O. To describe the localized features of the Ti-3d orbitals, the GGA+U method was employed, where the onsite Coulomb repulsion was considered with an effective parameter of U = 7.0 eV for Ti 3d [18, 19]. X. Han et al. suggested the optimum choice of the U parameter for TiO_2 [19]. The electronic wavefunctions were expanded by plane waves up to a cutoff energy of 500 eV. Brillouin zone integration was performed with the Monkhorst-Pack mesh of 4×4×6 for the unit cell of rutile TiO_2. The structure was optimized until the atomic forces converged to less than 0.01 eV/Å. The calculated lattice parameters of a = 0.469 nm and c = 0.305 nm slightly overestimated the experimental data [20], but the trends were similar to those in previous GGA calculations [19].

The present GGA+U calculations indicated that rutile TiO_2 had a direct theoretical E_g

of 2.30 eV at the Γ point. To evaluate effective masses (m^*) of electrons in rutile TiO_2, the energy dispersion curves at the CBM were obtained around the Γ point for the rutile TiO_2 unit cell (structure-optimized as above) using a k-point mesh density toward a particular symmetric point of more than 4.2 nm. Subsequently, parabolic curve fitting for five *k*-points centered at Γ was performed, and the m^* values of electrons were obtained from the second partial derivatives of the parabolic fitting curves [21].

Although the theoretical E_g (2.30 eV) of bulk rutile TiO_2 underestimated the experimental value (3.03 eV) [22], which is a standard feature of GGA-related DFT calculations, such a small theoretical E_g may also affect the theoretical m^*. To evaluate the effect of the theoretical E_g on m^*, hybrid-functional calculations only at the Γ point were also performed using the hybrid density functional proposed by Heyed, Scuseria and Ernzerhof (HSE06) [23, 24]. The E_g of 3.20 eV calculated by HSE06 reproduced the experimental E_g value better than that by the GGA+U calculations. However, the calculated m^* of 1.168 for Γ to X and 0.414 for Γ to M were slightly smaller than the corresponding GGA+U values of 1.672 and 0.588, respectively (**Table 4-1**). However, these differences do not affect the conclusion of this paper. Since hybrid functional calculations are computationally demanding, the GGA+U calculations were mainly used to investigate m^* in distorted rutile TiO_2.

4.3. Result and discussion

4.3.1. Epitaxial film growth of rutile Nb:TiO_2 with orthorhombic distortion

Figure 4-1 depicts the lattices of (001) rutile TiO_2 and $(1\bar{1}00)$ α-Al_2O_3 crystals. The epitaxial relationship is (001) [100] TiO_2 || $(1\,\bar{1}\,00)$ [0001] α-Al_2O_3. Due to the anisotropic lattice parameter of $(1\bar{1}00)$ α-Al_2O_3 in the in-plane directions, the rutile TiO_2 lattice sustains compressive strain along [100] (lattice mismatch: −5.9%), whereas tensile strain occurs along [010] (lattice mismatch: +3.5%). **Figure 4-2** summarizes the crystallographic characterization of the resultant Nb:TiO_2 films on $(1\,\bar{1}\,00)$ α-Al_2O_3 substrates. The out-of-plane XRD patterns exhibit intense 002 diffraction peaks of rutile Nb:TiO_2 and those of $3\bar{3}00$ α-Al_2O_3 substrate (**Figure 4-2(a)**), indicating a high *c*-axis orientation. As the thickness increases, the 002 peak shifts toward the smaller scattering vector and approaches the bulk position (dashed line), which suggests an increasing trend of the lattice parameter *c* (**Figure 4-2(c)**). The in-plane XRD patterns (**Figure 4-2(b)**) have different peak positions for the 400 (upper) and the 040 (lower). The 400 diffraction peaks of Nb:TiO_2 are seen together with those of 000$\underline{12}$ α-Al_2O_3 substrates at $\sim q_x/2\pi$ = 8.75 nm^{-1}. This is slightly larger than that of bulk (dashed line), but the 400 peaks are independent of thickness. In contrast, the 040 diffraction peaks of Nb:TiO_2, which are seen together with $22\bar{4}0$ α-Al_2O_3 substrates, shift toward a larger scattering vector as the thickness increases and approach $\sim q_y/2\pi$ = 8.67 nm^{-1}. This value is slightly smaller than that of the bulk (dashed line).

Figure 4-2(d) summarizes the in-plane lattice parameters *a* and *b* as functions of the film thickness. Note that the lattice parameters of the 10-nm-thick and 20-nm-thick samples were extracted from the 200 Nb:TiO_2 and 020 Nb:TiO_2 diffraction peaks due to the weak peak intensities of 400 Nb:TiO_2 and 040 Nb:TiO_2. Lattice parameter *a* is ~0.457 nm, which is slightly shorter than that of the bulk (0.4594 nm) due to the compressive strain originating from the lattice mismatch (−5.9%). Lattice parameter *a* is independent of the thickness. Unlike lattice parameter *a*, lattice parameter *b* shows a clear thickness dependence. For a 10-nm-thick film, lattice parameter *b* is 0.473 nm, which is ~3% longer than that of bulk rutile TiO_2. However, it decreases to 0.461 nm, which is slightly longer than that of the bulk when the thickness is 300 nm. This clearly indicates the presence of a strong tensile strain originating from the lattice mismatch (+3.5%).

To visualize the orthorhombic lattice distortion, the ratio of lattice parameters (*b*/*a*) was defined as the degree of orthorhombic distortion (**Figure 4-2(e)**). The ratio *b*/*a* gradually decreases as the Nb:TiO_2 thickness increases and ranges from ~1.035 to ~1.01. It should be noted that the Nb:TiO_2 films were grown incoherently on $(1\bar{1}00)$ α-Al_2O_3 substrates. These results confirm orthorhombic strain is successfully introduced to the rutile TiO_2 and that the strain becomes smaller as the thickness increases. Also noting that the change tendency of lattice parameter *b* slowed down when the films are thicker than 100 nm, indicating such tensile strain has been highly weakened under this

condition.

To further clarify the orthorhombic distortion, cross-sectional STEM images were acquired for 6-nm-thick and 200-nm-thick TiO_2 films prepared under the same growth conditions. **Figure 4-3** shows the high-resolution HAADF-STEM images along the $[0001]Al_2O_3$ zone axis and the corresponding inverse fast Fourier transformation (IFFT) images. HAADF-STEM images (**Figure 4-3(a)** and **(b)**) exhibit a clear Z-contrast for the Ti and Al atoms. Consequently, the interface of TiO_2/M-plane sapphire can be observed, as shown by the dashed line.

Comparing the observed and theoretical structures of TiO_2 demonstrates that both the 6-nm-thick and 200-nm-thick films show (001) oriented rutile structures, which is consistent with our XRD results. IFFT is an intuitive method for observing dislocations. The lack of dislocations in IFFT of the 6-nm-thick film indicates that the TiO_2 lattice is strained (**Figure 4-3(c)**). In contrast, the edge dislocations at the interface of the 200-nm-thick film (**Figure 4-3(d)**) suggests that the strain is released by forming dislocations. The uneven distribution of dislocations may be due to no post-annealing. Based on the dislocation observations, the orthorhombic distortion originates from the elastic deformation of the lattice and was relieved through dislocation formation. In addition, it was also observed the HAADF-STEM images along $[11\bar{2}0]Al_2O_3$ zone axis of these two films (**Figure 4-4**). The existence of edge dislocations in both films along

this direction is also well consistent with the smaller change tendency of lattice parameter *a* (**Figure 4-2(d)**). For the 200-nm-thick films, it was observed the lattice parameter difference along the out-of-plane. No clear atom spacing difference was observed, indicating the strain release only occurs around the dislocation at interface instead of a gradient release from interface to surface. Such phenomenon has been experimentally revealed by other reports and it also confirms the uniformity of the film [25, 26].

4.3.2. Electrical and optical properties of the rutile Nb:TiO_2 films

The electron transport properties of the resultant Nb:TiO_2 films were measured at room temperature. **Figure 4-5** summarizes the electron transport properties as a function of the orthorhombic distortion (i.e., *b*/*a*). The electrical conductivity (σ) is 2 − 3 S cm^{-1} and is independent of *b*/*a* (**Figure 4-5(a)**). Similar to the Nb concentration (0.5% ≈ 1.6 × 10^{20} cm^{-3}), the carrier concentration (*n*) is in the range of 10^{19} − 10^{20} cm^{-3} and shows a gradual decreasing tendency as *b*/*a* increases (**Figure 4-5(b)**). For a semiconductor film depositing on sapphire, the band bending possibly occurs around the interface. Thus, the carriers within a contain thickness would be trapped, resulting in the decreasing of *n* when thickness decreased. In contrast, μ_{Hall} shows the opposite trend (**Figure 4-5(c)**). For a small *b*/*a* ratio (~1.01), the μ_{Hall} value is ~0.3 cm^2 V^{-1} s^{-1}. μ_{Hall} increases with *b*/*a* and exceeds 1 cm^2 V^{-1} s^{-1} when *b*/*a* = 1.034. The variety of μ_{Hall}

should be related to the change of effective mass, which would be revealed later.

It should be noted that the thermopower ($-S$) gradually decreases with b/a from ~600 to ~430 μV K^{-1} (**Figure 4-5(d)**). According to Mott's formula, $-S$ reflects n for semiconductors; $-S$ decreases as n increases if the Fermi energy increases on the parabolic electronic density of states (DOS) and m^* is constant. Thus, the observed tendencies of $-S$ and n reveal that the m^* becomes lighter when orthorhombic lattice distortion is introduced.

For visualization, m^* is estimated from the relation between n and S as [27]

$$S = -\frac{k_B}{e}\left(\frac{(r+2)F_{r+1}(\xi)}{(r+1)F_r(\xi)} - \xi\right),$$

$$n = 4\pi\left(\frac{2m^* k_B T}{h^2}\right)^{3/2} F_{1/2}(\xi),$$

where k_B, r, F_r, ξ, T, and h are the Boltzmann constant, scattering parameter of the relaxation time, Fermi integral, chemical potential, absolute temperature, and Plank's constant, respectively. F_r can be further expressed as

$$F_r(\xi) = \int_0^\infty \frac{x^r}{1 + e^{x-\xi}}\, dx.$$

Figure 4-5(e) plots the estimated m^* as a function of b/a. m^* of the almost relaxed rutile TiO_2 film (b/a ~1.008) is ~35 m_0. This value is consistent with the reported m^* of bulk rutile TiO_2 (12 − 35 m_0 [28-31]). It should be noted that the m^* decreases as b/a

increases and reaches ~3 m_0 when b/a = 1.034. This smaller m^* is closer to that of anatase TiO_2 (~1 m_0) [32, 33]. So far, the results demonstrated the relation between distortion and effective mass. The decreasing tendency is corresponding to the increase of mobility, revealing the major factor in change of mobility.

In addition to the electron transport properties, E_g is also a property associated with the electronic structure. There is a consensus that E_g of bulk rutile TiO_2 is ~3.06 eV while that of anatase is ~3.20 eV [1, 34, 35]. To clarify the effect of the orthorhombic distortion on E_g, the optical transmission and reflection spectra of the resultant films were measured for resultant films. It should be noted that, although rutile TiO_2 is a direct bandgap semiconductor, the direct transition is dipole-forbidden and degenerated with the indirect allowed transition [36-38]. Thus, direct E_g is equivalent to indirect E_g and was possible to be evaluated by extrapolating the linear region of the Tauc $((\alpha hv)^{1/2} - hv)$ plot (**Figure 4-6**). E_g gradually increases from ~3.11 eV to ~3.48 eV as b/a increases (**Figure 4-7(a)**). Even a highly relaxed film (300 nm) shows a small distortion (b/a ~1.008), which may explain why E_g is slightly higher than the rutile bulk value (~3.06 eV) [39].

Generally, E_g of an extremely thin layer is greater than that of the bulk due to the quantum size effect (QSE). QSE occurs when the film thickness is thinner than the de Broglie wavelength. E_g gradually increases as the film thickness decreases (**Figure 4-**

7(b)). To clarify the origin of the increased E_g, the theoretical E_g was calculated assuming that QSE can be expressed as [40, 41]

$$E_g = E_{g,Bulk} + \frac{h^2}{8d^2}\left(\frac{1}{m_e^*} + \frac{1}{m_h^*}\right),$$

where $E_{g,Bulk}$, h, and d are the bulk bandgap, Planck's constant, and film thickness, respectively. m_e^* and m_h^* are the electron and hole effective masses, which are assumed to be ~20 m_0 [29] and ~5 m_0 [42], respectively. The calculated E_g increases dramatically when the film thickness is thinner than ~10 nm. This behavior does not fit with the observed E_g, indicating that the QSE theory cannot explain the observed E_g. These observations confirm that the electronic structure of a rutile TiO_2 film is predominantly modulated via orthorhombic distortion.

Nb:TiO_2 films grown on $(1\bar{1}00)$ α-Al_2O_3 substrate show differentiated properties from the rutile phase when the thickness is sufficiently thin due to orthorhombic lattice distortion but typical properties of the rutile phase appear as the thickness increases. Since rutile Nb:TiO_2 shows interesting transport properties at low temperatures and the temperature-related behavior may provide information about the transport mechanism, the temperature dependence of the electron transport properties was measured for the 300-nm-thick Nb:TiO_2 film (b/a ~1.008) and the 20-nm-thick Nb:TiO_2 film (b/a = 1.034). Both films show semiconductor-like behaviors of ρ (**Figure 4-8(a)**). As the temperature decreases, ρ gradually increases, n gradually decreases (**Figure 4-8(b)**), and μ_{Hall} increases (**Figure 4-8(c)**). These results suggest that phonons dominate carrier

scattering.

The films display different temperature dependences of $-S$ (**Figure 4-8(d)**). At room temperature, the $-S$ values of the 300-nm-film and the 20-nm-film are ~0.6 mV K^{-1} and 0.45 mV K^{-1}, respectively. As the temperature decreases, the former increases dramatically and exceeds 1.5 mV K^{-1}. In contrast, the latter decreases gradually and approaches zero. It has been observed that rutile TiO_2 shows a colossal $-S$ at low temperature due to the phonon drag effect [28, 43]. This behavior is usually observed in materials with a large m^* [44-47]. As above described, m^* of the 300-nm-film is 35 m_0 while that of the 20-nm-film is ~3 m_0. Similarly, the presence or absence of a colossal $-S$ reflects the distortion-induced m^* modulation at room temperature.

These observations reveal that introducing orthorhombic lattice distortion using $(1\bar{1}00)$ α-Al_2O_3 substrates significantly modulates the electronic structure of rutile TiO_2. Orthorhombic distortion realizes changes in E_g, m^*, and $-S$, indicating that the electronic structure of rutile TiO_2 shifts toward that of anatase TiO_2.

4.3.3. Changes in the electronic structure of rutile TiO_2 due to orthorhombic distortion

The XAS spectra of the TiO_2 films were measured to directly clarify the change in the

electronic structure of rutile TiO_2 upon orthorhombic distortion. **Figure 4-9** shows the XAS spectra of the 10 − 200-nm-thick rutile TiO_2 films at the Ti L_3-edge. The single peak around ~456 eV corresponds to the three-fold degenerate t_{2g} state, and the double peak around ~459 eV corresponds to the two-fold degenerate e_g state. The e_g peak is further split into two peaks (e_{g1} and e_{g2}) due to the octahedral distortion of TiO_6 octahedra. The octahedral distortion differs between rutile and anatase. Rutile is D_{2h} symmetry, while anatase is D_{2d}. This difference is reflected in the XAS spectra as the inversion of the relative intensities of the e_{g1} and e_{g2} peaks. Hence, their intensities can be used as a fingerprint for different TiO_2 polymorphs [48]. The observed XAS spectra indicate the TiO_2 films maintain the electronic structure of the rutile phase. Although the anatase phase does not appear even with a large orthorhombic distortion, it has been considered that changes in the lattice parameters result in changes in the degree of octahedral distortion. This small perturbation has a non-negligible effect on the physical properties [9, 49, 50]. From this viewpoint, fitting of the XAS data with a Gaussian distribution was performed (The fitting parameters were available in **Table 4-3**) and the relative peak area ratio of e_{g2}/e_{g1} was calculated (**Figure. 4-9(a−d)**). As the thickness increases, e_{g2}/e_{g1} shows an increasing tendency (**Figure. 4-9(e), inset**). However, e_{g2}/e_{g1} linearly decreases as *b*/*a* increases (**Figure. 4-9(e)**), clearly indicating that there is a strong correlation between the electronic structure of rutile TiO_2 and the orthorhombic lattice distortion.

4.3.4. DFT calculation of TiO_2 with orthorhombic lattice distortion

Finally, DFT calculations of rutile TiO_2 with orthorhombic lattice distortion were performed to investigate the influence of lattice distortion of TiO_2 thin films on electron m^*. Three TiO_2 unit cells were considered: 1) a rutile unit cell with fully optimized a- and c-axis lengths (a_0, $b_0 = a_0$, c_0), 2) a rutile unit cell with the b-axis length extended 3% from the fully optimized value (a_0, $1.030b_0$, c_0), and 3) a rutile unit cell with the a-axis length compressed 0.5% and the b-axis length extended 3% ($0.995a_0$, $1.03b_0$, $0.994c_0$). These extensions and compressions of a_0 and b_0 are based on the experimental data shown in **Figure 4-2**. It should be noted that the c-axis length in case 3 was optimized by the DFT calculations, and the optimized c-axis length of $0.994c_0$ agrees well with that for the thin-film value (about $0.9925c_0$) shown in **Figure 4-2(c)**. Moreover, the theoretical E_g value for the distorted unit cell (case 3) is 2.37 eV, which is larger than the fully optimized unit cell value of 2.30 eV. The increased E_g trend for the distorted rutile unit cell agrees well with the experimental E_g variation against orthorhombic distortion shown in **Figure 4-7**.

Table 4-1 lists the calculated m^* values at the Γ point toward the X (or Y) point and the M (or S) point (these directions correspond to the in-plane ones to the thin-film surface). The DFT results show that the m^* of the fully optimized rutile TiO_2 are around 1.7 m_0 and 0.6 m_0, which are much smaller than the experimentally observed value (~35

m_0). Previous GGA calculations provided similar theoretical results [37, 51, 52]. It is thought that electronic conduction in rutile TiO_2 is not simply described by the m^*-like states but is strongly affected by the formation of polarons, namely, electron coupling with lattice vibrations (phonons). As the orthogonal distortions increase (cases 2 and 3), the calculated m^* values tend to increase. However, the m^* values are still smaller than the experimentally observed one (3 m_0) for the distorted thin films (**Figure 4-5e**). Hence, it is most likely that the original orthogonal distortions of the rutile TiO_2 thin films due to the substrate considerably change the lattice vibrational states in the thin films.

4.4. Conclusion

In this chapter, 0.5%Nb:TiO_2 epitaxial films with various thickness were fabricated on $(1\bar{1}00)$ α-Al_2O_3 substrates. Due to strain induced orthorhombic lattice distortions, the thinner films exhibit optoelectronic properties approaching to anatase phase. Concretely speaking, as the film thickness decreases, b/a increases up to 3.4%; as b/a increases, the carrier m^* decreases from 35 m_0 to 3 m_0 (m_0: electron mass) but E_g increases. The electronic structure change was observed experimentally. The present observations provide insight into regulating the physical properties of TiO_2 and should aid in the design of TiO_2-based photocatalysts and transparent conducting electrodes.

Table 4-1. Calculated effective masses for electrons in non-distorted (case 1) or orthogonally distorted (cases 2 and 3) rutile TiO_2.

	Effective mass m^*/m_0			
	Γ→X	Γ→Y	Γ→M	Γ→S
Case 1 (a_0, b_0=a_0, c_0)	1.672		0.588	
Case 2 (a_0, b_0=1.030a_0, c_0)	1.777	1.698		0.656
Case 3 (0.995a_0, b_0=1.030a_0, 0.994c_0)	1.759	1.664		0.742

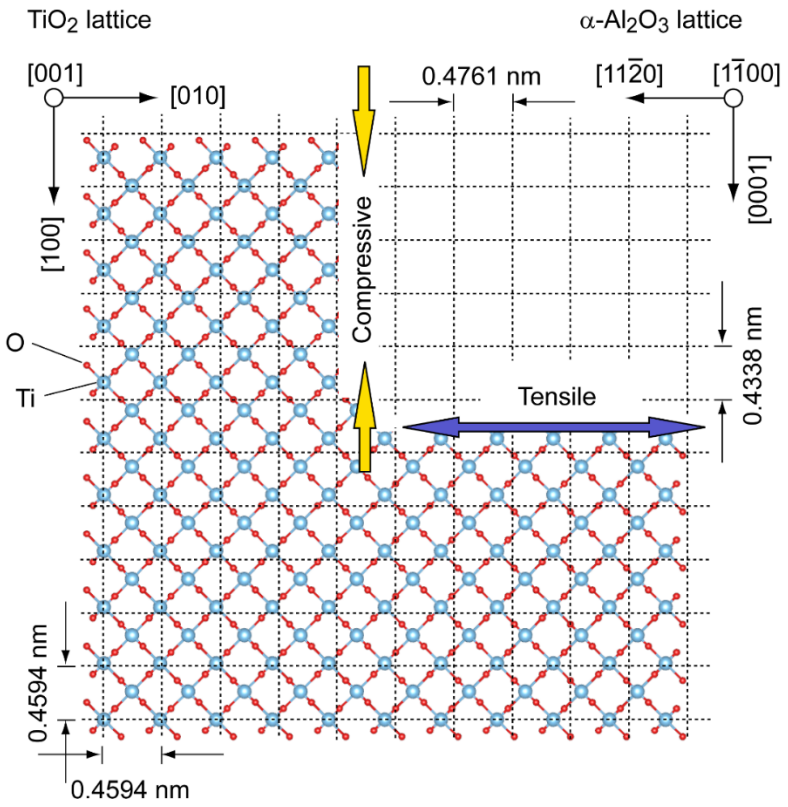

Figure 4-1. Hypothesis of the orthorhombic lattice distortion of rutile-structured TiO_2 epitaxial film on an M-plane sapphire substrate. Schematic of the crystal lattice of rutile TiO_2 on (1$\bar{1}$00) α-Al_2O_3 (sublattice of oxide ions, dotted lines). Since lattice parameter *a* of TiO_2 is longer than lattice parameter *c* of α-Al_2O_3 (lattice mismatch: −5.9%), compressive strain is assumed, whereas tensile strain is assumed because lattice parameter *a* of α-Al_2O_3 is larger than that of lattice parameter *b* of TiO_2 (lattice mismatch: +3.5%). Therefore, I hypothesized that orthorhombic distortion is introduced in the TiO_2 lattice. For convenience, the TiO_2 lattice is represented by the ball and stick model, while the α-Al_2O_3 lattice is simplified to the sublattice of oxide ions, which is shown by the dotted lines.

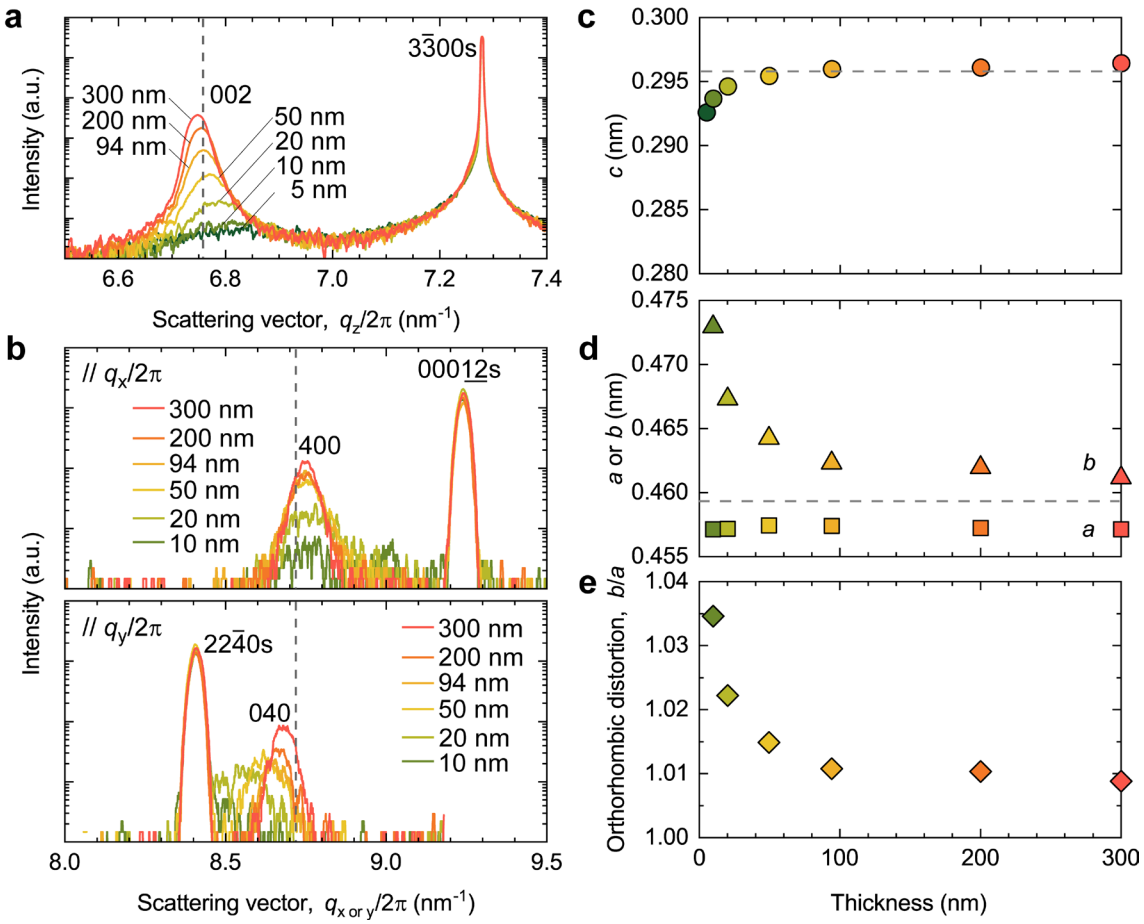

Figure 4-2. Crystallographic characterization of the resultant TiO_2 films on an M-plane sapphire substrate. (a) Out-of-plane and (b) in-plane XRD patterns of 5 − 300-nm-thick TiO_2 films grown on a (1$\bar{1}$00) α-Al_2O_3 substrate. For the in-plane pattern, the upper and lower figures correspond to the XRD patterns along azimuth [0001] α-Al_2O_3 and azimuth [11$\bar{2}$0] α-Al_2O_3, respectively. Dotted lines indicate the position of bulk TiO_2. Thickness dependence of (c) out-of-plane lattice parameter *c* and (d) in-plane lattice parameters *a* and *b*, which are extracted from the XRD patterns. Dotted lines indicate the lattice parameters of bulk TiO_2. (e) Orthorhombic distortion *b*/*a* of the resultant TiO_2 films.

Table 4-2. The comparison of lattice mismatch and distortion along [0001] Al_2O_3 and [$11\bar{2}0$] Al_2O_3 direction.

Substrate orientation	0001	$11\bar{2}0$
Film orientation	100	010
Lattice mismatch	−5.9%	+3.5%
Lattice parameter of films	0.457 nm (10 nm) 0.457 nm (300 nm)	0.473 nm (10 nm) 0.461 nm (300 nm)
Relation between lattice parameter and thickness	Weak	Strong

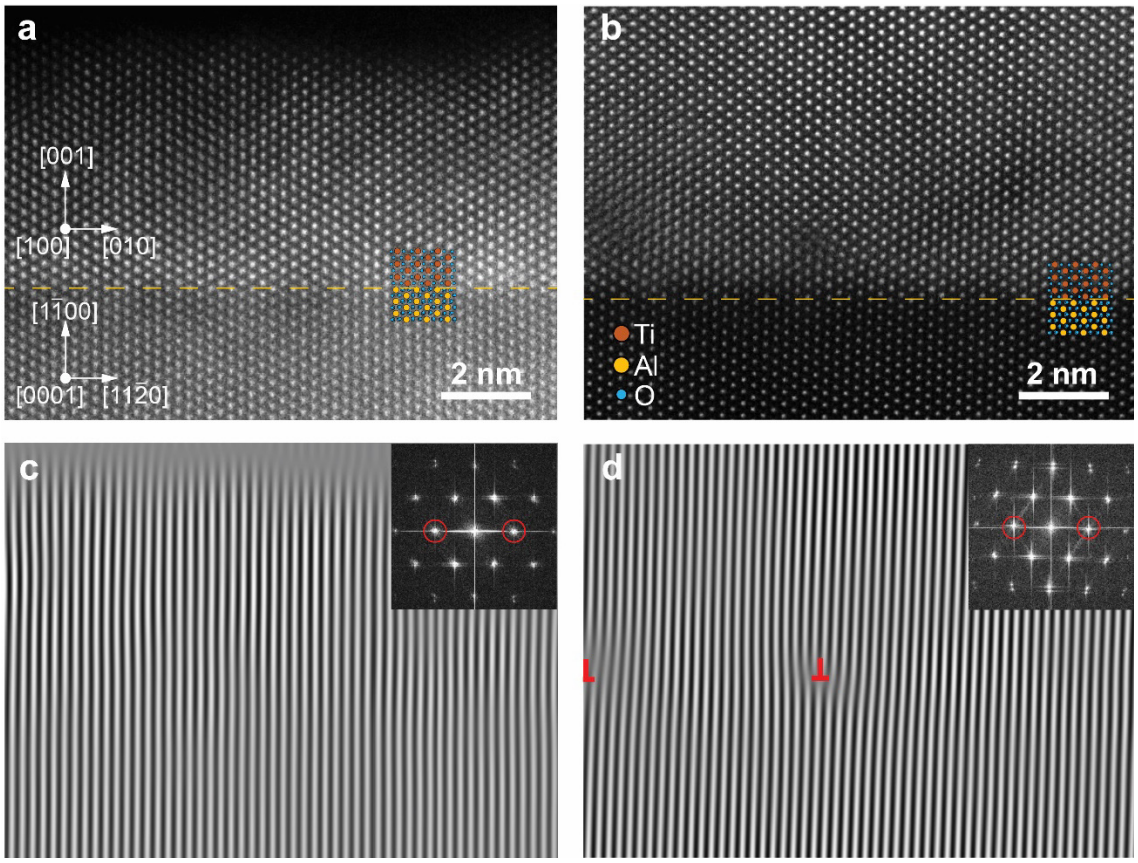

Figure 4-3. Cross-sectional STEM images of the TiO_2 films on an M-plane sapphire substrate. (a, b) HAADF-STEM images of (a) 6-nm-thick and (b) 200-nm-thick TiO_2 films grown on (1$\bar{1}$00) α-Al_2O_3 substrates along the [0001]Al_2O_3 zone axis. Dashed line indicates the interface of TiO_2/α-Al_2O_3 . (c, d) Corresponding IFFT images of (c) 6-nm-thick and (d) 200-nm-thick TiO_2 films. Red marker denotes edge dislocations. Insets are the corresponding FFT patterns.

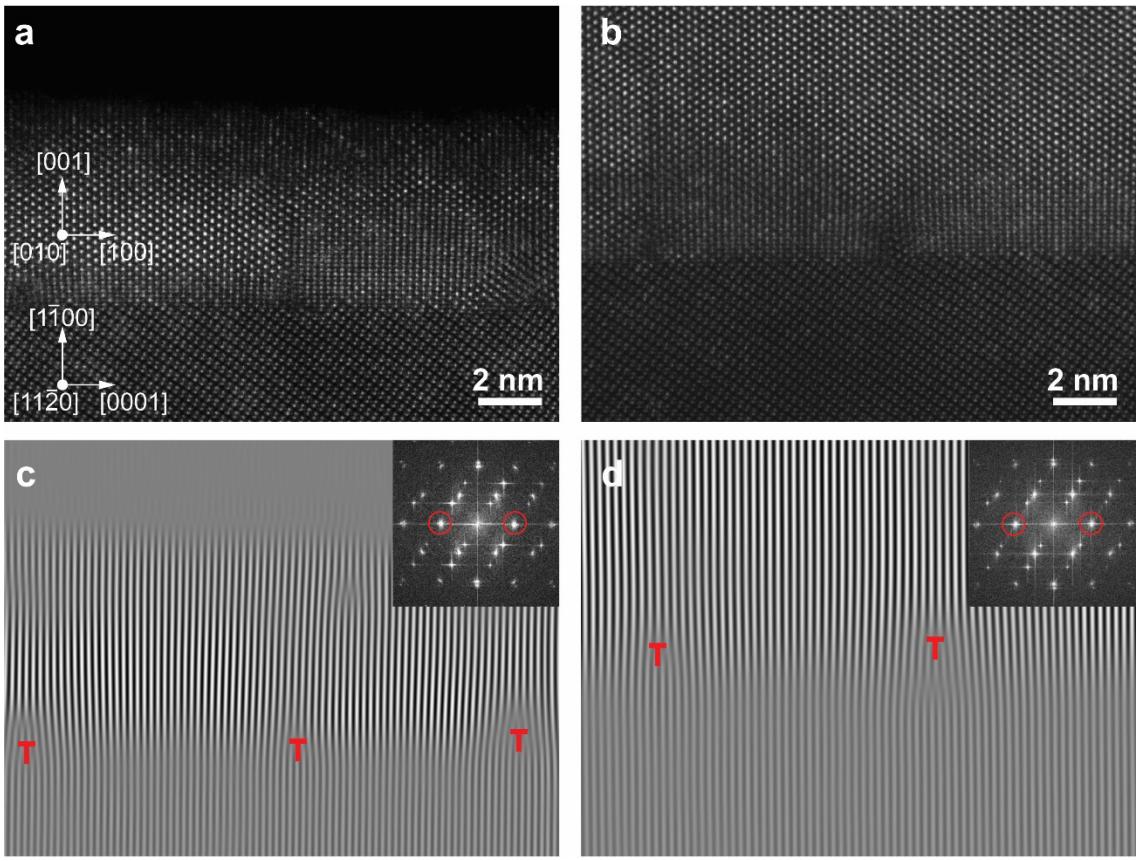

Figure 4-4. Cross-sectional STEM images of the TiO_2 films on an M-plane sapphire substrate. (a, b) The HAADF-STEM images of (a) 6-nm-thick and (b) 200-nm-thick TiO_2 films grown on $(1\bar{1}00)$ α-Al_2O_3 substrates along $[11\bar{2}0]Al_2O_3$ zone axis. (c, d) The corresponding IFFT images of (c) 6-nm-thick and (d) 200-nm-thick TiO_2 films. The edge dislocations were marked by the red marker. The insets are the corresponding FFT patterns.

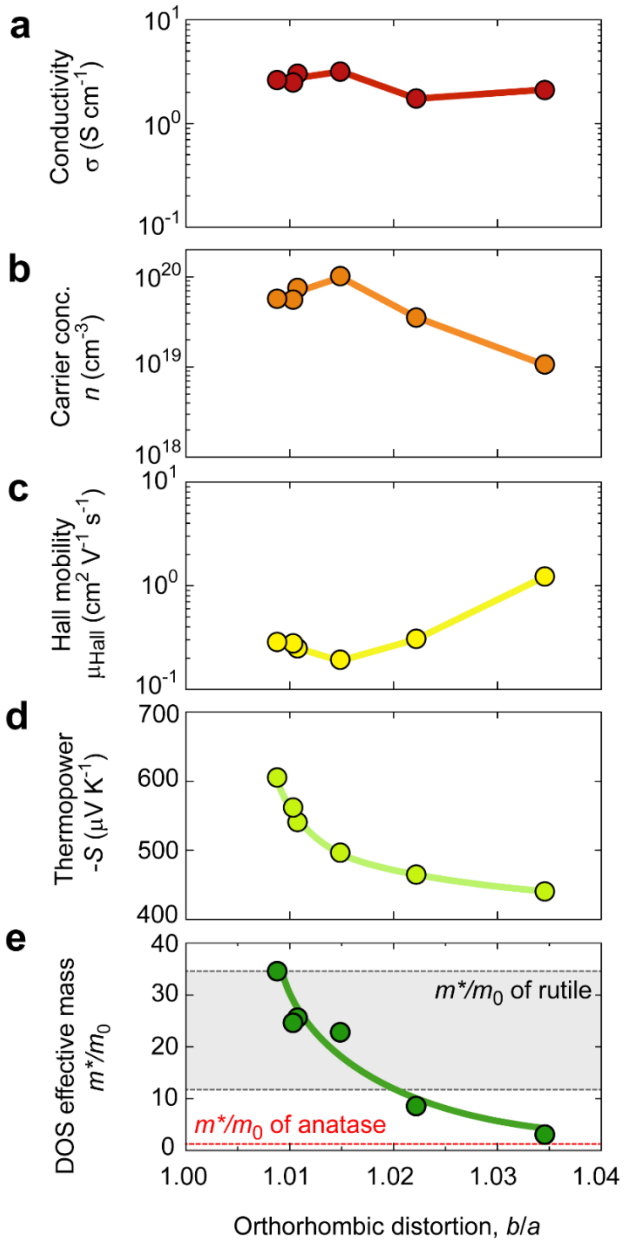

Figure 4-5. Room temperature electron transport properties of the TiO_2 films as the function of the orthorhombic distortion. (a) Electrical conductivity (σ), (b) carrier concentration (n), (c) Hall mobility (μ_{Hall}), (d) Thermopower (S), and (e) DOS effective mass (m^*/m_0). The grey region and red dotted line in (e) indicate the reported effective masses of rutile [28-31] and anatase TiO_2 [32, 33], respectively. Solid lines are to guide the eye. Note that n decreases while $|S|$ increases with b/a.

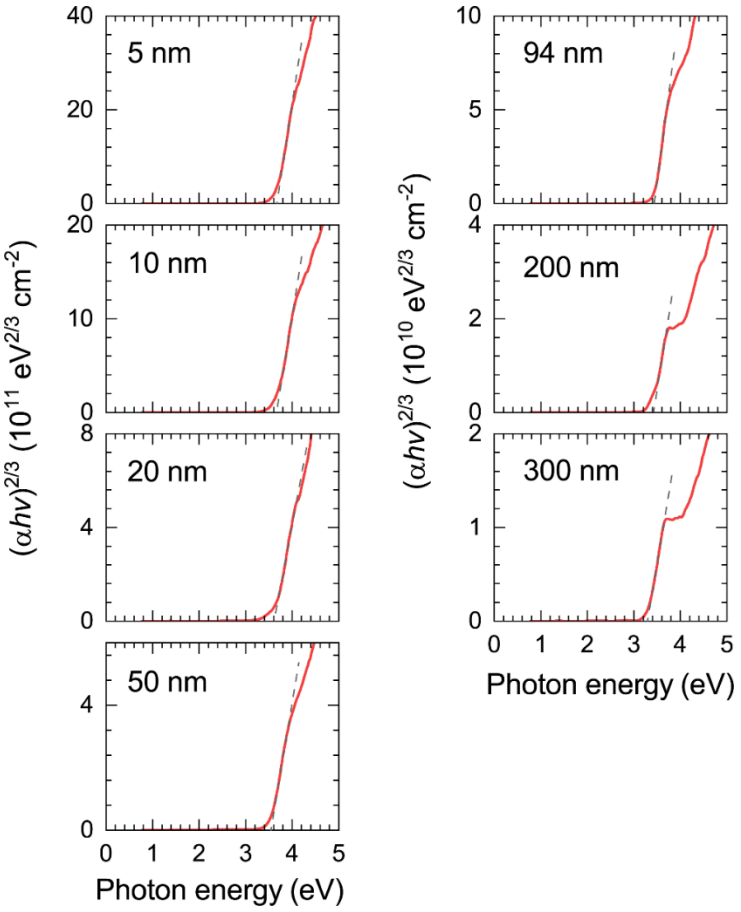

Figure 4-6. Optical property of TiO_2 films. Tauc plots ($(\alpha hv)^{1/2} - hv$) of the 5 – 300-nm-thick rutile TiO_2 films grown on $(1\bar{1}00)$ α-Al_2O_3 substrates. The bandgaps (E_g) are extracted using the dotted lines.

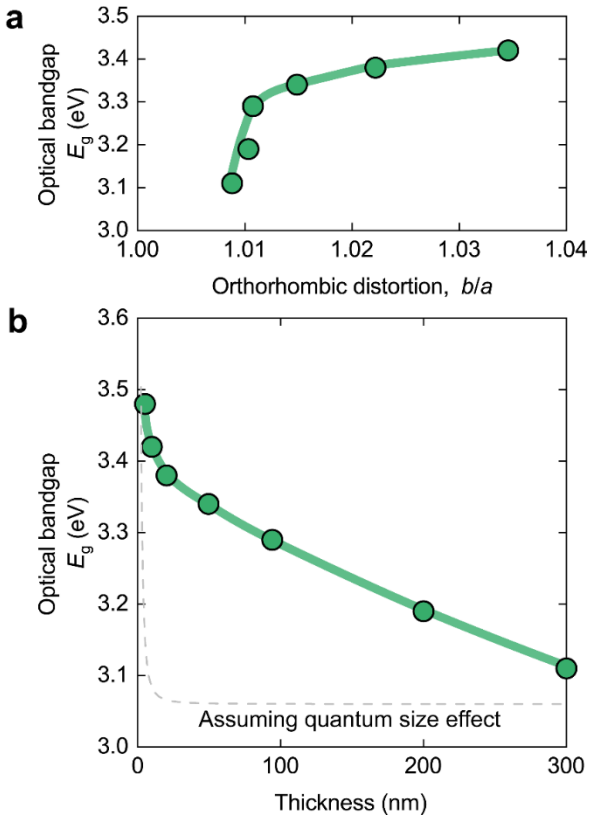

Figure 4-7. Denying the quantum size effect of TiO_2 epitaxial films. Change in E_g of the TiO_2 films. (a) E_g increases with b/a. (b) E_g increases as the thickness decreases. This increasing tendency completely differs from the assumption for the quantum size effect.

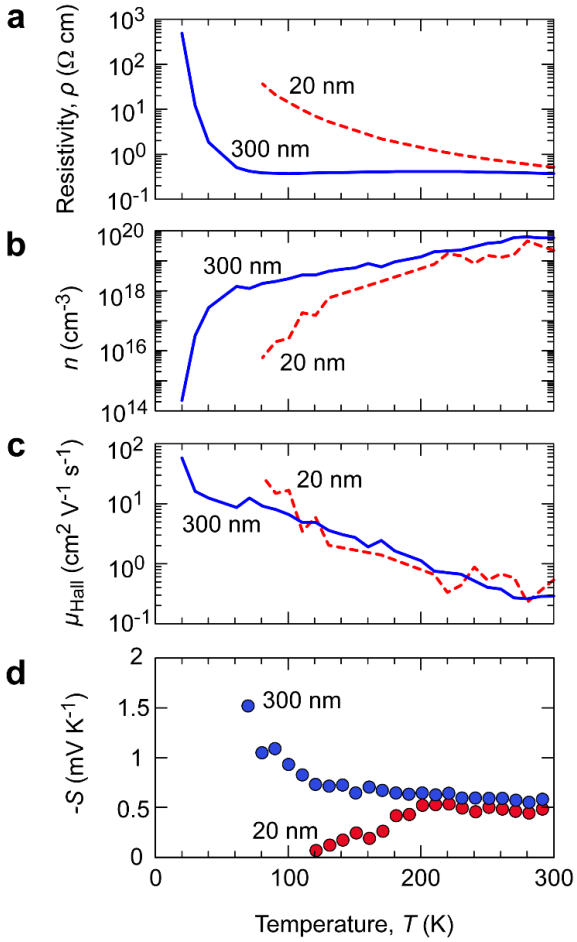

Figure 4-8. Low temperature electron transport properties of the TiO_2 films. (a) Resistivity, (b) carrier concentration (n), (c) Hall mobility (μ_{Hall}), and (d) thermopower (S) of 20- and 300-nm-thick rutile TiO_2 films grown on $(1\bar{1}00)$ α-Al_2O_3 substrates. Note that the $|S| - T$ curve of the 300-nm-thick TiO_2 is similar to that of the reduced rutile TiO_2 single crystal, whereas that of the 20-nm-thick TiO_2 is similar to that of anatase TiO_2 epitaxial film.

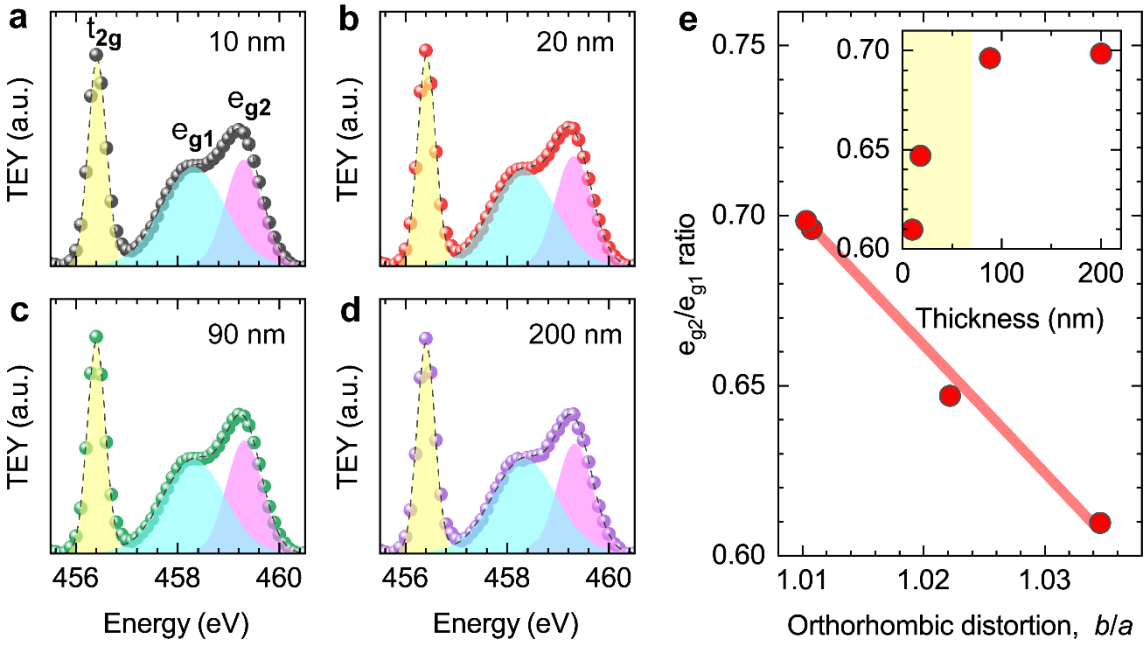

Figure 4-9. Ti L_3 XAS spectra of the 10 − 200-nm-thick rutile TiO_2 films. (a) 10-nm-thick TiO_2, (b) 20-nm-thick TiO_2, (c) 90-nm-thick TiO_2, and (d) 200-nm-thick TiO_2 grown on $(1\bar{1}00)$ α-Al_2O_3 substrates. Peak fitting is processed by the Gaussian distribution. (e) Relative peak area ratio of e_{g2}/e_{g1} as a function of orthorhombic distortion. Inset plots the e_{g2}/e_{g1} ratio as a function of film thickness.

Table 4-3. Ti L_3 XAS spectra peak fitting parameters

	t_{2g}			e_{g1}			e_{g2}		
Thickness	Energy (eV)	Area	FWHM	Energy (eV)	Area	FWHM	Energy (eV)	Area	FWHM
10 nm	456.417	0.364	0.422	458.300	0.606	1.463	459.294	0.370	0.833
20 nm	456.411	0.366	0.417	458.307	0.590	1.466	459.301	0.382	0.833
90 nm	456.404	0.370	0.419	458.302	0.549	1.405	459.307	0.398	0.832
200 nm	456.409	0.365	0.416	458.313	0.561	1.421	459.318	0.392	0.830

Reference

[1] Dette, C.*, et al.*, TiO_2 Anatase with a Bandgap in the Visible Region. *Nano Lett.* **14**, 6533-6538 (2014).

[2] Etacheri, V.*, et al.*, Visible-light Activation of TiO_2 Photocatalysts: Advances in Theory and Experiments. *J. Photoch. Photobio. C* **25**, 1-29 (2015).

[3] Nair, R.V.*, et al.*, A Review on Optical Bandgap Engineering in TiO_2 Nanostructures via Doping and Intrinsic Vacancy Modulation Towards Visible Light Applications. *J. Phys. D: Appl. Phys.* **55**, 313003 (2022).

[4] Fujishima, A. and K. Honda, Electrochemical Photolysis of Water at a Semiconductor Electrode. *Nature* **238**, 37-38 (1972).

[5] Daghrir, R., P. Drogui, and D. Robert, Modified TiO_2 For Environmental Photocatalytic Applications: A Review. *Ind. Eng. Chem. Res.* **52**, 3581-3599 (2013).

[6] Schneider, J.*, et al.*, Understanding TiO_2 Photocatalysis: Mechanisms and Materials. *Chem. Rev.* **114**, 9919-9986 (2014).

[7] Lan, Y.C., Y.L. Lu, and Z.F. Ren, Mini Review on Photocatalysis of Titanium Dioxide Nanoparticles and Their Solar Applications. *Nano Energy* **2**, 1031-1045 (2013).

[8] Arroyo-de Dompablo, M.E., A. Morales-Garcia, and M. Taravillo, DFT+*U* Calculations of Crystal Lattice, Electronic Structure, and Phase Stability under Pressure of TiO_2 Polymorphs. *J. Chem. Phys.* **135**, 054503 (2011).

[9] Hu, Y.X.*, et al.*, Lattice Distortion Induced Internal Electric Field in TiO_2 Photoelectrode for Efficient Charge Separation and Transfer. *Nat. Commun.* **11**, 2129 (2020).

[10] Rahimi, N., R.A. Pax, and E.M. Gray, Review of Functional Titanium Oxides. I: TiO_2 and Its Modifications. *Prog Solid State Ch* **44**, 86-105 (2016).

[11] Luttrell, T.*, et al.*, Why Is Anatase a Better Photocatalyst Than Rutile? - Model

Studies on Epitaxial TiO_2 Films. *Sci. Rep.* **4**, 4043 (2014).

[12] Nishikawa, M.*, et al.*, Effect of Lattice Distortion on Photocatalytic Performance of TiO_2. *Catal. Lett.* **147**, 292-300 (2017).

[13] Li, J.*, et al.*, Microstructure and Dielectric Properties of (Nb + In) Co-Doped Rutile TiO_2 Ceramics. *J. Appl. Phys.* **116**, 074105 (2014).

[14] Usui, H.*, et al.*, Nb-Doped Rutile TiO_2: a Potential Anode Material for Na-ion Battery. *ACS Appl Mater Interfaces* **7**, 6567-6573 (2015).

[15] Blochl, P.E., Projector Augmented-Wave Method. *Phys. Rev. B* **50**, 17953-17979 (1994).

[16] Kresse, G. and J. Hafner, Ab-Initio Molecular-Dynamics for Open-Shell Transition-Metals. *Phys. Rev. B* **48**, 13115-13118 (1993).

[17] Perdew, J.P., K. Burke, and M. Ernzerhof, Generalized Gradient Approximation Made Simple. *Phys. Rev. Lett.* **77**, 3865-3868 (1996).

[18] Dudarev, S.L.*, et al.*, Electron-energy-loss Spectra and the Structural Stability of Nickel Oxide: An LSDA+*U* Study. *Phys. Rev. B* **57**, 1505-1509 (1998).

[19] Han, X.P. and G.S. Shao, Electronic Properties of Rutile TiO_2 with Nonmetal Dopants from First Principles. *J. Phys. Chem. C* **115**, 8274-8282 (2011).

[20] Howard, C.J., T.M. Sabine, and F. Dickson, Structural and Thermal Parameters for Rutile and Anatase. *Acta Crystallogr. B* **47**, 462-468 (1991).

[21] Huy, H.A.*, et al.*, Calculation of Carrier-Concentration-Dependent Effective Mass in Nb-doped Anatase Crystals of TiO_2. *Phys. Rev. B* **83**, 155201 (2011).

[22] Tang, H.*, et al.*, Urbach Tail of Anatase TiO_2. *Phys. Rev. B* **52**, 7771-7774 (1995).

[23] Heyd, J., G.E. Scuseria, and M. Ernzerhof, Hybrid Functionals Based on a Screened Coulomb Potential. *J. Chem. Phys.* **118**, 8207-8215 (2003).

[24] Krukau, A.V.*, et al.*, Influence of the Exchange Screening Parameter on the Performance of Screened Hybrid Functionals. *J. Chem. Phys.* **125**, 224106 (2006).

[25] Sun, X., *et al.*, Dislocation-Induced Stop-and-Go Kinetics of Interfacial Transformations. *Nature* **607**, 708-713 (2022).

[26] Zhang, Z., *et al.*, The Peculiarity of the Metal-Ceramic Interface. *Sci. Rep.* **5**, 11460 (2015).

[27] Vining, C.B., A Model for the High-Temperature Transport-Properties of Heavily Doped N-Type Silicon-Germanium Alloys. *J. Appl. Phys.* **69**, 331-341 (1991).

[28] Thurber, W.R. and A.J.H. Mante, Thermal Conductivity and Thermoelectric Power of Rutile (TiO_2). *Phys. Rev.* **139**, A1655 (1965).

[29] Itakura, M., *et al.*, Hall Effect and Thermoelectric Power in Semiconductive TiO_2. *Jpn. J. Appl. Phys.* **6**, 311-317 (1967).

[30] Frederiksen, H., Recent Studies on Rutile (TiO_2). *J. Appl. Phys.* **32**, 2211-2215 (1961).

[31] Deford, J.W. and O.W. Johnson, Electron-Transport Properties in Rutile from 6 to 40 K. *J. Appl. Phys.* **54**, 889-897 (1983).

[32] Tang, H., *et al.*, Electrical and Optical-Properties of TiO_2 Anatase Thin-Films. *J. Appl. Phys.* **75**, 2042-2047 (1994).

[33] Kurita, D., *et al.*, Carrier Generation and Transport Properties of Heavily Nb-doped Anatase TiO_2 Epitaxial Films at High Temperatures. *J. Appl. Phys.* **100**, 096105 (2006).

[34] Kavan, L., *et al.*, Electrochemical and Photoelectrochemical Investigation of Single-Crystal Anatase. *J Am Chem Soc* **118**, 6716-6723 (1996).

[35] Scanlon, D.O., *et al.*, Band Alignment of Rutile and Anatase TiO_2. *Nat. Mater.* **12**, 798-801 (2013).

[36] Mathieu, H., J. Pascual, and J. Camassel, Uniaxial Stress Dependence of the Direct-Forbidden and Indirect-Allowed Transitions of TiO_2. *Phys. Rev. B* **18**, 6920-6929 (1978).

[37] Ekuma, C.E. and D. Bagayoko, Ab-initio Electronic and Structural Properties of

Rutile Titanium Dioxide. *Jpn. J. Appl. Phys.* **50**, 101103 (2011).

[38] Yamada, Y. and Y. Kanemitsu, Blue Photoluminescence of Highly Photoexcited RutileTiO_2: Nearly Degenerate Conduction-Band Effects. *Phys. Rev. B* **82**, 113103 (2010).

[39] Huang, P.R., *et al.*, Impact of Lattice Distortion and Electron Doping on Alpha-MoO_3 Electronic Structure. *Sci. Rep.* **4**, 7131 (2014).

[40] Lockwood, D.J., Z.H. Lu, and J.M. Baribeau, Quantum Confined Luminescence in Si/SiO_2 Superlattices. *Phys. Rev. Lett.* **76**, 539-541 (1996).

[41] Liang, D.D., *et al.*, Thickness Optimization toward High-Performance Bottom-Gated Transparent Tin Dioxide Thin-Film Transistors. *ACS Appl. Electron. Mater.* **2**, 3454-3458 (2020).

[42] Dong, S., *et al.*, Valence Band of Rutile TiO_2(110) Investigated by Polarized-Light-Based Angle-Resolved Photoelectron Spectroscopy. *J. Phys. Chem. Lett.* **13**, 2299-2305 (2022).

[43] Tang, J.K., *et al.*, Colossal Positive Seebeck Coefficient and Low Thermal Conductivity in Reduced TiO_2. *J. Phys. Condens. Matter.* **21**, 205703 (2009).

[44] Takahashi, H., *et al.*, Colossal Seebeck Effect Enhanced by Quasi-ballistic Phonons Dragging Massive Electrons in $FeSb_2$. *Nat. Commun.* **7**, 12732 (2016).

[45] Frederikse, H.P.R., W.R. Thurber, and W.R. Hosler, Electronic Transport in Strontium Titanate. *Phys. Rev.* **134**, A442-A445 (1964).

[46] Matsuura, H., *et al.*, Effect of Phonon Drag on Seebeck Coefficient Based on Linear Response Theory: Application to $FeSb_2$. *J Phys Soc Jpn* **88**, 074601 (2019).

[47] Emelyanenko, O.V., *et al.*, Phonon Drag in P-Gaas. *Phys. Status Solidi* **12**, K89 (1965).

[48] Ruus, R., *et al.*, Ti 2*p* and O 1*s* X-ray Absorption of TiO_2 Polymorphs. *Solid State Commun.* **104**, 199-203 (1997).

[49] Zhang, X.H., *et al.*, FeO_6 Octahedral Distortion Activates Lattice Oxygen in

Perovskite Ferrite for Methane Partial Oxidation Coupled with CO_2 Splitting. *J Am Chem Soc* **142**, 11540-11549 (2020).

[50] Vasquez, G.C.*, et al.*, Understanding the Effects of Cr Doping in Rutile TiO_2 by DFT Calculations and X-ray Spectroscopy. *Sci. Rep.* **8**, 8740 (2018).

[51] Kamisaka, H.*, et al.*, Density Functional Theory Based First-principle Calculation of Nb-doped anatase TiO_2 and Its Interactions with Oxygen Vacancies and Interstitial Oxygen. *J. Chem. Phys.* **131**, 034702 (2009).

[52] Zhang, J.F.*, et al.*, New Understanding of the Difference of Photocatalytic Activity Among Anatase, Rutile and Brookite TiO_2. *Phys. Chem. Chem. Phys.* **16**, 20382-20386 (2014).

Chapter 5. A Comparison Study of Strain Condition and Properties of Epitaxial Rutile TiO_2 and SnO_2 Films Grown on M-plane Sapphire

5.1. Objective of this chapter

In chapter 4, the orthorhombic distortion was successfully introduced into epitaxial TiO_2 films by fabricating the film on $(1\bar{1}00)$ α-Al_2O_3 substrates. Accordingly, the optoelectronic properties as well as the electronic structure were modulated due to this distortion. It should be noted that rutile structured oxides are a large family of materials as mentioned in the chapter 1.1. It remains a question whether all the rutile structured oxides are possible to introduce the distortion in same way. In fact, the answer is no. In the chapter, a comparison study between rutile TiO_2 and SnO_2 was proposed to point out the absence of orthorhombic distortion in SnO_2 films.

SnO_2 is another well-known oxide material with rutile structure. Compared to TiO_2, two features are worth pointing out: one point is addressed on the crystal structure where the SnO_2 has a larger lattice parameter of a = 0.4737 nm and c = 0.3186 nm (for TiO_2, a = 0.4594 nm, c = 0.2958 nm). As mentioned in chapter 1.2.3, epitaxial growth of a film is highly dependent on the mismatch determined by the lattice parameter. Concomitantly, the condition of distortion is also related to it. When SnO_2 grown on

$(1\bar{1}00)$ α-Al_2O_3 substrates, an extremely large mismatch is estimated along the direction of [0001] α-Al_2O_3 (**Figure 5-1**). Another point is the specific composition of band structure. The band edge of SnO_2 consists of the Sn 5s-based conduction band minimum (CBM) and the O 2p-based valence band maximum (VBM). Since the Sn 5s orbitals shows larger orbital radius and spherical symmetry, it is easier to overlap with each other, allowing the freer movement of electrons and smaller electron effective mass (m^*). Thus, SnO_2 becomes a promising candidate of transparent conducing oxide (TCO) Thus, electron-doped SnO_2 is considered as a great candidate of transparent conducing oxide (TCO) [1, 2], when increasing its carrier concentration (n_s) by artificial methods, such as chemical doping, vacuum annealing, etc [1-4]. In chapter 2, the increase of ns in VO_2 films was achieved by introduction of orthorhombic distortion [5]. According to this, it is worthwhile to clarify whether similar increase of ns can be achieved in SnO_2 films for TCO related applications.

In this chapter, epitaxial SnO_2 films were fabricated on $(1\bar{1}00)$ α-Al_2O_3 substrates to evaluate the strain effect on SnO_2 films. As the result, an unconventional strain absence was observed even in the film with thickness of ~10 nm. By comparing with TiO_2 film with similar thickness, such absence was attributed to the combination of large mismatch induced high strain relaxation and the negligible mismatch induced unstrained state. Although no orthorhombic distortion was introduced, the optoelectronic properties of SnO_2 films were still investigated, pointing out that the effectiveness of orthorhombic

distortion on optoelectronic properties of rutile structured oxide films from another perspective.

5.2. Experimental

***Sample preparation*:** Both 0.5%Nb:TiO_2 and SnO_2 epitaxial films were fabricated on $(1\bar{1}00)$ α-Al_2O_3 substrates by pulsed laser deposition (PLD) method, where a KrF excimer laser (λ = 248 nm, fluence ~1.0 J cm^{-2} $pulse^{-1}$, repetition rate = 10 Hz) was employed to irradiate the pre-doped stoichiometric ceramic targets. The oxygen pressure (P_{O2}) was maintained at 5×10^{-3} Pa during growth of both films, whereas the substrate temperatures (T_{sub}) of 500 °C and 700 °C were adopted for optimal growth of Nb:TiO_2 and SnO_2.

***Crystallographic analyses*:** The crystallographic orientation and lattice parameters of resultant films were evaluated though the high-resolution X-ray diffraction (XRD, ATX-G, Rigaku Co.) with Cu $K\alpha_1$ (λ = 0.154059 nm) radiation. High-angle annular dark field (HAADF)-STEM observation was performed using STEM (ARM200CF, JEOL Co. Ltd).

***Electrical and optical properties measurements*:** The electron transport property (ρ, n, μ_{Hall}) measurements at room temperature and with variable temperature were performed

using the dc four-probe method with the van der Pauw electrode configuration. Thermopower (*S*) at room temperature was measured by the conventional steady-state method. The transmission and reflection spectra in the 200 − 1600 nm wavelength range were evaluated by a spectrophotometer (SolidSpec-3700, Shimadzu Co.).

5.3. Result and discussion

Figure 5-2 summarizes the X-ray diffraction (XRD) patterns of the resultant 0.5% Nb doped TiO_2 (0.5%Nb:TiO_2) and SnO_2 epitaxial films grown on $(1\,\bar{1}\,00)$ α-Al_2O_3 substrates. Both intense 002 Nb:TiO_2 and SnO_2 diffraction peaks were observed along with that of $3\bar{3}00$ α-Al_2O_3 substrate, and no peaks of other crystal planes appeared in wide range patterns, suggesting the epitaxy with high *c*-axis orientation (**Figure 5-2(a)** and **2(b)**). The average crystalline tilt angles were revealed by X-ray rocking curves, where the similar values of full width at half maximum (FWHM) indicates the similar crystallinity (**Figure 5-2(a)** and **2(b)**, **inset**). For the in-plane XRD patterns, the 400 and 040 peaks of Nb:TiO_2 located at $\sim q_{x\text{ or }y}/2\pi$ = 8.75 and 8.65 nm^{-1}, respectively, where the former is slightly larger than that of the bulk, whereas the latter is smaller (**Figure 5-2(c)** and **2(e)**). This indicates that the Nb:TiO_2 film received high strain from α-Al_2O_3 substrate. On the contrary, the 400 and 040 peaks of SnO_2 have the similar positions around $\sim q_{x\text{ or }y}/2\pi$ = 8.47 nm^{-1}, which is also consistent with the bulk value (**Figure 5-2(d)** and **2(f)**). The absence of such difference suggests that SnO_2 film has been fully

relaxed. Noting that both Nb:TiO_2 and SnO_2 films with different thickness of ~10 − 90 nm were also fabricated on $(1\bar{1}00)$ α-Al_2O_3 substrates. The in-plane lattice parameters of former show clear thickness dependence while those of SnO_2 remain almost constant, suggesting that the strain relaxation of SnO_2 films occurs even when the film is extremely thin (**Figure 5-2(e)** and **2(f)**, **inset**).

To elucidate reason why there is the difference in strain condition between Nb:TiO_2 and SnO_2 films, cross-sectional STEM observations along $[1\bar{1}00]$ and [0001] Al_2O_3 zone axis were performed for TiO_2 and SnO_2 films grown on $(1\bar{1}00)$ α-Al_2O_3 substrates, shown in **Figure 5-3**. HAADF-STEM images (**Figure 5-3(a)**, **3(c)**, **3(e)** and **3(g)**) show that the atomic arrangements of both TiO_2 and SnO_2 film are consistent with that of (001) oriented rutile structure.

For the epitaxial films, strain is usually released through dislocations, which can be visualized through inverse fast Fourier transform (IFFT) analyses. **Figure 5-3(b)**, **3(d)**, **3(f)**, and **3(h)** summarized the corresponding IFFT images, in which the edge dislocations were denoted by red markers. The dislocations were observed along both $[1\bar{1}20]$ and [0001] Al_2O_3 zone axis with the spacing of ~8.5 − 10 nm in TiO_2 film, indicating that strain relaxation occurs along these two directions (**Figure 5-3(b)** and **3(d)**). For SnO_2 film, on the one hand, dislocations were only observed along the $[1\bar{1}20]$ Al_2O_3 zone axis with extremely large mismatch of −9.2%. The dislocation spacing was

estimated as ~4.8 nm, which is much smaller than that of TiO_2 film, may suggest that a higher degree of dislocation induced strain relaxation along [$1\bar{1}20$] Al_2O_3 zone axis in SnO_2 film (**Figure 5-3(f)**). On the other hand, due to the negligible mismatch (+0.5%) along [0001] Al_2O_3 direction, no dislocation was found along this direction, corresponding to the absence of strain and intrinsic coherent growth (**Figure 5-3(h)**). Herein, the results indicated that the complete strain release of SnO_2 is possibly due to the combination of large mismatch induced high strain relaxation and the negligible mismatch induced strain absence, while the moderate mismatch between TiO_2 and substrate results in the (partially) strained condition.

Figure 5-4 summarizes the electron transport properties of 0.5%Nb:TiO_2 and SnO_2 films at room temperature (RT). The conductivity (σ) of Nb:TiO_2 is ~1.7 − 3.2 S cm^{-1}, whereas SnO_2 shows much higher σ of ~10 − 36 S cm^{-1} (**Figure 5-4(a)** and 5-**4(b)**). Although both exhibit distinct conductivity, the conducting nature differs between these two: the conduction of Nb:TiO_2 is due to the increase of carrier concentration induced by electron doping, while SnO_2 has intrinsic high electron mobility, resulting in better σ. Such differences are further revealed by Hall measurements shown in **Figure 5-4(c−f)**. The results of Hall measurements revealed that both Nb:TiO_2 and SnO_2 are n-type semiconductor. The carrier concentrations (n) of 0.5%Nb:TiO_2 gradually increases from ~10^{19} cm^{-3} to a saturated value of ~10^{20} cm^{-3} with increasing thickness (**Figure 5-4(c)**), which is close to the theoretical dopant contributed electron concentration (0.5%Nb ≈

1.6×10^{20} cm^{-3}) and overall higher than that of SnO2 of ~$5 \times 10^{18} - 2 \times 10^{19}$ cm^{-3} (**Figure 5-4d**). On the contrary of carrier concentration, the Hall mobility of SnO_2 is ranging from 4 to 42 cm^2 V^{-1} s^{-1}, larger than that of 0.5%Nb:TiO_2 (**Figure 5-4(e)** and (**f)**). The higher mobility of SnO_2 originates from the high degree of orbital overlapping of Sn 5s electrons than that of Ti 5d electrons [6], eventually resulting in the better electrical properties .

Additionally, the thermopower measurements were also performed for the resultant films (**Figure 5-4(g)** and **4(h)**). Both Nb:TiO_2 and SnO_2 show negative seebeck coefficient (*S*), which suggests the dominated carrier is electron (n-type semiconductor), consistent with the results of Hall measurements. Nb:TiO_2 shows a large $-S$ of 440 − 540 μV K^{-1}, while the $-S$ of SnO_2 is ranging from 110 − 200 μV K^{-1}. It was noted that, although the $-S$ of both Nb:TiO_2 and SnO_2 show an upward trend as thickness increases, $-S$ and n of SnO_2 are inversely related to thickness while the two of Nb:TiO_2 show approximately similar increasing trend with thickness. According to the Mott formula, the variation trends of $-S$ and *n* are usually consistent for parabolic electronic density of states (DOS) with constant effective mass (m^*). The different relation of $-S$ and n between Nb:TiO_2 and SnO_2 possibly indicates the difference of evolution of m^* with thickness between the two.

To clarify this, m^* is calculated according to the equation as follows [7]

$$S = -\frac{k_B}{e}\left(\frac{(r+2)F_{r+1}(\xi)}{(r+1)F_r(\xi)} - \xi\right),$$

$$n = 4\pi\left(\frac{2m^* k_B T}{h^2}\right)^{3/2} F_{1/2}(\xi),$$

where k_B, r, ξ, T, and h are the Boltzmann constant, scattering parameter of the relaxation time, chemical potential, absolute temperature, and Plank's constant, respectively. F_r is Fermi integral, which can be further evaluated from the following equation

$$F_r(\xi) = \int_0^\infty \frac{x^r}{1 + e^{x-\xi}}\, dx.$$

Here the m^* of SnO_2 were calculated and plotted as the function of thickness, shown together with that of Nb:TiO_2 in **Figure 5-5**. For Nb:TiO_2, a clear relation between thickness regulated strain condition (orthorhombic distortion) and m^* has been demonstrated in the Chapter 5. Different from the Nb:TiO_2, the absence of such distortion in SnO_2 has been clarified through XRD and STEM observation in this chapter. Correspondingly, the m^* of SnO_2 also shows no thickness dependence and almost keeps a constant of ~0.30 m_0, which is close to the reported value of ~0.28 m_0 [8]. The difference in the trend of m^* between Nb:TiO_2 and SnO_2 points out that, on the one hand, orthorhombic distortion does have a significant effect on the electron structure and transport of rutile-structured oxides; one the other hand, in the special case of epitaxial SnO_2 films grown on M-sapphire, absence of distortion results in the intrinsic-like properties of SnO_2.

In addition to effective mass, another effect induced by orthorhombic distortion lies on the optical bandgap (E_g). In Chapter 5, Nb:TiO_2 has been clarified to exhibit anomalously increasing E_g with decreasing thickness (**Figure 5-6(a)**). The failure of explanation by quantum size effect (QSE) illustrates that orthorhombic distortion contributes to the shift of E_g. In the case of SnO_2, optical transmission (T) and reflection (R) measurements were also performed and the E_g were evaluated by the Tauc plot of $(\alpha hv)^{1/r}$ versus hv, where r = 1/2 for direct transition nature of SnO_2. **Figure 5-6(b)** plots the E_g of SnO_2 as the function of thickness. When the film thickness exceeds ~30 nm, the E_g is almost saturated at ~4.05 eV, which is consistent with previous reports of epitaxial SnO_2 grown on sapphire substrate [9, 10], whereas the E_g dramatically increases as thickness decreases when the film is thinner than ~25 nm. the E_g data was also fitted through the QSE model, which can be expressed as the following equation [11, 12]

$$E_g = E_{g,Bulk} + \frac{h^2}{8d^2}\left(\frac{1}{m_e^*} + \frac{1}{m_h^*}\right)$$

Where $E_{g,Bulk}$, h and d are the E_g of bulk SnO_2 (assumed as the saturated E_g), Planck's constant and film thickness, respectively. The m_e^* and m_h^* are the effective mass of electron and holes of SnO_2, which is assumed to 0.28 m_0 [8] and 0.90 m_0 [13]. Still different from the condition of Nb:TiO_2, in the case of SnO_2, the theoretical change of E_g induced by QSE is well fitted with the observed shift of E_g. This result demonstrates that QSE dominates the dramatic widening of E_g of SnO_2 when thickness is thin. Furthermore, by contrasting this with the case of Nb:TiO_2, the effect of orthorhombic

distortion on the optical properties of rutile structured oxides is verified from another aspect.

5.4. Conclusion

In this chapter, epitaxial SnO_2 films with various thickness were fabricated on $(1\bar{1}00)$ α-Al_2O_3 substrates and compared with TiO_2 films. Different from the TiO_2 grown on same substrates, orthorhombic distortion was no longer observed in this series of SnO_2 film. STEM observations suggest that the absence of distortion possibly originates from the combination of large mismatch induced high strain relaxation and the negligible mismatch induced strain absence. Accordingly, the effective mass of all resultant SnO_2 films is around ~0.3 m_0, independent with film thickness; the optical bandgap increases with decreasing thickness owning to the quantum size effect instead of the contribution of orthorhombic distortion. This study presents a special case to discuss the optoelectronic properties of rutile structured films in the absence of strain, as a contrast, demonstrating the significant effects of strain induced orthorhombic distortion on properties of rutile structured films.

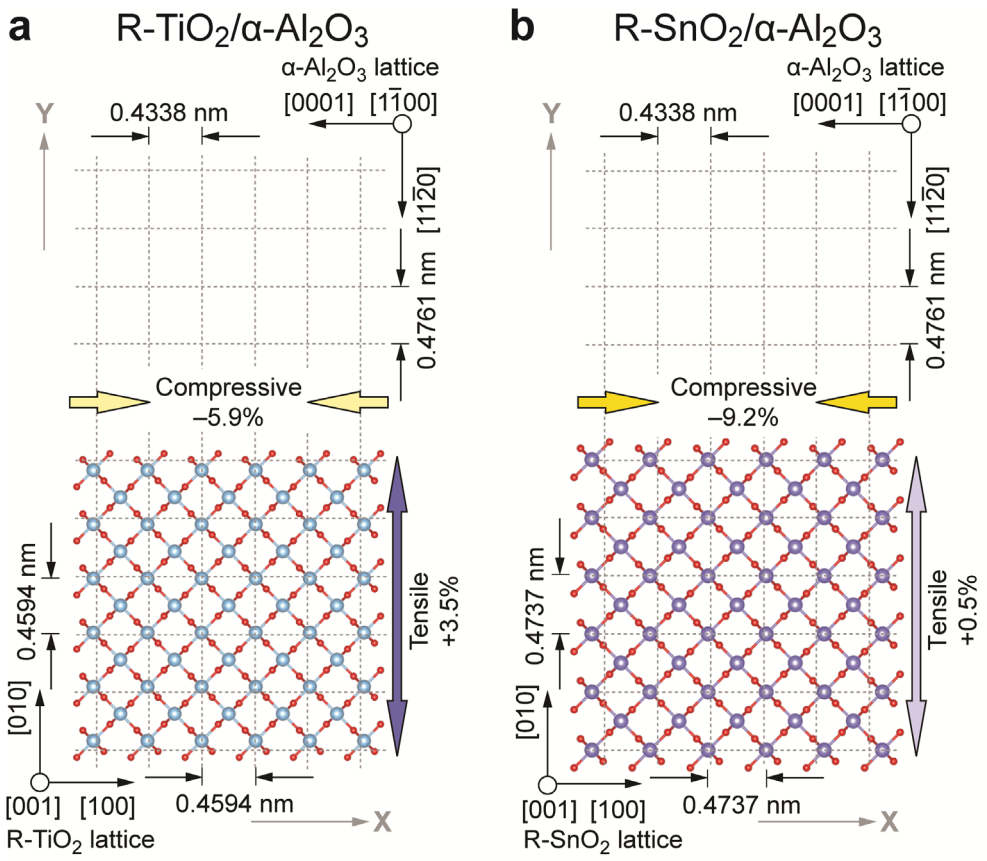

Figure 5-1. The atomic arrangements of rutile TiO_2 and SnO_2 on M-plane sapphire substrate. (a) Schematic crystal lattice of rutile TiO_2 on $(1\bar{1}00)$ α-Al_2O_3 (sublattice of oxide ions, dotted lines). The lattice parameter of TiO_2 along [100] direction is larger than that of α-Al_2O_3 along [0001] (lattice mismatch: −5.9%), suggesting a compressive strain along X direction, whereas tensile strain is assumed along the Y direction ($[11\bar{2}0]$ α-Al_2O_3) due to the relatively small lattice parameter of TiO_2 along this direction compared to that of α-Al_2O_3 (lattice mismatch: +3.5%). (b) Schematic crystal lattice of rutile SnO_2 on $(1\bar{1}00)$ α-Al_2O_3. For SnO_2, the compressive and tensile strain are also assumed along X and Y directions. However, the compressive strain (lattice mismatch: −9.2%) becomes larger whereas tensile strain (lattice mismatch: +0.5%) is smaller compared to these of TiO_2.

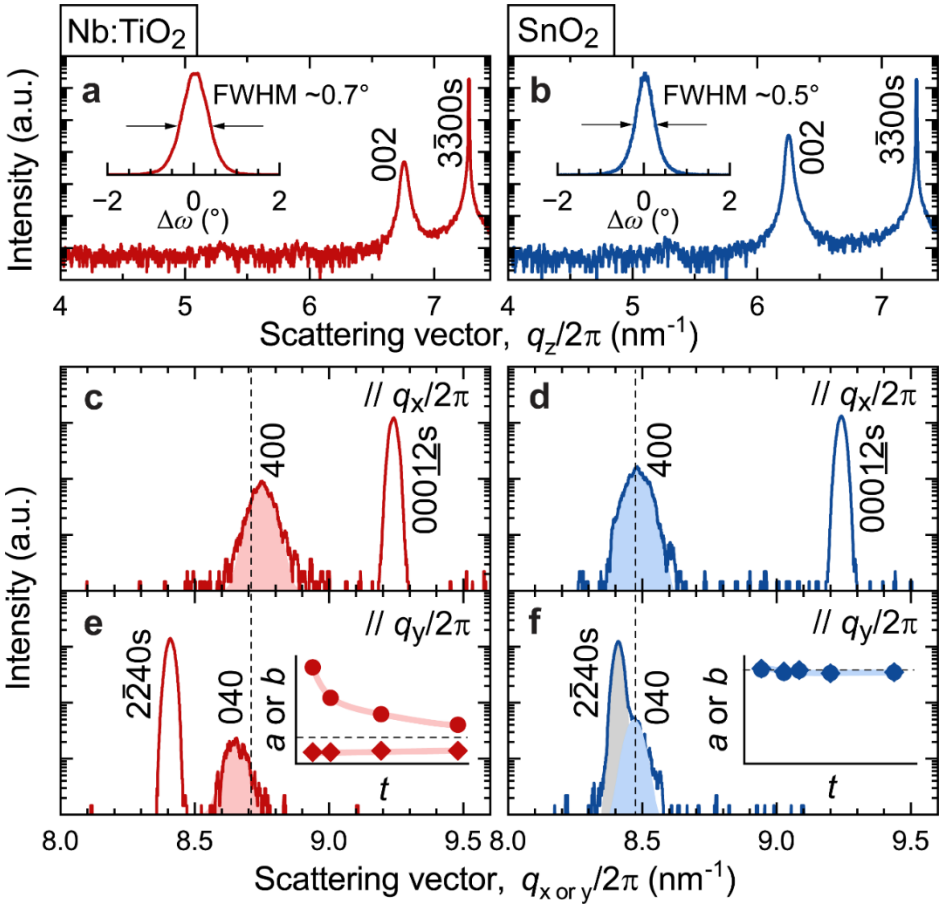

Figure 5-2. X-ray diffraction (XRD) patterns of the resultant Nb:TiO_2 and SnO_2 film on M-plane sapphire substrate. (a, b) Out-of-plane XRD patterns of (a) 94-nm-thick 0.5%Nb:TiO_2 and (b) 87-nm-thick SnO_2 grown on $(1\bar{1}00)$ α-Al_2O_3 substrates. The insets are the corresponding X-ray rocking curves ($\Delta\omega$). (c–f) In-plane XRD patterns of (c, e) 94-nm-thick 0.5%Nb:TiO_2 and (d, f) 87-nm-thick SnO_2 grown on $(1\bar{1}00)$ α-Al_2O_3 substrates along azimuth [0001] α-Al_2O_3 ($//q_x/2\pi$) and azimuth $[11\bar{2}0]$ α-Al_2O_3 ($//q_y/2\pi$), respectively. The dotted lines indicate the position of bulk. Both films with different thicknesses were also fabricated and the change tendency of in-plane lattice parameters are shown in the inset figures.

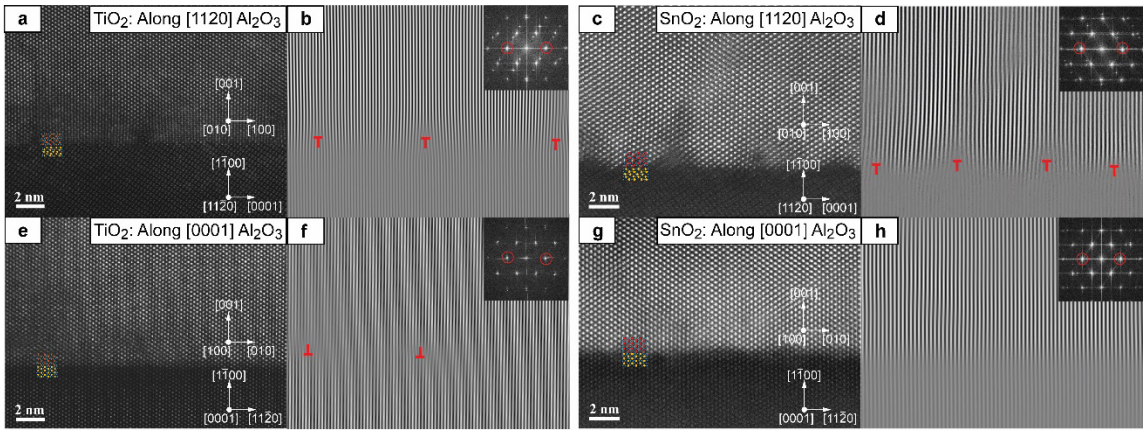

Figure 5-3. Cross-sectional STEM images of the TiO_2 and SnO_2 films on M-plane sapphire substrates. (a, c, e, g) HAADF-STEM images of (a, e) TiO_2 and (c, g) SnO_2 films on $(1\bar{1}00)$ α-Al_2O_3 substrates along the (a, c) $[11\bar{2}0]$ and (e, g) [0001] Al_2O_3 zone axis. (b, d, f, h) The corresponding inverse fast Fourier transform (IFFT) images, in which the edge dislocations were denoted by red markers. The insets are the corresponding FFT patterns.

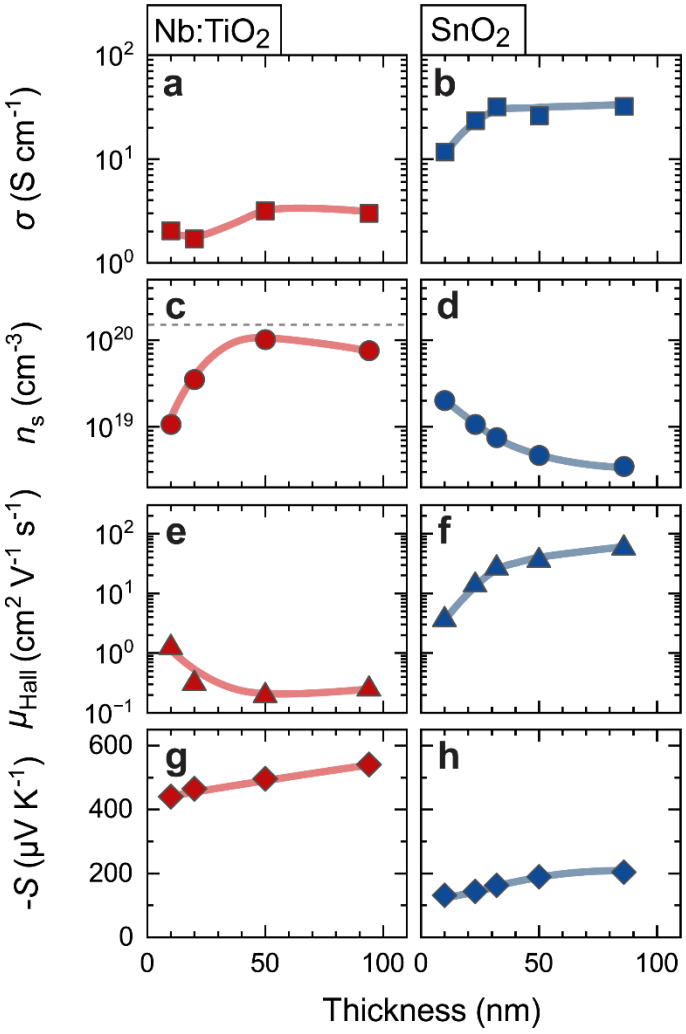

Figure 5-4. Room temperature electron transport properties of the Nb:TiO_2 and SnO_2 films on M-plane sapphire substrates. (a, b) Electrical conductivity (σ), (c, d) carrier concentration (n), (e, f) Hall mobility (μ_{Hall}), and (g, h) Thermopower (S). Solid lines are to guide the eye. The dotted line in (c) indicates the theoretical carrier concentration contributed by 0.5% Nb doping.

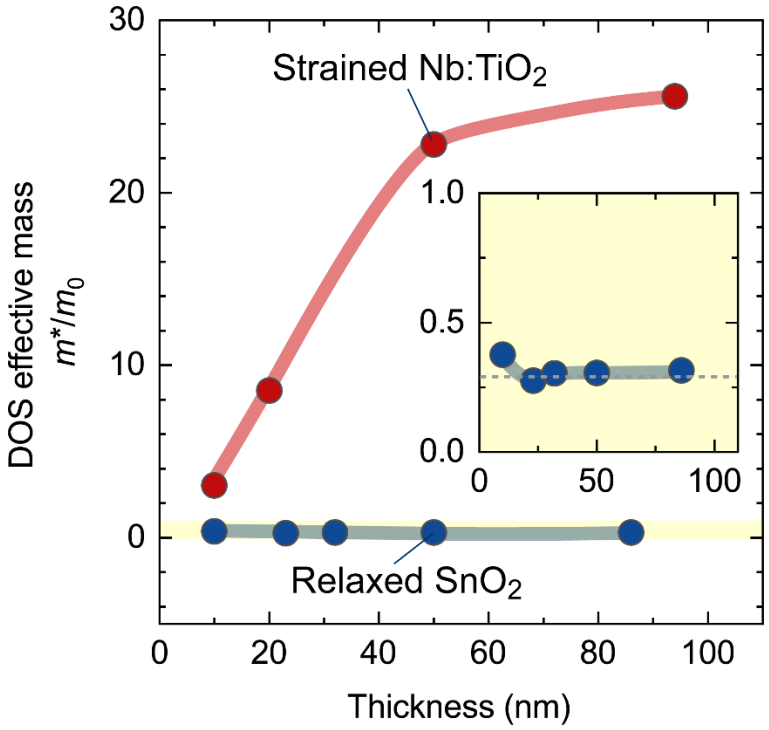

Figure 5-5. Density of state effective mass (m^*/m_0) of Nb:TiO_2 and SnO_2 films as the function of thickness. Nb:TiO_2 is strained and the lattice is orthorhombic distorted, while SnO_2 shows no strain and distortion. The inset is the enlarged view of SnO_2, in which the dashed line indicates the theoretical mass of SnO_2.

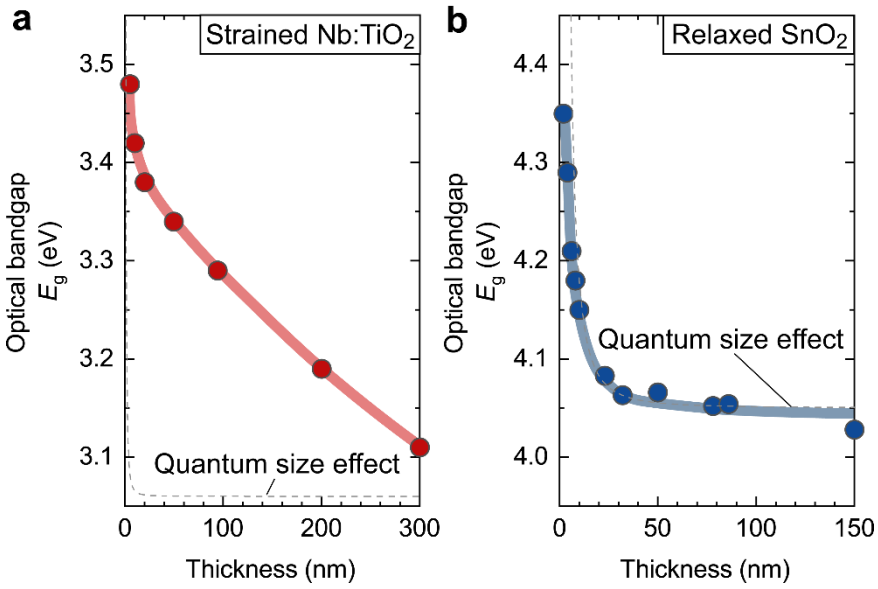

Figure 5-6. Optical bandgap (E_g) of Nb:TiO_2 and SnO_2 films as the function of thickness. (a) strained Nb:TiO_2, (b) relaxed SnO_2. The dashed lines represent the change trend of E_g when only quantum size effect validates.

References

[1] Williamson, B.A.*, et al.*, Resonant Ta Doping for Enhanced Mobility in Transparent Conducting SnO_2. *Chem. Mater.* **32**, 1964-1973 (2020).

[2] Dixon, S.C.*, et al.*, n-Type Doped Transparent Conducting Binary Oxides: an Overview. *J. Mater. Chem. C* **4**, 6946-6961 (2016).

[3] Sato, K.*, et al.*, Highly Textured SnO_2: F TCO Films for a-Si Solar Cells. *Asahi Garasu Kenkyu Hokoku* **42**, 129-137 (1993).

[4] Montero, J., J. Herrero, and C. Guillén, Preparation of Reactively Sputtered Sb-doped SnO_2 Thin Films: Structural, Electrical and Optical Properties. *Sol. Energy Mater. Sol. Cells* **94**, 612-616 (2010).

[5] Chen, B.*, et al.*, Room Temperature Insulator-to-Metal Transition of VO_2/TiO_2 Epitaxial Bilayer Films Grown on M-plane Sapphire Substrates. *Adv. Electron. Mater.* **8**, 2100687 (2022).

[6] Mishra, K.C., K.H. Johnson, and P.C. Schmidt, Electronic Structure of Antimony-doped Tin Oxide. *Phys. Rev. B* **51**, 13972-13976 (1995).

[7] Vining, C.B., A Model for the High-Temperature Transport-Properties of Heavily Doped N-Type Silicon-Germanium Alloys. *J. Appl. Phys.* **69**, 331-341 (1991).

[8] Button, K.J., C.G. Fonstad, and W. Dreybrodt, Determination of the Electron Masses in Stannic Oxide by Submillimeter Cyclotron Resonance. *Phys. Rev. B* **4**, 4539-4542 (1971).

[9] Zhou, W.*, et al.*, Band Gap Engineering of SnO_2 by Epitaxial Strain: Experimental and Theoretical Investigations. *J. Phys. Chem. C.* **118**, 6448-6453 (2014).

[10] Zhu, Z.*, et al.*, Structure and Photoluminescence Properties of Rpitaxial SnO_2 Films Grown on α-Al_2O_3 (012) by MOCVD. *J. Lumin.* **131**, 88-91 (2011).

[11] Lockwood, D.J., Z.H. Lu, and J.M. Baribeau, Quantum Confined Luminescence

in Si/SiO_2 Superlattices. *Phys. Rev. Lett.* **76**, 539-541 (1996).

[12] Liang, D.D.*, et al.*, Thickness Optimization toward High-Performance Bottom-Gated Transparent Tin Dioxide Thin-Film Transistors. *ACS Appl. Electron. Mater.* **2**, 3454-3458 (2020).

[13] Shanthi, E.*, et al.*, Electrical and Optical Properties of Undoped and Antimony - Doped Tin Oxide Films. *J. Appl. Phys.* **51**, 6243-6251 (1980).

Chapter 6. Summary

The given doctoral thesis focused on the modulation of the optoelectronic properties of a series of functional oxide films with rutile structure. The approach was using the epitaxial strain from the substrate to introduce the orthorhombic distortion. Compared with other conventional methods such as chemical doping and filed gating, this method is more stable and has less parasitic effects.

In chapter 2, I report the strain effects on the IMT behaviors of VO_2/TiO_2 epitaxial bilayer films grown on M-sapphire substrate. A systematic study with varied thicknesses of TiO_2 and VO_2 layer is conducted. By changing the VO_2 thickness from 40 to 5.5 nm while fixing the TiO_2 thickness to 200 nm, the T_c gradually decreased from 320 K to 305 K, which is highly reduced compared to that of bulk VO_2, suggesting that TiO_2-buffered M-sapphire substrate plays a similar effect to the TiO_2 substrate. Note that orthorhombic distortion is introduced to the film due to the anisotropic lattice parameter of M-sapphire substrate in the in-plane directions. Such distortion is enlarged when reducing TiO_2 thickness, resulting in the suppression of IMT behavior.

In chapter 3, I propose a solution for the strain relaxation and crack formation of VO_2 film grown on TiO_2 substrate. A TiO_2 strain compensation layer (SCL) was inserted between two VO_2 layers to maintain the strain condition of VO_2. The recovery of abrupt

IMT behavior and absence of cracks suggest that high strain condition of VO_2 is maintained when TiO_2 thickness exceeds 9 nm. By further alternately stacking VO_2 and TiO_2 layers, I demonstrate that the use of TiO_2 SCL is useful to maintain clear clockwise IMT behavior even when the overall VO_2 thickness is ~50 nm, far thicker than the theoretical thickness (t_c ~15 nm) of VO_2 relaxation.

In chapter 4, I report the effects of orthorhombic distortion on the properties of rutile TiO_2 films. I fabricated 0.5% Nb:TiO_2 films on M-sapphire substrate. By varying the thickness ranging from 300 to 5 nm, the degree of orthorhombic distortion (lattice parameter, b/a) was regulated from ~1.01 to ~1.035. Correspondingly, the carrier effective mass (m^*) decreases from 35 m_0 to 3 m_0 (m_0: electron mass) but the optical bandgap increases, suggesting the optoelectronic properties of rutile TiO_2 is modulated by introducing the lattice distortion.

In chapter 5, I report a comparison study between Nb:TiO_2 film and SnO_2 film grown on M-sapphire substrates. Nb:TiO_2 film is distorted as shown in chapter 4, indicating the strained condition, whereas the lattice parameters of Ta:SnO_2 films are consistent with the bulk value, suggesting complete strain relaxation. STEM observation revealed that the complete strain release of SnO_2 is due to the combination of large mismatch-induced high strain relaxation and the negligible mismatch-induced strain absence. By contrast, the moderate mismatch between TiO_2 and substrate results in the strained condition.

Correspondingly, the properties of Nb:TiO_2 are significantly regulated due to distortion whereas the property change of SnO_2 does not include the contribution of distortion.

In short, I systematically studied the epitaxial strain effects on optoelectronic properties of rutile-structured VO_2, TiO_2, and SnO_2 epitaxial films. The related results would provide useful guidance for the property design of rutile-type oxides and the development of related devices.

Acknowledgements

This thesis was conducted under the supervision of Prof. Hiromichi Ohta at Research Institute for Electronic Science, Hokkaido University from October 2019 to March 2023, including a half year of research student period.

First of all, I would like to express my sincere gratitude to my supervisor, Prof. Hiromichi Ohta (RIES, Hokkaido U.), for his invaluable guidance and continuous support during my PhD study. This is my first time studying and living abroad for such a long time. Climate, cultural difference, language… many things troubled me when I first arrived at Sapporo. It was Prof. Ohta who offered me meticulous care in my daily life, helping me through the initial difficulties. For study and research, Prof. Ohta always helped me address and solve the problems accurately. His keen sense, rigorous attitudes and unlimited enthusiasm on research benefited me a lot in past several years. These noble qualities would be my relentless pursuit and the most precious wealth in my future career.

I would like to offer my special thanks to Prof. Tsukasa Katayama (RIES, Hokkaido U.). He brought me into a new field of multiferroics and taught me a lot. Some of my research achievements were achieved under his tireless help. Prof. Katayama is no doubt a good teacher and beneficial friend for me.

I also would like to extend my great thanks to Prof. Hai Jun Cho (RIES, Hokkaido U. until 2022.8, currently at U. Ottawa) and Prof. Yusaku Magari (RIES, Hokkaido U.) for guidance in scientific research and help in daily life. They guided my research with their wealth vast knowledge and research experience.

Next, I would like to thank all lab members I have worked together with in Ohta lab. Dr. Yuqiao Zhang (OB, Professor at Jiangsu U.), Dr. Xi Zhang (OG, Professor at CQUT), Dr. Prashant Ghediya (Postdoc, RIES, Hokkaido U.), Dr. Takaki Onozato (OB, SONY), Dr. Gowoon Kim (OG, SAMSUNG ELECTRO-MECHANICS), Dr. Doudou Liang (OG, Professor at Ludong U.), Dr. Mian Wei (OG, Professor at Henan U.), Dr. Qian Yang (OG, Professor at Jiangsu U.), Mr. Yuzhang Wu (Ph.D candidate, IST, Hokkaido U.), Ms. Hui Yang (Ph.D candidate, BJTU), Mr. Lizhikun Gong (Ph.D candidate, IST, Hokkaido U.), Mr. Zhiping Bian (Ph.D candidate, IST, Hokkaido U.), Mr. Kungwan Kang (Ph.D candidate, IST, Hokkaido U.), Mr. Kenyu Sugo (OB), Mr. Yugo Takashima (OB), Mr. Takashi Fujimoto (OB), Mr. Liao Wu (OB), Mr. Rui Yu (Master candidate, IST, Hokkaido U.), Mr. Yaoming Liu (Master candidate, IST, Hokkaido U.), Ms. Mitsuki Yoshimura (Undergraduate, Hokkaido U.), Ms. Ozaki (Secretary, Ohta lab) *et al.* for all the countless help during my study and life. Special thinks to Dr. Yuqiao Zhang for teaching me the manipulation of facilities in Ohta lab as well as lots of helpful scientific discussions.

I really appreciate the collaborations from Prof. Ikuhara (U. Tokyo), Prof. Feng (U. Tokyo), and Dr. Lin (U. Tokyo) for STEM observations, Prof. Matsunaga (Nagoya U.) and Mr. Hoshino (Nagoya U.) for DFT calculations, Prof. Jeen (Pusan Nat'l U.) and Mr. Kang (Pusan Nat'l U. until 2022.2, currently Ph.D candidate, IST, Hokkaido U.) for XAS measurements and analysis. Without their helps and discussions, I cannot finish this thesis. I also appreciate the thesis committee members, Prof. Junichi Motohisa (IST, Hokkaido U.), Prof. Seiya Kasai (RCIQE, Hokkaido U.) and Prof. Toshihiro Shimada (Faculty of ENG., Hokkaido U.) for taking time to review this thesis and giving me valuable comments.

Thirdly, I do deepest appreciate to my parents, my wife, my son. Thanks to their unconditional support and tolerance for my inability to take care of our family. I should say sorry to my wife and my son for the absence of accompany. I will never leave again.

Lastly, I'm grateful to the financial support provided by the Ministry of Education, Culture, Sports, Science and Technology (MEXT), Japan as well as the support from Chinese consulate general in Sapporo.

Binjie Chen

Sapporo, Japan

List of Publications

Publications related to this thesis

[1] **B. Chen***, G. Kim, H.J. Cho, H. Ohta*, "Room Temperature Insulator-to-Metal Transition of VO_2/TiO_2 Epitaxial Bilayer Films Grown on M-plane Sapphire Substrates", *Adv. Electron. Mater*. **8**, 2100687 (2021).

[2] **B. Chen***, K. Kang, H. Jeen, Y. Zhang, J. Lin, B. Feng, Y. Ikuhara, S. Hoshino, K. Matsunaga, H. Ohta*, "Orthorhombic Distortion-induced Anatase-like Optoelectronic Properties of Rutile TiO_2", *J. Appl. Phys.* **132**, 185301 (2022).

[3] **B. Chen***, J. Lin, B. Feng, Y. Ikuhara, H. Ohta*, "Room Temperature Insulator-to-Metal Transition of Strained VO_2/TiO_2 Multilayered Films", Submitted.

Other publications

[4] **B. Chen**, and T. Katayama*, "Hexagonal RFeO$_3$ (R = Dy, Er, and Lu) Films Grown on Glass Substrates with Both Magnetic and Ferroelectric Orders", *ACS Appl. Electron. Mater.* **5**, 344−349 (2022).

[5] **B. Chen**, H. Ohta, and T. Katayama*, "Ferroelectric and Magnetic Properties of Hexagonal $ErFeO_3$ Epitaxial Films", *ACS Appl. Electron. Mater.* **4**, 4547−4552 (2022).

[6] Y. Zhang[#], **B. Chen**[#], X. Deng, Z. Guan, B. Chen, Y. Chen, N. Zhong*, P. Xiang*, C. Duan, "A Mott Transistor with Giant Switching Ratio at Room Temperature and its Emulation of Artificial Synapses", *J. Mater. Chem. C* **10**, 11654−11663 (2022).

[7] **B. Chen**, T. Hasegawa, H. Ohta, T. Katayama*, "Antiferroelectric-to-Ferroelectric Phase Transition in Hexagonal Rare-earth Iron Oxides", *J. Mater. Chem. C* **10**, 5621−5626 (2022).

[8] D. Liang*, **B. Chen**, B. Feng, Y. Ikuhara, H.J. Cho, H. Ohta*, "Optimization of Two-Dimensional Channel Thickness in Nanometer-Thick SnO_2-Based Top-Gated Thin-Film Transistors using Electric Field Thermopower Modulation: Implications for Flat-Panel Displays", *ACS Appl. Nano Mater.* **3**, 12427−12432 (2020).

[9] D. Liang*, **B. Chen**, H.J. Cho, H. Ohta*, "Thickness Optimization toward High-Performance Bottom-Gated Transparent Tin Dioxide Thin-Film Transistor", *ACS Appl. Electron. Mater.* **2**, 3454−3458 (2020).

List of Presentations

[1] **Binjie Chen**, Gowoon Kim, Hai Jun Cho, and Hiromichi Ohta, "Orthorhombic Distortion Induced Insulator-to-Metal Transition Behavior of VO_2/TiO_2 Bilayer Films on $(1\bar{1}00)$ α-Al_2O_3", 7th International Conference on Advances in Functional Materials (AFM 2023), Fukuoka, Japan, January 9−12, 2022. (Oral)

[2] **Binjie Chen**, Hiromichi Ohta, "Room Temperature Insulator-to-Metal Transition of Strained VO_2/TiO_2 Multilayered Films", The 23rd RIES-Hokudai International Symposium 拓 [Taku], Sapporo, Japan, December 5−6, 2022. (Poster)

[3] **Binjie Chen**, Jinchuan Lin, Bin Feng, Yuichi Kithara, and Hiromichi Ohta, "Room Temperature Insulator-to-Metal Transition of Strained VO_2/TiO_2 Multilayered Films", 薄膜材料デバイス研究会 第 19 回研究集会 in 京都, 龍谷大学響都ホール（京都府京都市）, 2022 年 11 月 17 日−18 日. (Oral)

[4] **Binjie Chen**, Jinchuan Lin, Bin Feng, Yuichi Kithara, and Hiromichi Ohta, "Room Temperature Insulator-to-Metal Transition of Strained VO_2/TiO_2 Multilayered Films", 令和 4 年度日本セラミックス協会東北北海道支部研究発表会, 伝国の杜（山形県米沢市）, 2022 年 11 月 10 日−11 日. (Oral)

[5] 陳 斌杰, 太田裕道, "VO_2/TiO_2 多層膜の段階的絶縁体/金属転移", 2022 年第 83 回 応用物理学会秋季学術講演会, 東北大学川内北キャンパス+オンライン, 2022 年 9 月 20 日−23 日. (Oral)

[6] **Binjie Chen**, Yuqiao Zhang, Katsuyuki Matsunaga, and Hiromichi Ohta,

"Optoelectronic Properties of Orthorhombic-Distorted Nb:TiO_2 Films", The 22nd International Vacuum Congress (IVC-22), Sapporo, Japan, September 11−16, 2022. (Oral)

[7] **陳 斌杰**, 張 雨橋, 太田裕道, "サファイア M 面基板上に成長させたルチル型 Nb:TiO_2 エピタキシャル薄膜の斜方晶歪みと光電子輸送特性", 2022 年 第 69 回 応用物理学会 春季学術講演会, 青山学院大学 相模原キャンパス＋オンライン, 2022 年 3 月 22 日−26 日. (Oral)

[8] **Binjie Chen**, Gowoon Kim, Hai Jun Cho, and Hiromichi Ohta, "Room Temperature Insulator-to-Metal Transition of VO_2/TiO_2 Epitaxial Bilayers on $(1\bar{1}00)$ α-Al_2O_3", 日本セラミックス協会 第 60 回セラミックス基礎科学討論会, 熊本大学, 2022 年 1 月 8 日−9 日. (Oral)

[9] **Binjie Chen**, Tetsuya Hasegawa, Hiromichi Ohta, Tsukasa Katayama, "Antiferroelectric to Ferroelectric Phase Transition in Hexagonal $DyFeO_3$ Films", The 22nd RIES-HOKUDAI International Symposium, December 5−7, 2021. (Poster)

[10] **B. Chen**, T. Hasegawa, H. Ohta, T. Katayama, "Temperature induced Anti- to Ferroelectric Transition in Hexagonal $DyFeO_3$ Films", 令和 3 年度日本セラミックス協会東北北海道支部研究発表会, online, 2021.11.18−19. (Oral)

[11] **Binjie Chen**, Tetsuya Hasegawa, Hiromichi Ohta, Tsukasa Katayama, "Temperature driven Anti- to Ferroelectric Phase Transition in Hexagonal $DyFeO_3$ Films", 薄膜材料デバイス研究会 第 18 回研究集会 in 京都, オンライン,

2021.11.11−12. (Poster)

[12] **B. Chen**, G. Kim, H.J. Cho, H. Ohta, "Lattice Strain and Insulator-to Metal Transition of VO_2/TiO_2 Epitaxial Bilayer Films Grown on M-plane Sapphire Substrates", 第 82 回 応用物理学会秋季学術講演会, online, 2021.9.10−13. (Oral)

[13] **Binjie Chen**, Gowoon Kim, Hai Jun Cho, Hiromichi Ohta, "Reduction of the T_c and suppression of the ΔT_c of VO_2 epitaxial films on TiO_2 buffered sapphire substrate (FF02)", 63rd Electronic Materials Conference (EMC 2021), Virtual, June 23−25, 2021. (Oral)

[14] **Binjie Chen**, Gowoon Kim, Hai Jun Cho, and Hiromichi Ohta, "Modulation of the Metal-to-Insulator Transition Behavior of VO_2 Films", 2021 年 第 68 回 応用物理学会春季学術講演会, online, 2021.3.16−19. (Oral)

[15] **Binjie Chen**, Gowoon Kim, Hai Jun Cho, and Hiromichi Ohta, "Modulation of the Metal-to-Insulator Transition Behavior of VO_2 Epitaxial Films by Insertion of TiO_2 Layers", 第 56 回 応用物理学会北海道支部/第 17 回日本光学会北海道支部合同学術講演会, online, 2021.1.9−10. (Oral)

[16] **Binjie Chen**, Gowoon Kim, Hai Jun Cho, and Hiromichi Ohta, "Reduction of Metal-to-Insulator Transition Temperature of VO_2 Films by Inserting TiO_2 Layers", The 21st RIES-Hokudai International Symposium 間 [ma], online, December 10−11, 2020. (Poster)

[17] **Binjie Chen**, Gowoon Kim, Hai Jun Cho, and Hiromichi Ohta, "Metal-to-

insulator transition temperature reduction of VO_2 films by inserting TiO_2 layers”, 令和 2 年度 日本セラミックス協会 東北北海道支部 研究発表会, online, November 13−14, 2020. (Oral)

List of Awards

[1] **発表奨励賞** (2021.03.25), **Binjie Chen**, Gowoon Kim, Hai Jun Cho, and Hiromichi Ohta, "Modulation of the Metal-to-Insulator Transition Behavior of VO_2 Epitaxial Films by Insertion of TiO_2 Layers", 第 56 回 応用物理学会北海道支部/第 17 回日本光学会北海道支部合同学術講演会, online, 2021.1.9−10.

[2] Poster Award (2022.12.06), **Binjie Chen**, Hiromichi Ohta, "Room Temperature Insulator-to-Metal Transition of Strained VO2/TiO2 Multilayered Films", The 23rd RIES-Hokudai International Symposium 拓 [Taku], Sapporo, Japan, 2022.12. 5−6.